Image Simulation and Assessment of the Colour and Spatial Capabilities of the Colour and Stereo Surface Imaging System (CaSSIS) on the ExoMars Trace Gas Orbiter

Livio Tornabene, Frank Seelos, Antoine Pommerol, Nicholas Thomas, C. Caudill, Patricio Becerra, C. Bridges, Shane Byrne, Marco Cardinale, Matthew Chojnacki, et al.

Image simulation and assessment of the colour and spatial capabilities of the Colour and Stereo Surface Imaging System (CaSSIS) on the ExoMars Trace Gas Orbiter

Livio L. Tornabene[1], Frank. P. Seelos[2], Antoine Pommerol[3], Nicholas Thomas[3], C.M. Caudill[1], Patricio Becerra[3], John C. Bridges[4], Shane Byrne[5], Marco Cardinale[6], Matthew Chojnacki[5], Susan J. Conway[7], Gabriele Cremonese[8], Colin M. Dundas[9], M. R. El-Maarry[10], Jennifer Fernando[5], Candice J. Hansen[11], Kayle Hansen[1], Tanya N. Harrison[12], Rachel Henson[4], Lucia Marinangeli[6], Alfred S. McEwen[5], Maurizio Pajola[13], Sarah S. Sutton[5] and James J. Wray[14]

[1]Centre for Planetary Science and Exploration/Department of Earth Sciences, University of Western Ontario, London, Ontario N6A 5B7, Canada (E-mail: ltornabe@uwo.ca)

[2]Johns Hopkins University Applied Physics Laboratory, Laurel, Maryland, USA

[3]Physikalisches Institut, Sidlerstr. 5, University of Bern, CH-3012 Bern, SWITZERLAND

[4]Space Research Centre, Leicester Institute for Space and Earth Observation, University of Leicester, UK LE1 7RH

[5]Lunar and Planetary Laboratory, University of Arizona, Tucson, Arizona 85721-0092, USA

[6]DiSPUTER, Università G.d'Annunzio, Chieti, Italy

[7]CNRS, Laboratoire de Planétologie et Géodynamique, CNRS/INSU UMR 6112, Université de Nantes, 2 chemin de la Houssinière, BP 92205, 44322 Nantes Cedex 3, France.

[8]INAF-Osservatorio Astronomicodi Padova, Vicolo Osservatorio 5, 35122 Padova, Italy

[9]U.S. Geological Survey, Astrogeology Science Center, 2255 N. Gemini Dr., Flagstaff, AZ 86001, USA.

[10]Laboratory of Atmospheric and Space physics (LASP), University of Colorado, 3665 Discovery Dr., Boulder, CO 80303, USA.

[11]Planetary Science Institute, 1700 E. Fort Lowell, Suite 106, Tucson, AZ 85719, USA

[12]NewSpace Initiative, Arizona State University, P.O. Box 876004, Tempe, AZ 85287

[13]NASA Ames Research Center, Moffett Field, CA 94035, USA.

[14]School of Earth and Atmospheric Sciences, Georgia Institute of Technology, Atlanta, GA 30332, USA.

Keywords: Mars; Mars, geology; Mars, surface processes; Mars, climate; Mars, change detection; Mars, landing sites; multispectral imaging; image processing; band ratios; pan-sharpening

ABSTRACT

This study aims to assess the spatial and visible/near-infrared (VNIR) colour/spectral capabilities of the 4-band Colour and Stereo Surface Imaging System (CaSSIS) aboard the ExoMars 2016 Trace Grace Orbiter (TGO). The instrument response functions for the CaSSIS imager was used to resample spectral libraries, modelled spectra and to construct spectrally (*i.e.*, in I/F space) and spatially consistent simulated CaSSIS image cubes of various key sites of interest and for ongoing scientific investigations on Mars. Coordinated datasets from Mars Reconnaissance Orbiter (MRO) are ideal, and specifically used for simulating CaSSIS. The Compact Reconnaissance Imaging Spectrometer for Mars (CRISM) provides colour information, while the Context Imager (CTX), and in a few cases the High-Resolution Imaging Science Experiment (HiRISE), provides the complementary spatial information at the resampled CaSSIS unbinned/unsummed pixel resolution (4.6 m/pixel from a 400-km altitude). The methodology used herein employs a Gram-Schmidt spectral sharpening algorithm to combine the ~18-36 m/pixel CRISM-derived CaSSIS colours with I/F images primarily derived from oversampled CTX images. One hundred and eighty-one simulated CaSSIS 4-colour image cubes (at 18-36 m/pixel) were generated (including one of Phobos) based on CRISM data. From these, thirty-three "fully"-simulated image cubes of thirty unique locations on Mars (*i.e.*, with 4 colour bands at 4.6 m/pixel) were made. All simulated image cubes were used to test both the colour capabilities of CaSSIS by producing standard colour RGB images, colour band ratio composites (CBRCs) and spectral parameters. Simulated CaSSIS CBRCs demonstrated that CaSSIS will be able to readily isolate signatures related to ferrous (Fe^{2+}) iron- and ferric (Fe^{3+}) iron-bearing deposits on the surface of Mars, ices and atmospheric phenomena. Despite the lower spatial resolution of CaSSIS when compared to HiRISE, the results of this work demonstrate that CaSSIS will not only compliment HiRISE-scale studies of various geological and seasonal phenomena, it will also enhance them by providing additional colour and geologic context through its wider and longer full-colour coverage (~9.4 x 50 km), and its increased sensitivity to iron-bearing materials from its two IR bands (RED and NIR). In a few examples, subtle surface changes that were not easily detected by HiRISE were identified in the simulated CaSSIS images. This study also demonstrates the utility of the Gram-Schmidt spectral pan-sharpening technique to extend VNIR colour/spectral capabilities from a lower spatial resolution colour/spectral dataset to a single-band or panchromatic image grayscale image with higher resolution. These higher resolution colour products (simulated CaSSIS or otherwise) are useful as means to extend both geologic context and mapping of datasets with coarser spatial resolutions. The results of this study indicate that the TGO mission objectives, as well as the instrument-specific mission objectives, will be achievable with CaSSIS.

1 Introduction

The payload of the ExoMars 2016 Trace Grace Orbiter (TGO) (Vago et al 2015) is designed to detect and characterise the concentration and spatial distribution of trace gases in the Martian atmosphere over various times of day, incidence and spanning all the Martian seasons. Methane (CH_4), a metastable and short-lived trace gas linked to life and/or active geological processes, was putatively detected on Mars from Earth-based, orbital and surface measurements (*e.g.*, Formisano et al 2004; Mumma et al 2009; Fonti and Marzo 2010; Villanueva et al 2013; Webster et al 2015) and was the catalyst for this mission (Zurek et al 2011). The Colour and Stereo Surface Imaging System (CaSSIS) is a moderately high-resolution 4-colour visible/near-infrared (VNIR) stereo camera included as part of the payload of the TGO (Thomas et al this issue). As a VNIR imager pointed at the surface of Mars, CaSSIS is specifically tasked with: **1)** *characterising possible [surface/subsurface] sources for methane and other trace gases*; **2)** *investigating dynamic surface processes that may contribute to atmospheric gases*; and **3)** *certifying and characterising safety and hazards (e.g., rocks, slopes, etc.) associated with candidate landing sites for ExoMars 2020 and other future surface missions*. Furthermore, and similarly to the High-Resolution Imaging Science Experiment (HiRISE) (McEwen et al 2007, 2010) on the Mars Reconnaissance Orbiter (MRO) [Zurek and Smrekar 2007], investigations by the members of the CaSSIS team emphasize a variety of Mars science objectives organized under specific science theme groups (*e.g.*, seasonal processes, impact cratering, etc.). This ensures that CaSSIS will cover diverse areas of study that include and go beyond the focused science objectives of CaSSIS and TGO. The instrument design and anticipated CaSSIS observations are expected to provide high-resolution and full-colour stereo products that will highly complement past, present, and future datasets.

This study seeks to assess and simulate the colour and spatial capabilities of CaSSIS and thereby assess how CaSSIS, and its various expected high-level derived data products, will be used to meet both orbiter and instrument objectives, and evaluate to what extent CaSSIS falls short of, complements, or in some cases even exceeds the capabilities of previous imagers (*e.g.*, HiRISE).

Despite the significantly higher spatial resolution of HiRISE, CaSSIS offers three notable advantages over HiRISE including: 4-band colour, a wider image swath, and colour capability across the entire image. CaSSIS can also acquire along-track stereo images on a single orbital pass, and, due to the orbital inclination of the TGO, it can obtain images over a range in local times and incidence; however, we note here that these particular characteristics are not a major focus of this simulation study (for more details, see Thomas et al this issue).

In this study, we begin by making use of the CaSSIS instrument spectral response functions (*i.e.*, bandpasses) to evaluate CaSSIS colour sensitivity to various minerals and Fe-bearing surface materials known to exist on Mars. In addition to this, we have developed methods for simulating CaSSIS observations and data products using complementary and coordinated MRO datasets covering various sites of interest on Mars. These simulated CaSSIS products cover spectral mineral/phase type-localities, key morphologic features related to dynamic surface processes, and high-priority landing sites. These simulated CaSSIS 4-band colour image cubes are then used to assess to what extent CaSSIS will continue and expand upon ongoing investigations of various surface processes monitored by HiRISE and previous imagers, such as the Mars Orbiter Camera (MOC), the High-Resolution Stereo Camera (HRSC), and the Context Imager (CTX). The results of our study herein are anticipated to also help the CaSSIS science and operations teams to determine the best higher-level data products to produce, and best practices for planning targeted colour and stereo observations, and aid colour calibration efforts. As such, this work will enable the team to optimize both operations and maximise the science return for the mission. Lastly, the methods used here to create fully-simulated CaSSIS image cubes provides the means to extend the monitoring of long-term surface changes on Mars with CaSSIS to the pre-TGO era (*i.e.*, back to the onset of the MRO mission in late 2006) by providing a spectrally and spatially consistent MRO-derived CaSSIS-compatible product that may be used to for comparison to actual CaSSIS data to be acquired in 2018 and beyond.

1.1 CaSSIS instrument and colour band selection

CaSSIS is a pushframe imager that will provide colour images of the Martian surface at ~4.6 m/pixel, which will be up to ~9.4 km wide and possibly up to ~40-

50 kilometres long from a final circularized orbital altitude of ~400km. CaSSIS has a fixed pointing of ~10° off nadir and a rotation mechanism that is used to acquire stereo images in a single orbital pass providing a 22.14° parallax angle. Unlike all other recent Mars orbiters with high-resolution cameras, the final configuration of the TGO orbit will be at an inclination of 74° to the equator; although this will limit the ability of CaSSIS to image targets above 74° N or S, it provides CaSSIS the means to image at multiple times of day across all seasons and over a larger range of incidence angles.

The pushframe imaging configuration utilized by CaSSIS offers some advantages with respect towards achieving a good radiometric calibration solution for colour CaSSIS images of Mars; this is further supported by recent results from the ground calibration effort thus far, which is showing very small errors against standard stars (see Roloff et al this issue). For more detailed information on design and ground calibration of the CaSSIS imaging system, please see Thomas et al and Roloff et al, respectively, this issue.

The 4 colour filters of CaSSIS correspond to blue-green (BLU), broadband orange-red (PAN), and two near-infrared colours (RED and NIR), collectively utilizing a detector sensitivity that spans ~400 to 1100 nm (Table 1). This wavelength sensitivity range is notably similar to HiRISE (Delamere et al 2010; McEwen et al 2010). The first two CaSSIS bands, blue-green (BLU) and a broadband red (PAN), are very similar to BG and RED filters of HiRISE, respectively (*c.f.,* Delamere et al 2010). With respect to the NIR, CaSSIS provides two bands (RED and NIR) that effectively split the single HiRISE IR band. These two CaSSIS NIR filters are expected to provide extra sensitivity to the detection of Fe-bearing surface materials.

Thee four CaSSIS bands will provide a Signal-to-Noise Ratio (SNR) that is ~50 % higher than the 3 bands of HiRISE, or ~7% higher SNR (>100:1 top of atmosphere) based on Mars reference surfaces under similar observational conditions (Thomas et al this issue; Roloff et al this issue). Based on these characteristics, CaSSIS will not only complement HiRISE colour products, but will also provide similar sensitivities to characteristic spectral features in this range that are useful for distinguishing Fe-bearing materials on Mars, as well as ices and

various atmospheric phenomena (*e.g.*, haze, fog, clouds, dust devils, avalanche clouds, etc.).

The reflectivity or I/F intensity of CO_2 and H_2O ice- and frost-bearing surfaces are higher in blue wavelengths compared to other Mars surface materials (*e.g.*, James et al 1994; Bell et al 1997). The reflectivity of H_2O is relatively lower than CO_2 ice in red and NIR wavelengths, due to a spectral slope towards the NIR and the presence of a relatively narrow and shallow absorption feature centred around 1030 nm (Figure 1) (*e.g.*, Williams and Ferrigno 1988; Becerra et al 2015). Furthermore, surfaces containing fine-grained ice or frost, especially if the ice/frost is transparent to translucent, will likely have high reflectance values over the entire 400-1100 nm sensitivity range of CaSSIS (*e.g.*, Appéré et al 2011), when compared to ice-free surfaces. Like ice/frost, various atmospheric phenomena (*e.g.*, fog, haze, clouds, active dust devils, avalanche clouds, etc.) also have relatively higher reflectance values over the visible spectrum, and especially over the bluer wavelengths and when compared to the Martian surface that lacks ice or frost (*e.g.*, James et al 1994; Bell et al 1997).

[FIGURE 1]

The VNIR colour of metal-bearing minerals is a consequence of metallic cations in the periodic table's first row of transition elements (*i.e.*, Ti to Cu). However, the colours observed in the most common rock forming minerals are often attributed to variations in the oxidation state of iron (Fe^{2+}, Fe^{3+}) and the crystalline structure (or lack thereof) of the material (Figure 1). Specifically, within the wavelength sensitivity range of CaSSIS, there are electronic transitions and crystal field effects due to the presence of ferrous (Fe^{2+}) iron-bearing minerals responsible for strong and diagnostic absorptions at ~700 – 1100 nm (*e.g.*, mafic minerals such as olivine and pyroxene). The CaSSIS sensitivity range also includes diagnostic broad absorptions extending from the UV to the visible, short of 550 nm, which arise from intervalence charge-transfer transitions of ferric iron Fe^{3+} and O^{2-} present in altered ferric (Fe^{3+}) iron-bearing minerals (*e.g.*, hematite, nontronite, etc.) (*e.g.*, Adams 1974; Hunt 1977; Hunt and Ashley 1979; Burns 1993). Although colour can be characteristic of specific minerals, it is not necessarily diagnostic. However, colour CaSSIS images (especially band ratios) are

expected to be quite helpful towards discriminating ferrous vs. ferric materials, ice- or frost-bearing surfaces, and extending spectral mapping from orbital instruments with coarser spatial scales, such as the Compact Reconnaissance Imaging Spectrometer for Mars (CRISM) and the Observatoire pour la Mineralogie, l'Eau, la Glace et l'Activite (OMEGA).

This knowledge of the general spectral behaviour over the CaSSIS wavelength sensitivity range that are due to the presence of various surface materials/atmospheric phenomena (summarized above) is utilized, in conjunction with the CaSSIS band positions, to formulate spectral ratios and parameters that will be used to isolate pixels with high-concentrations or good exposures of these materials on Mars (see Section 3).

2 Methods

2.1 CaSSIS colour-sensitivity to known minerals on Mars

Here we use the CaSSIS instrument response functions to resample, and then subsequently analyse, lab-measured spectra for selected minerals that are known to exist on Mars. A model for the instrument response and spectral sensitivity of CaSSIS (see Figure 2), from approximately 400 to 1100 nm, was built from manufacturer-provided spectral curves for each of the relevant instrument elements, the quantum efficiency of the detector, the transmission of the bandpass filters and the reflectance of the four-mirror telescope optics (Thomas et al this issue). All response curves were measured with a spectral sampling of 1 nm. These response curves were then verified in the laboratory during the pre-flight calibration of the instrument. See Roloff et al (this issue) for a discussion of the observed agreements and discrepancies during pre-flight calibration.

The minerals and phases selected for this study are based on published summaries of spectral studies of the Martian surface, *in situ* detections and the known composition of Martian meteorites (see Ehlmann et al 2011; Carter et al 2013; Ehlmann and Edwards 2014; and Viviano-Beck et al 2014 and references therein). The equivalent lab-measured spectra for Martian minerals and phases are derived from the USGS and CRISM mineral spectral libraries (*e.g.*, Clark et al

1993; PDS Geosciences Spectral Library: http://speclib.rsl.wustl.edu/, accessed 2017).

[FIGURE 2]

2.2 Creating simulated CaSSIS products

The second part of this study entails the creation and assessment of simulated CaSSIS image cubes covering various surface materials, landforms and other sites of interest on Mars based on MRO datasets. For this purpose, we created two types of simulated cubes: "partial" – ones that simulate the CaSSIS spectral/colour bands only, and "fully" – ones that simulate CaSSIS both spectrally (4 bands) and spatially (w.r.t. pixel-scale). We note here that our simulated CaSSIS cubes do not account for differences in modular transfer functions, geometric distortion, system noise, SNR, and atmospheric effects that will inherently vary with respect to the MRO data sources used to create a specific simulated CaSSIS cube and the actual CaSSIS images that will be acquired in the future. Nonetheless, these simulated products will enable us to begin to assess the general spectra/colour and spatial capabilities of CaSSIS.

Simulated CaSSIS spectral/colour image cubes are initially created by convolving VNIR spectral information obtained by the CRISM instrument (Murchie et al 2007) with the CaSSIS instrument response functions. However, these initial colour products maintain the spatial scale of the input CRISM cubes (*i.e.*, ~18-36 m/pixel) and constitutes our "partial" simulated product. These colour-only simulated products come as two types of image cubes, a "CRISM-CaSSIS Compatible" (C^3), and a "Corrected CRISM-CaSSIS Compatible" (C^4) cube, and are described in more detail below. A fully-simulated CaSSIS cube is produced by merging one of the two previously mentioned simulated colour cubes (C^4, but C^3 if C^4 not available) with a 32-bit radiometrically calibrated I/F panchromatic image from CTX (Malin et al 2007) that is oversampled from ~5-6m/pixel to the pixel-resolution of CaSSIS (*i.e.*, ~4.6m/pixel). In only a few cases, resampled 32-bit radiometrically calibrated I/F HiRISE RED mosaic images (McEwen et al 2007, 2010; Delamere et al 2010) were used instead of CTX.

Triple or double coordinated MRO observations (*i.e.*, simultaneous acquisition of CRISM-CTX, CRISM-HiRISE, or CRISM-CTX-HiRISE) are sought to

mitigate issues inherent in observations taken at different times with disparate observation geometries and acquisition circumstances. MRO coordinated observations are ideal for CaSSIS simulated data product generation as they share a common atmospheric state (weather conditions), sun-surface-spacecraft geometry (incidence, emission and phase angles), season (L_s), and no surface changes in areas of Mars known to have seasonal changes. In cases where coordinated observations were unavailable, observations taken at different times were used, but only where surface changes, weather, and geometric discrepancies were deemed to be minimal These simulations were kept to a minimum (only 4 cases, see Table 2), as coordinated observations are strongly preferred for the best simulated results.

Also in a few cases, and were CTX and HiRISE stereo-derived DTMs were available, we resampled these DTMs to ~18.4 m post (*i.e.*, 3x the anticipated pixel-scale). For one simulated test case, specifically geared toward assessing spatial changes in the Nili Patera active dune field, a time-series pair of CTX images were controlled to a HiRISE stereo pair and a pre-existing Digital Terrain Model (DTM). For this task, SOCET SET® BAE system photogrammetry software and the techniques summarized by Kirk et al (2008) were employed. Orthorectified CTX images were oversampled to the CaSSIS pixel-scale (4.6m/pixel), and then change detection methods, including animated GIFs and difference maps were applied to see if spatial changes could be detected (see Section 3.5.2 for more details).

Radiometrically calibrated Planetary Data System (PDS) datasets for CRISM, CTX and HiRISE were used in this study with all general processing tasks described herein performed with a software package from Harris Geospatial Solutions that includes both Environment for Visualizing Images (ENVI) and the Interactive Data Language (IDL). Integrated Software for Imagers and Spectrometers (ISIS) pre-processing of 32-bit CTX I/F data was accomplished and obtained through the USGS PILOT web interface. Gain/offsets to convert calibrated 8-bit HiRISE images to 32-bit I/F data was accomplished in ENVI via the HiRISE Toolkit available through the PDS.

289 *2.2.1 Creating the CaSSIS colours from CRISM*

290 The spectral/colour component of a given CaSSIS simulation is derived from
291 a CRISM hyperspectral targeted observation VNIR image cube (VNIR S-detector:
292 364-1055 nm; 6.55 nm sampling; ~20 m/pixel full spatial resolution) (Murchie et al
293 2007). The spectral sampling characteristics of the CRISM instrument allow for the
294 synthesis of CRISM-derived data products that are spectrally compatible with
295 other Martian remote sensing instruments (Seelos et al 2011a), such as CaSSIS
296 (Thomas et al this issue) and HiRISE (McEwen et al 2007).

297 The "CRISM-compatible" data product concept originated as part of an
298 ongoing CRISM/HIRISE inter-instrument calibration effort, which has also been
299 employed in CRISM/HiRISE radiometric data fusion efforts (*e.g.*, Seelos et al
300 2011b]). An overview of the CRISM-HIRISE compatible transform is included as part
301 of our supporting online supplemental materials included with this manuscript
302 (also refer to Figures S1-S3), with the specifically illustrated in Figure S4, and
303 provided as a detailed walkthrough using ENVI/IDL therein.

304 The transformation process is fundamentally similar to the CRISM-HiRISE
305 one, with the four CaSSIS instrument response functions (BLU, PAN, RED, NIR)
306 taking the place of the three HiRISE response functions (BG, RED, IR) (*c.f.*, Figure 2
307 with Figure S1). The "CRISM-CaSSIS Compatible" (C^3) spectral processing portion
308 of the transformation of a CRISM VNIR image cube consists of the following steps,
309 and is illustrated in Figures 3a and 3b : **1)** Transforming the CRISM reflectance (I/F)
310 image cube to the equivalent spectral radiance; **2)** Interpolating the radiance
311 spectra across the CRISM VNIR filter boundary (~638 nm - ~690 nm) to cover the
312 CaSSIS PAN bandpass filter, extrapolating the spectra short-ward of ~410 nm, and
313 long-ward of ~1017 nm as required to cover the full wavelength ranges of CRISM
314 and CaSSIS (for the CaSSIS BLU and NIR bandpass filters, respectively); **3)**
315 Oversampling the interpolated/extrapolated radiance spectra to match the
316 spectral sampling of the compatible instrument response functions (1 nm sampling
317 of the CaSSIS response curves); **4)** Integrating the interpolated/extrapolated and
318 oversampled radiance spectra with respect to the instrument response functions;
319 and 5) Transforming the result back to I/F.

320 **[FIGURE 3]**

The resulting data product inherits the spatial and geometric characteristics and radiometric calibration from the input CRISM image cube, but has the spectral characteristics of the CaSSIS instrument. We note that the C^3 data products consist of transforming the as-acquired top-of-atmosphere (TOA) CRISM spectral reflectance (Figure 3a) to the compatible CRISM-CaSSIS 4-band reflectance without any additional data processing or corrections. As a result, the C^3 image cubes retain spectral-photometric variations inherent to the CRISM hyperspectral targeted observation data acquisition scenario, specifically the continuously varying observation geometry due to the requisite gimbal motion required for targeted CRISM imaging mode. The varying viewing geometry of CRISM targeted observations typically manifests as a wavelength-dependent along-track gradient with brightening toward the inbound and/or outbound edge of the observation central scan (*c.f.*, Figure 3a and 3b with 3c and 3d). These signal gradients are due primarily to the change in atmospheric path length, and the strong phase angle and wavelength dependence (over the CRISM VNIR and CaSSIS wavelength range) of atmospheric aerosol scattering (Wolff et al 2009), but also include some contributions from surface material scattering from these observation geometries as well (*e.g.*, Fernando et al 2016).

Although CaSSIS will acquire along-track stereo observations at different phase angles, the CRISM continuous gimbal motion is not consistent with CaSSIS push-frame (or HiRISE pushbroom) data acquisition. Therefore, to address this difference in how CRISM and CaSSIS image Mars, an additional data processing procedure is employed that results in data products which are consistent with the CaSSIS data acquisition scenario. We refer to this final spectral/colour data product as a "Corrected CRISM-CaSSIS Compatible" (C^4) image cube. These products incorporate an empirical CRISM geometric correction that transforms the original CRISM image cube (Figure 3a) to a synthetic state as though the data were acquired in a push-broom geometry (Figure 3c). Then the corrected CRISM image cube is transformed into the C^4 data product (Figure 3d) by the CRISM-CaSSIS compatible spectral processing as described above. The Empirical Geometric Normalization (EGN) procedure (Seelos et al 2011a) is a key component of the CRISM Targeted Empirical Record (TER) / Map-projected Targeted Reduced Data

353 Record (MTRDR) data processing pipeline (Seelos et al 2012; 2016), which
354 characterises the geometric dependencies across all segments of a CRISM targeted
355 observation, including the central scan and all available accompanying emission
356 phase function (EPF) segments, and then scales the dependencies out of the
357 central scan data relative to a reference observation geometry. We note that the
358 C^4 data products do retain both the photometric geometry (incidence, emission,
359 phase angle) of the source CRISM observation at its corresponding reference
360 geometry, and the combined effects of the surface/atmosphere system. As a
361 result, the C^4 products have spectral/colour variability consistent with as-acquired
362 TOA CaSSIS image cube. Importantly, the CRISM EGN procedure is dependent on
363 the availability of EPF segments that sample more extreme emission angles than
364 the central scan. Unfortunately, at the beginning of October of 2012, the CRISM
365 gimbal range was restricted due to hardware ageing issues, and the acquisition of
366 EPFs were no longer possible. CaSSIS simulations that make use of CRISM targeted
367 observations acquired since the onset of gimbal range restrictions employ the C^3
368 products, and as such retain a non-pushbroom CRISM-source spectral-
369 photometric variability. However, the restricted gimbal range also limits the
370 emission and phase angle range sampled by latter-mission CRISM targeted
371 observations, which in turn can limit the geometric-dependent variability.
372 Therefore the C^3-derived products can be employed on a case-by-case basis in the
373 evaluation of simulated CaSSIS intra-scene colour variability, particularly when
374 band ratios and other continuum-normalized evaluation criteria are considered,
375 and where it is not possible to generate C^4 products.

376 *2.2.2 Top of the Atmosphere (TOA) considerations – aerosol scattering in*
377 *the VNIR*

378 The TOA spectral radiance measured by an orbital remote sensing
379 instrument is a function of the wavelength-dependent illumination source (the
380 solar spectral irradiance), surface spectral bidirectional reflectance, and
381 atmospheric radiative transfer. Over the CRISM VNIR and CaSSIS wavelength range
382 Mars atmospheric radiative transfer is dominated by dust (*i.e.*, a ferric oxide
383 spectral signature) and water ice aerosols. Wolff et al (2009) derived the dust
384 aerosol radiative properties from 0.3 to 2.9 microns, in terms of the single

scattering albedo [*w*], using CRISM EPF observations acquired during the 2007 global dust event. The dust particle single scattering albedo spectrum, which is the fraction of incident light scattered by a single dust particle as a function of wavelength, shows strong spectral variation directly related to the dust composition (*i.e.*, absorption coefficient). Dust aerosols scatter more light at longer wavelengths (*w*(700 nm) ~ 0.97) than at shorter wavelengths (*w*(500 nm) ~ 0.82) (see Figure 12 in Wolff et al 2009). There is also a shallow decrease in the dust single scattering albedo with wavelength long-ward of 700 nm directly related to an increase of the dust aerosol absorption coefficient (see Figures 12 and 13 in Wolff et al 2009). The angular distribution of the light scattering from dust aerosols [*p(g)*] is anisotropic (*e.g.*, Ockert-Bell et al 1997) and consequently the observed scattering also depends on observation geometries. The direct consequence of the dust aerosol scattering contribution in the VNIR range is a reddening of surface signatures (*i.e.*, impose a ferric absorption), which can influence the calculation of surface spectral properties such as albedo and colour ratios from TOA spectra (see Figure 1 in Fernando et al 2017). This effect is governed by the quantity of dust in the atmosphere characterized by the optical depth [τ]. Water ice aerosols also moderate the surface signal but the estimation of the radiative effect on a given observation is complicated by their heterogeneous spatial and vertical distributions in the Martian atmosphere as a function of time.

CRISM observations used for the "fully"-simulated CaSSIS effort in this study were acquired with varying, but generally with favourable atmospheric conditions (see Table 2). The subset of observations with a high atmospheric dust and/or water ice optical depth (τ_{dust} > 1.0 @ 900 nm (Wolff et al 2009); τ_{ice} > 0.2 @ 320 nm (derived from MRO/MARCI data (Wolff, personal communication) must be used with caution, particularly when relating TOA spectral properties (*e.g.*, albedo, and band ratios and spectral parameters) to corresponding calculations applied to library spectra. In the CaSSIS data processing workflow, the EGN procedure accommodates the aerosol scattering anisotropy, but it is a TOA relative correction and so the C^4 data products have not been corrected to ground reflectance. Despite this, the variability in the C^4 and the fully-simulated CaSSIS data products (described in the next section) does accurately track intra-scene spectral/colour

surface variability (as opposed to atmospheric or photometric effects. However, due to the TOA nature of these products, an exact agreement with known mineral and phase spectral libraries is not generally expected. The magnitude of the surface vs. TOA discrepancy is directly governed by the atmospheric optical depth, and so is minimised in CRISM scenes acquired when the atmosphere is relatively clear (*e.g.,* FRT00003E12; see Table 2).

2.2.3 Creating a fully-simulated CaSSIS image cube

The majority of the MRO instrument datasets from CRISM, CTX, and HiRISE PDS data products are not orthorectified, and the MRO instrument teams use slightly different processing steps in the generation of map-projected products. Consequently, even MRO coordinated datasets do not overlay one another precisely. Therefore, image-to-image registration using a network of Ground Control Points (GCPs) must be used to co-register the datasets before they can be combined. This step is often an iterative process, if the topography of the scene is complicated.

Overall, GCP-based warping of CRISM-derived C^4 image cubes to 32-bit CTX (or HiRISE) calibrated I/F images resampled to 4.6m/pixel works well, especially for images with minimal topographic variability. During processing, we noticed that images with significant local-scale topographic variation were difficult to align. Therefore, iterative steps of addition and adjustment of GCPs between the CRISM-derived C^4 cube and the corresponding high-resolution panchromatic base image (*i.e.*, 32-bit CTX or HiRISE I/F) was necessary to improve alignment. After the initial selection of GCPs and warping, the warped C^4 image is carefully compared with the base image. This facilitates the identification of locations in the image that require adjustment to, or additional, GCPs to minimise misalignment/distortions and maximise the spatial pixel-to-pixel accuracy of the fused transformed and spatially resampled MRO datasets into a final fully-simulated CaSSIS image cube. This adjustment/addition of GCPs is followed by re-warping the original C^4 cube. This process can be repeated until the misalignment/distortion between the two datasets is minimised. Sufficiently accurate spatial co-registration is generally achieved after defining ~75-100 well-distributed GCPs for images with high-frequency topographic variability.

Once the CRISM-derived C^4 colour products are controlled to the spatially rescaled CTX (or HiRISE) image, a pan-sharpening method is used to combine them into a single cube. Pan-sharpening is a type of ground data processing and spacecraft data-volume/bandwidth saving technique that merges a higher spatial resolution grayscale panchromatic image with lower spatial resolution spectral images to create a higher-resolution colour image or multispectral image cube (*e.g.*, McEwen and Soderblom 1984). The Gram-Schmidt spectral sharpening transform (Laben and Bower 2000) is one of the most preferred pan-sharpening methods used for terrestrial datasets, specifically VNIR, and is employed here to create our final fully-simulated 4-band "CaSSIS" multispectral cube. Unlike many of the other pan-sharpening methods used today (*e.g.*, Hue-Saturation-Value – HSV), the Gram-Schmidt transform is a spectral pan-sharpening transform that retains the radiometrically calibrated I/F values of the input images while maximizing colour sharpness and keeping colour distortion to a minimum (Mauer 2013). The transform first simulates the panchromatic band or image (*i.e.*, CTX or HiRISE greyscale images) based on the lower spatial resolution spectral bands or image cube (*i.e.*, the CRISM-derived C^3 or C^4 products). Next, this lower spatial resolution simulated panchromatic band is used as the first band in a forward Gram-Schmidt transform. The first transformed band is then swapped out for the higher spatial resolution panchromatic band or image, and an inverse Gram-Schmidt transform is applied to generate the pan-sharpened spectral bands. The result is a spatially (4.6m/pixel) and spectrally (4-band) simulation of a CaSSIS image cube. Note that we calculate an additional CaSSIS band that we denote as "band 0" (see Table 1). This is a synthesized "blue" wavelength band, which is calculated in a similar fashion to the synthetic "blue" generated for HiRISE RGB images by using the HiRISE "BG" and "RED" bands (Delamere et al 2010). In the case of CaSSIS, the synthesized blue band is generated from the BLU and PAN bands. A detailed walkthrough of the various techniques used here to generate our fully-simulated CaSSIS image cube in ENVI/IDL is provided as part of our supporting online supplemental materials.

Individual CRISM VNIR full spatial resolution spectral bands have a SNR in the range of ~100 to ~500. The C^3 and C^4 data products integrate numerous CRISM

channels in the calculation of the compatible CaSSIS spectral bands. As a result, the C^3 and C^4 products have a significantly higher SNR (*c.f.*, Figures 3a and 3b with Figures 3c and 3d). Although a quantitative calculation of the SNR of fully-simulated CaSSIS image cubes have yet to be determined, it is likely that their SNR are marginally higher than what will be observed with real CaSSIS images. We also note that the SNR for the CaSSIS PAN band will be significantly higher than CTX (for a surface at comparable lighting and atmospheric conditions) and possibly for HiRISE as well (see Thomas et al and Roloff et al this issue).

2.2.4 Simulated CaSSIS image site selection

The Viviano-Beck et al (2014) study presents a summary of 31 type-spectra of minerals and phases on Mars using CRISM data and which have been compiled into the MICA (Minerals Identified through CRISM Analysis) spectral library. These 31 CRISM spectral type-localities are covered by 27 individual CRISM hyperspectral targeted observations (see Table 1 in Viviano-Beck et al [2014] for the specific mineral or phase, image ID, and associated reference(s), location, and corresponding best-matching analogue lab-measured mineral spectra).

[FIGURE 4]

In addition to these type-localities, coordinated MRO observations covering key sites that fall under the defined science theme groups of the CaSSIS team were selected for simulation, for a total of 181 simulated locations – including Phobos (Figure 4). The resulting set of simulated images generated for this paper is by no means comprehensive with respect to all the science themes and the many ongoing investigations of surface processes on Mars currently being conducted by other moderate- to high-resolution imagers (*e.g.*, HiRISE, CTX, HRSC and MOC). However, these set of simulations should provide ample examples demonstrating the anticipated colour and spatial capabilities of CaSSIS in the context of a few selected key investigations. Preference was given to sites and investigations where the colour and spatial abilities of CaSSIS need to be further tested (*e.g.*, resolving small scale features studied by HiRISE, such as Recurring Slope Lineae) and where it has been speculated that the extended colour capabilities would be particularly useful. The simulations provided here are meant to provide an idea of the strengths/limitations of the CaSSIS dataset returned

during the primary science phase and beyond, and to what extent CaSSIS will compliment and extend existing or concurrent datasets.

Lastly, we specifically note here that while some actual CaSSIS images have been acquired during a series of Mars Capture Orbit (MCO) imaging campaigns in November 2016 and February 2017 (see Pommerol et al 2016), and that some comparisons between simulated CaSSIS products and actual images are underway (Pajola et al 2017a), actual image radiometric and geometric calibration efforts are currently in progress (*e.g.*, Tulyakov et al 2017), and therefore the comparisons are beyond the scope of this paper. Furthermore, actual CaSISS images taken during MCO where taken on highly elliptical orbits, which do not provide a good test of the spatial capabilities of CaSSIS at its anticipated pixel-scale resolution.

3 Results

3.1 Fe-sensitivity with CaSSIS colour image products

Lab-derived spectra for forty-three ferrous iron-bearing, including mafic minerals, and fourteen ferric iron-bearing minerals were resampled to 4-point CaSSIS-convolved spectra (*i.e.*, BLU, PAN, RED and NIR). The hyperspectral lab spectra and CaSSIS-convolved spectra (*e.g.*, Figure 1) can be visually compared to one another to understand the spectral sensitivity that remains after convolution to the 4 bands of CaSSIS from the hundreds of bands of the lab spectra that cover the CaSSIS sensitivity range (~400-1100 nm). Referring back to Figure 1, we can observe that CaSSIS-convolved spectra for ferrous iron-bearing olivine and ferric iron-bearing nontronite are still quite distinguishable from one another, exhibiting strong spectral slopes toward the major absorption features associated with the presence of ferrous and ferric iron in these two example minerals, respectively. While additional comparisons of ferrous iron- (*e.g.*, pyroxenes) and ferric iron-bearing (*e.g.*, hematite, goethite, etc.) mineral/phase spectra show that it is not generally possible to identify a mineral or phase uniquely from 4-point CaSSIS spectra alone, it is nonetheless possible to distinguish ferrous iron- and ferric iron-bearing species from each other rather consistently.

[FIGURE 5]

This is further exemplified by plotting the CaSSIS-convolved ratioed band values based on multiple mineral/phase spectra on bivariate diagrams (*e.g.*, McEwen et al 2007; Delamere et al 2010), and provides another means of assessing the Fe-sensitivity of CaSSIS without having to plot and compare numerous spectra (Figure 5). The plots in Figure 5 show that Fe-bearing minerals behave in a predictable and consistent manner as a function of the CaSSIS band sensitivity to the known locations of absorptions, or a lack thereof. For example, a PAN/BLU ratio is used to highlight minerals and phases with a strong ferric iron (Fe^{3+}) absorption short of 550 nm (*e.g.*, Figure 1) by producing higher ratio values for minerals and phases that are dominated by ferric iron over ferrous iron (Fe^{2+}). We observe an expected greater spread in the value of ferric iron-bearing minerals and phases (mean: 2.11 std. dev.: 0.66) for this ratio because the absorption feature depth for ferric iron varies due to several factors (*e.g.*, mineral composition, grain size, etc.), whereas we see very little spread (mean: 1.11 std. dev.: 0.11) for the values for ferrous iron-bearing minerals and phases that generally lack an absorption feature short of 550 nm. Likewise, we see similar good discrimination behaviours with respect to the PAN/NIR ratio values, which is designed for highlighting minerals and phases with a strong ferrous iron (Fe^{2+}) absorption near 1000 nm, when comparing ferrous iron- vs. ferric iron-bearing minerals and phases.

Our analysis of the 57 CaSSIS-convolved lab-collected mineral and phase spectra shows that the four CaSSIS colour bands will provide ample sensitivity to Fe-bearing minerals that will rival the ability of HiRISE. This is due to the better SNR of CaSSIS and the splitting of the HiRISE NIR band into two IR bands for CaSSIS (*i.e.*, RED and NIR; see Table 1). This two NIR bands allow for an additional band ratio to be formulated (*i.e.*, RED/PAN) over HiRISE (Delamere et al 2010). The plots in Figure 5 and Table 3 provide a synthesis of the results and illustrate the most useful band ratio combinations for CaSSIS images, which we can use to achieve the best visual discrimination among the various Fe-bearing surface materials known to exist on Mars. To summarize, a PAN/BLU ratio (675 nm / 500 nm) provides the strongest discrimination between ferric iron- and ferrous iron-

574 bearing minerals followed by PAN/NIR (675 nm / 937 nm), and RED/PAN (836 nm
575 / 675 nm).

576 ### 3.2 Ice/Frost and/or Atmospheric Phenomena sensitivity with CaSSIS
577 ### colour image products

578 Although Figure 1 shows that CaSSIS should have some sensitivity to the
579 absorption around 1030 nm due to the presence of ice/frost, the broadband
580 nature of the 4 CaSSIS bands, and the fact that ferrous iron-bearing phases (Fe^{2+})
581 have a stronger absorption around ~1000 nm, poses issues for creating a CaSSIS-
582 derived band ratio or spectral parameter that will readily distinguish pixels that
583 are influenced ice/frost. Basically, a ratio that relies on the band depth of the NIR
584 band will more readily distinguish any ferrous iron-bearing materials in any given
585 scene over H_2O frost/ice. Therefore, any simple ratio using the NIR band will not
586 unambiguously isolate H_2O frost/ice in a scene that contains any ferrous iron
587 component.

588 **[FIGURE 6]**

589 Based on previous methods, single wavelength blue or blue-green image
590 and/or a red- or NIR-to-blue ratio (*e.g.*, James et al 1994; Bell et al 1997; Pelkey et
591 al 2007; Murchie et al 2009; Viviano-Beck et al 2014) have been used with some
592 success to isolate pixels containing a signature of ice/frost and/or atmospheric
593 phenomena in a given image (*e.g.*, see Figure 6). This is because the Martian dust,
594 which covers most of the surface, is bright, red and lacks blue due to a broad ferric
595 (Fe^{3+}) iron absorption over the blue wavelengths; whereas, ices and atmospheric
596 phenomena are also very bright, they do not generally lack blue (Figure 6a) (except
597 perhaps in cases where ice may be contaminated with Martian dust). The
598 remaining Martian surfaces that lack both dust and ice are generally bluer because
599 they generally lack ferric (Fe^{3+}) iron and possess a ferrous (Fe^{2+}) iron component.
600 However, similar to the discussion above, a simple red- or NIR-to-blue ratio alone
601 to isolate the signatures of ices or atmospheric phenomena will be confounded in
602 scenes where both materials are present (*e.g.*, Figure 6b). However, we note that
603 these dust- and ice-free surfaces have the very lowest reflectance or albedo values
604 on Mars (*e.g.*, Syrtis Major). This suggests that a multiband mean reflectance or
605 I/F intensity image (as a proxy for albedo) may be used to aid discrimination of

pixels influences by ice/frost and/or atmospheric phenomena. Unfortunately, natural variations in topography and observation geometries at high-resolution are an issue in a multiband mean reflectance or I/F intensity image as sun-lit light-toned bedrock and Martian dust-bearing surfaces may be just as bright as ice/frost and atmospheric phenomena (*e.g.*, Figure 6c). While a single band blue or blue-green image compared to a colour R-G-B image does a fairly good job at distinguishing ice/frost and atmospheric phenomena, a single band image will still contain illumination effects, which may cause some ambiguity and slow down analysis (*c.f.*, Figure 6a and 6d).

Although we find that each of the different suggestions summarized above cannot be used alone to readily and unambiguously distinguish ice/frost or atmospheric phenomena in images, we have determined a simulated CaSSIS spectral parameter that combines the individual strengths into a single spectral parameter that works exceptionally well, especially when compared to CRISM IR hyperspectral parameters for ices (Pelkey et al 2007; Murchie et al 2009; Viviano-Beck et al 2014) (*c.f.*, Figures 6e and 6f). The spectral parameter is created by dividing a mean multiband reflectance or I/F intensity image by a red- or NIR-to-blue ratio (*e.g.*, NIR/BLU, RED/BLU or PAN/BLU) image, and applying a min/max linear stretch (*e.g.*, Figure 6e). Figure 6e shows that the illumination effects are minimised and that the spectral parameter provides an excellent separation of ice/frost and atmospheric phenomena from other Martian surface components that is better than just a single wavelength blue or blue-green image alone (*c.f.*, Figures 6e and 6a). This separation also appears to be possible with a two-band image, one that includes the mean of the blue-green (BLU) band and at least one other CaSSIS band (PAN, RED or NIR), divided by a ratio of the two.

3.3 Suggestions for CaSSIS standard colour and band ratio colour composite image products

One hundred and eighty-one C^3 products were generated in this study, and of these 18 were not suitable to be processed as C^4 products (*i.e.*, CaSSIS colour-compatible products with the CRISM gimbaled/variable imaging geometry normalized to a reference observation geometry). As previously discussed in Section 2.2.1, this is due to an insufficient number of EPF segments associated

638 with a given CRISM targeted observations (*i.e.*, less than five). This also includes
639 the CRISM observation of Phobos (FRT00002992), which, despite the 'FRT' class
640 type, was acquired in a manner inconsistent with the geometric normalization
641 procedure. A total of 33 "fully" simulated CaSSIS image cubes were generated
642 (Table 2) based on C^4 products with the exception of one – the Mars Science Lab
643 (MSL) "Curiosity" landing site (FRS0028346). Only a C^3 product was possible for
644 this site as no EPF segments were acquired in association with this
645 CRISM targeted observation taken in early 2013. The 33 fully-simulated CaSSIS
646 cubes cover 30 unique locations on the Martian surface, as six of the cubes
647 represent change detection pairs for the "Inca City", "Arrakis" and Gasa crater
648 sites. A database/table (Table S1) including information on the 181 CRISM
649 observations is included in three formats (.csv, .xlsx and ESRI shapefile .shp) as part
650 of our supporting online supplementary materials, please see these resources and
651 the associated help file for more information on the observations used to generate
652 our CaSSIS simulated products.

653 Standard colour RGB band combination images, and Colour Band Ratio
654 Composites (CBRCs) for all simulated products were created as another tool to
655 assess the colour capability of CaSSIS towards differentiating various surface and
656 atmospheric components. With two near-infrared CaSSIS bands to choose from
657 (Table 1), we can create two IRB (*i.e.*, infrared-red-blue) infrared colour images,
658 which we refer to here as IRB1 and IRB2; these combinations correspond
659 specifically to simulated CaSSIS band combinations of 4-2-1 or NIR-PAN-BLU and
660 3-2-1 or RED-PAN-BLU in the R-G-B channels, respectively. The synthesized blue
661 wavelength band (*i.e.*, band 0) provides the means to produce a synthetic "true"
662 colour composite image that is similar to the HiRISE RGB (red-green-blue) product,
663 which is created with simulated CaSSIS products by combining the 2-1-0, or PAN-
664 BLU-"Blue", bands in R-G-B channels. Based on the results of our analysis of lab
665 spectra convolved to the CaSSIS instrument response functions, a CBRC
666 combination that combines simulated CaSSIS band ratios RED/PAN, PAN/BLU and
667 PAN/NIR in the R-G-B channels (we refer to this product as CBRC1) to maximize
668 the distinction of Fe-bearing minerals and phases; while for distinguishing ice/frost
669 or atmospheric phenomena and other surface materials, we recommend a CBRC

combination of PAN/BLU, PAN/NIR and Mean[BLU-NIR]/(NIR/BLU) in the R-G-B channels (we refer to this as CBRC2). Our analysis also indicates that a CBRC2 image that uses just the BLU band in the blue channel does an adequate job of distinguishing ice/frost or atmospheric phenomena from other surface materials, but the former spectral parameter provides better separation when available. All standard R-G-B images have a default 0.5% linear stretch applied to them, unless stated otherwise.

Figure 7 shows an example set of simulated CaSSIS colour image products based on CRISM observation FRT00003E12, which is the same CRISM observation that was used by Delamere et al (2010) as an example location for the effectiveness of HiRISE colour products to extend hyper- and multi-spectral datasets (*e.g.*, CRISM and THEMIS, respectively). As such, this is also an excellent example location for assessing both HiRISE and CaSSIS colour capabilities, as the Nili Fossae region of Mars is known for its mineral diversity and particularly for both spatially separated and distinctive ferrous- and ferric-bearing surface units. The CBRC1 combination employed here uses all four CaSSIS colour bands and is noted for providing extra sensitivity and discrimination of altered, ferric iron-bearing materials when compared to the band ratios used for a HiRISE CBRC image combination presented in Delamere et al (2010). The enhanced colour diversity and sensitivity brought out by the simulated CaSSIS CBRC1 image over the HiRISE CBRC is readily observed by comparing the one provided in Figure 7 with Figure 12 in Delamere et al (2010) (also see an additional example included in the Composition and Photometry section – section 3.5.1 – which covers the reported CRISM type-locality for the mineral talc). Furthermore, single-band ratio images that use a colour table to highlight pixels with the greatest band strength (bottom row of Figure 7), will be extremely useful as a proxy for exposure/concentration maps that may be utilized for extending orbital mineral mapping, but more importantly as a *in situ* exploration guide for landed missions.

[FIGURE 7]

The Fe-sensitivity of CBRC1 is not only supported by the above example, but by also analysing image-derived spectra extracted from the 4-band C^4 image cube based on CRISM FRT00003E12 (Figure 8). Here we extracted spectra for

coloured spectral units based on our CBRC1 product (see Figure 7) both before and after implementing a dark subtraction method in ENVI to mitigate issues with wavelength-dependent atmospheric scattering in each of the 4 bands. Despite the TOA nature of the image-derived spectra, the spectra extracted from the C^4 cube have the general shapes, slopes, and features expected based on the known spectral units and mineral matches for this location on Mars (see Mustard et al 2007, 2009; Tornabene et al 2008; Ehlmann et al 2008, 2009; Delamere et al 2010) and when compared to lab-derived spectra. The FRT00003E12 C^4 image derived spectra for Fe/Mg-bearing olivines and smectites are similar to the CaSSIS convolved lab-derived spectra shown (*c.f.*, Figure 7 and 1). However, this is only because there are minimal effects from dust and water-ice atmospheric contributions for these TOA spectra (see Table 2 and Figure 1 in Fernando et al [2017] for more details).

[FIGURE 8]

3.4 General results based on C^4 CaSSIS colour products and fully-simulated CaSSIS image cubes

Our 33 fully-simulated 5-band image cubes currently include 4 of 27 CRISM images covering the spectral mineral/phase type-localities presented in Viviano-Beck et al (2014), specifically for olivine/Mg-carbonate, talc, kaolinte, and low-calcium pyroxene (LCP).

[FIGURE 9]

Figure 9 shows a compilation of CBRC1s generated exclusively from simulated C^4 CaSSIS colour products based on 24 of the 27 CRISM images covering the spectral mineral/phase type-localities. Notably, the most diversely coloured CBRC1 images in the set (Figure 7 and Figures 9d, 9e, 9l-n, 9p, 9s-x) correspond to mineral localities or locations on Mars that contain excellent exposures of widespread Fe-bearing minerals and phases.

In general, the CBRC1 shows ferrous iron-bearing minerals in blue and ferric iron-bearing materials in yellow and orange. Although many of these localities show diverse colours consistent with abundant Fe-bearing minerals and phases, there are a few colour-diverse CBRC1 images shown in Figure 9 that show similar colour diversity that in some cases are actually due to a lack of spectral contrast (red coloured unit; also see spectrum in Figure 8) or a relative lack of Fe-bearing phases. In such cases, the lack of Fe-bearing materials results in minimal

736 contributions to the blue and green channels of the CBRC1 image; this results in a
737 strongly red or reddish-orange coloured unit. Examples of this include some
738 occurrences of Al-bearing smectites (Figure 9m-n) and chloride-bearing deposits
739 (Figure 9x). An additional example of chlorides with a strong red and orange colour
740 in our CBRC1 product is provided in the Composition and Photometry section
741 below (section 3.5.1).
742 **[FIGURE 10]**
743 Figure 10 shows an example of an infrared colour image constructed from
744 fully-simulated, 5-band and 4.6 m/pixel CaSSIS image using bands 4-2-1 (or NIR-
745 PAN-BLU) in R-G-B. For those that are familiar with HiRISE colour images, the
746 simulated CaSSIS IRB appears remarkably similar in colour to the HiRISE IRB
747 products for this site (see HIRISE IRB for PSP_002176_2025). The fully-simulated
748 cube was cropped for the figure to demonstrate the two anticipated swath width
749 modes planned for CaSSIS imaging (full-width: ~9.4 km; short-width: ~7.1 km) and
750 compared to the HiRISE full-swath width (~1.2 km). Additional discussion of this
751 example is provided in the Composition and Photometry section (section 3.5.1).
752 Although DTMs are not a focus of this simulation study, HIRISE and CTX
753 DTMs (when available), were resampled to 18.4-m post-spacing, which is based
754 on a simple 3-pixel solution for deriving elevation from stereo images (*e.g.*, Kirk et
755 al 2008). Figure 10 shows an example with the "mesh" function switched on in
756 ENVI; the mesh facilitates a comparison of the post-spacing pixel-scale of the DTM
757 in relation to surface/morphologic features. This illustrates a simple example of
758 what a 3D perspective using a CaSSIS colour image draped over a CaSSIS stereo-
759 derived DTM would look like, and how CaSSIS might provide constraints on the
760 geometry, thickness and 3D relationships (*e.g.*, stratigraphy) of surface units, and
761 thereby the relative timing of their formation, possible origins and modification
762 histories.
763

764 ## 3.5 Various examples of CaSSIS simulations by science theme

765 ### *3.5.1 Composition and Photometry*

766 Mars has a global surface composition that is more or less basaltic with a
767 high abundance of iron (*e.g.*, Christensen et al 2000; Bandfield et al 2001; Wyatt

et al 2002); furthermore, the ice-free surfaces of Mars can be generally divided into low albedo and high albedo surfaces, which strongly correlates with ferric iron-rich dust coverage, where, in general, the higher the dust coverage of the surface, the higher the albedo, and the redder the surface. Past and ongoing multi- and hyper-spectral VNIR and thermal infrared (TIR) instruments currently in orbit around Mars continue to provide more details into the mineral and phase compositional diversity of the surface at regional and local scales. The diverse minerals and phases of Mars can be generally categorized into primary/unaltered (mafic) and secondary/altered, or into groups (*e.g.*, Viviano-Beck et al 2014), such as: 1) primary mafic minerals and iron oxides; 2) sulphates; 3) phyllosilicates; 4) carbonates; and 5) halides and other silicates.

Although most of these groups were known to exist on Mars through the study of Martian meteorites (*e.g.*, McSween et al 2002), the first group to be identified spectrally on Mars was the primary mafic (*e.g.*, Adams 1968; McCord and Westphal 1971; Martin et al. 1996) and iron oxides group minerals (*e.g.*, Adams and McCord 1969; McCord et al 1977, 1978; Singer et al 1979). Although several minerals were suggested to exist on the Martian surface based on telescopic observations (*e.g.*, a ferric-bearing phase, pyroxenes, etc.), crystalline grey hematite, a common ferric iron-bearing mineral, was spectrally isolated in the Meridiani Planum region with hyper-spectral data from the Thermal Emission Spectrometer (TES) on the Mars Global Surveyor (Christensen et al 2000). This was followed by the isolation and identification of olivine spectra correlating to specific Fo# compositions (*i.e.*, Fosterite/Fayalite content) near Nili Fossae and Isidis Planitia (Hoefen et al 2003; Hamilton and Christensen 2005; Koeppen and Hamilton 2008; Tornabene et al 2008); however, the verification of the presence of other primary mafic minerals (*e.g.*, low and high Ca-pyroxenes, and high Ca-plagioclase) from orbit was based on the inclusion of these mineral spectra to properly model and spectrally unmix TES surface spectra (*e.g.*, Christensen et al 2000; Bandfield et al 2001).

Other groups of minerals, comprised mostly of secondary alteration phases, were in some cases inferred from the results of TES spectral analyses (*e.g.*,

799 Christensen et al 2001), but were not unambiguously identified until the advent of
800 higher spatial resolution spectrometers (*e.g.*, THEMIS, OMEGA and CRISM). The
801 emergent view of the occurrence of phyllosilicates on Mars, although observed to
802 be concentrated in some specific regions of Mars, is that they are generally
803 observed to be widespread amongst the oldest and most heavily cratered terrains
804 on Mars (*e.g.*, Wray et al 2008; Ehlmann et al 2011; Carter et al 2013; Ehlmann
805 and Edwards 2014). Whereas, concentrations of sulphates detected from orbit
806 occur in two major localities – the canyon system of Valles Marineris (*e.g.*, Bishop
807 et al 2009; Roach et al 2009) and the northern hemisphere circumpolar dunes of
808 Olympia Undae (*e.g.*, Langevin et al 2005; Calvin et al 2009); however, sulphates
809 are far more abundant and extensive on the surface of Mars based on the results
810 of surface investigations by Opportunity, Spirit, Phoenix and Curiosity (Christensen
811 et al 2003; Klingelhöfer et al 2003; Rieder et al 2003; Gellert et al 2006; Morris et
812 al 2006a, 2006b; Kounaves et al 2010; McLennen et al 2014). Chloride deposits
813 are observed to be scattered throughout the Noachian highlands of Mars
814 (Osterloo et al 2008; 2010), and are sometimes associated with phyllosilicate clays
815 (*e.g.*, Glotch et al 2010). The synthesis provided by Ehlmann et al (2011) shows
816 that Fe/Mg phyllosicate clays are the most abundant secondary/aqueous
817 alteration minerals identified, with Fe-poor minerals and phases generally being
818 the least abundant. This bodes well for CaSSIS as it will be most sensitive to the
819 Fe-bearing minerals and phases; however, the results of our simulations show that
820 some Fe-poor minerals can appear quite distinctive in colour, specifically in our
821 CBRC1 product. Due to a strong lack of absorptions from either ferrous or ferric
822 iron-bearing materials in some deposits, and certainly when they are juxtaposed
823 amongst a generally Fe-rich background, our CBRC1 product shows Fe-poor
824 minerals and phases, such as Al-bearing phyllosilicate clays and chloride deposits,
825 as strongly red or orange coloured units (also see Figures 9 m-n and 9x). Figure 11
826 shows an excellent example of the chloride-bearing deposits (reds and oranges)
827 reported by Osterloo et al (2008), which is observed to starkly contrast with
828 ferrous iron-bearing lavas and crater ejecta (blues). We not that their
829 distinctiveness in CBRC1 is non-unique, and thereby CaSSIS can only provide

830 further context for such minerals in cases where they have already been identified
831 in other datasets (*e.g.*, THEMIS, CRISM, etc.).

832 **[FIGURE 11]**

833 A synthesis of decades of spectral analyses now provides us not only with
834 the identification of key mineral and phase localities on the surface of Mars (see
835 Viviano-Beck et al 2014 and references therein), but also the locations of some of
836 the most spectral diverse regions on the planet (see recent summaries by Ehlmann
837 et al 2011; Carter et al 2013; Ehlmann and Edwards 2014). Amongst this body of
838 results, several surface features and regions stand out (*e.g.*, impact craters,
839 channels, valleys/grabens, Valles Marineris, Mawrth Vallis, Nili Fossae region,
840 etc.). These features and locations are anticipated to be highly valued targets for
841 the CaSSIS Composition and Photometry science theme. Herein below, we provide
842 a few fully-simulated CaSSIS examples of some of these features, and from these
843 regions, to demonstrate the capabilities we can expect from CaSSIS for
844 augmenting compositional studies of the Martian surface.

845 *Complex Crater Central Uplifts*

846 Orbital observations continue to reveal the morphologic, spectral and
847 structural complexity of complex crater central uplifts. Although Valles Marineris
848 (Viviano-Beck et al 2016) and other valleys or channels on Mars (*e.g.*, Wray et al
849 2016) provide some of the best subsurface bedrock exposures on Mars, they occur
850 over limited regions and the geometry of the exposures are not always conducive
851 to observation from above. The bedrock exposed in complex crater central
852 features, however, are uplifted, rotated (as much as 90°) and exposed at the
853 surface making them ideal for orbital observation from above. A study of over 200
854 observations of well-exposed central uplifts indicate that craters provide the most
855 globally widespread occurrence of bedrock exposures across Mars (*e.g.*,
856 Tornabene et al 2015). A study focusing on hundreds of complex crater uplift
857 observations revealed three distinct bedrock textural classes: 1) a fractured and
858 massive bedrock (FMB); 2) "mega"-brecciated bedrock (MBB); and 3) layered
859 bedrock (LB). Tornabene et al (2015) also summarized the types and stratigraphic
860 relationships of impact-related deposits and structures, including breccias, clast-

861 rich and clast-poor melt-bearing deposits, dykes, and both faulting and what
862 appears to be folding observed primarily in layered uplifts (see Caudill et al 2012).
863 Several of the best-exposed and most spectrally diverse central uplifts on Mars
864 have been the focus of detailed studies (Marzo et al 2010; Osinski et al 2011;
865 Quantin et al 2012; Skok et al 2012; Wulf et al 2012; Sun and Milliken 2014, 2015;
866 Nuhn et al 2014, 2015; D'Aoust 2015; Ding et al 2015; Hopkins et al 2016) spanning
867 topics that include: 1) crustal formation and alteration history; 2) impact-induced
868 alteration mechanisms (including hydrothermal); and 3) central uplift formation,
869 and the timing and emplacement of impactite deposits. CaSSIS is anticipated to
870 augment these studies through its stereo and colour capabilities, especially colour
871 coverage, and thereby provide an improved understanding the various topics
872 mentioned above.

873 **[FIGURE 12]**

874 Figure 12 shows a summary figure of cropped portions of fully-simulated
875 CaSSIS infrared colour images covering the various bedrock texture classes
876 (Tornabene et al 2015) associated with crater central uplifts. All three bedrock
877 types, including the layered type (LB), are resolved by the simulated CaSSIS
878 images. Figure 13 shows additional details provided by a fully-simulated CaSSIS
879 infrared colour image that covers the central peak of Ritchey crater. These
880 simulation shows us the colour diversity, coverage, and rendered 3D perspective
881 views, that we might expect from CaSSIS. Impactites (*e.g.*, impact melts and
882 breccias) and bedrock are readily resolved and recognized, in addition to their
883 stratigraphic relationships, thanks to the full-colour coverage and 3D perspective
884 provided by the CaSSIS simulation (*c.f.*, 3D and 2D provided in Figure 13). Some
885 impact-related structures and features appear to be resolvable in these
886 simulations, but these features, such as crater-related dykes and smaller meter-
887 scale lithic clasts and certainly better resolved by HiRISE. This brings up an
888 important point. Where colour may be vital for detailed geologic mapping of such
889 small-scale features, and where HiRISE colour coverage may be lacking or difficult
890 to achieve, the use of CaSSIS colour images over these features can be pan-
891 sharpened using available HiRISE grayscale images. This is not only desirable, but

892 highly recommended for not only impact-focused studies, but for other
893 investigations where contiguous high-resolution colour coverage is important
894 (*e.g.*, landing site analysis, etc.). The examples provided in Figures 12 and 13
895 demonstrate how the increased colour coverage provided by the wider swath
896 width of CaSSIS will provide clearer, and in many cases, better context then HiRISE.
897 This is especially true where colour is vital towards identifying and mapping
898 distinct impact-related geologic features and their stratigraphic relationships, and
899 thereby improve our understating of the formation of the timing and formation of
900 said features. To truly optimize studies and our understanding of the geology of
901 complex crater central uplifts, we recommend combining CaSSIS DTM, spectral
902 and colour coverage information with HiRISE and other datasets, such as CRISM
903 and THEMIS-derived thermal inertia.

904 **[FIGURE 13]**

905 *Possible methane producing regions on Mars*

906 Focused studies of regions on Mars known to contain olivine and
907 associated alteration minerals and phases, particularly serpentine, will be of key
908 importance to the ExoMars 2016 TGO mission. Figure 7 and Figure 10 covers a
909 unique, morphologically and spectrally diverse location in the Nili Fossae region
910 that has been the focus of several intense studies that have made use for all
911 available VNIR and TIR spectrometer datasets collected from Mars orbit to date
912 (Hoefen et al 2003; Hamilton and Christensen 2005; Mustard et al 2007, 2008;
913 Tornabene et al 2008; Ehlmann et al 2009; Delamere et al 2010). This site includes
914 widespread olivine-bearing deposits (Hamilton et al 2003; Hoefen et al 2003;
915 Hamilton and Christensen 2005; Tornabene et al 2008) juxtaposed with Fe/Mg
916 smectite-bearing deposits (*e.g.*, Mangold et al 2007; Mustard et al 2007, 2008;
917 Ehlmann et al 2009), Mg/Fe carbonates (Ehlmann et al 2008), and serpentine
918 (Ehlmann et al 2010). The presence of these minerals may be linked to methane
919 being produced as a geochemical by-product through the alteration of olivine-
920 bearing materials into serpentine (*e.g.*, Wray and Ehlmann 2011; Viviano-Beck et
921 al 2013) (also see review by Holm et al 2015). This location is a relevant test case
922 for the ExoMars-TGO mission because it was identified as one of several possible
923 transient/seasonal methane source regions (Mumma et al 2009). The simulated

924 CaSSIS images show the olivine-bearing, smectite-bearing, and carbonate-bearing
925 surface units as dark blue, orange/yellow, and greenish-yellow, respectively in the
926 CBRC1 image (Figure 7); and cyan, orange/yellow, light-cyan, respectively, in the
927 fully-simulated infrared colour image (Figure 10). Our example shows that the
928 mapping of these minerals detected by CRISM, will be readily extended by the
929 colour and spatial capabilities of CaSSIS by effectively providing a higher resolution
930 colour product and improved geologic context than CRISM or HiRISE colour could
931 provide alone. Colour mapping with HiRISE of this locality would require
932 mosaicking numerous narrow-swath HiRISE colour images, which are not easy to
933 obtain for large contiguous areas under similar observation geometries. Indeed,
934 the coverage required for HiRISE colour mosaicking for large areas are difficult to
935 plan and acquire and, hence has it seldom ever been done for even the highest
936 priority sites on Mars.

937 The study by Wray and Ehlmann (2011) also describe correlated
938 compositions and surface textures observed within the reported methane source
939 regions (Mumma et al 2009), including Nili Fossae. These regions are generally
940 comprised of older terrains cut by deep fractures and which do not appear to
941 include any evidence of younger volcanic activity. Many of the observed fractures
942 are likely ancient themselves, but a few are also found to be recent (as little as
943 ~10^5 years?) as they postdate small aeolian bedforms (Wray and Ehlmann, 2011).
944 CaSSIS monitoring of these fractured terrains for changes may reveal candidate
945 sources for any trace gas activity that other instruments aboard TGO might detect.
946 The broader colour coverage of CaSSIS will undoubtedly aid in this task, as HiRISE
947 has shown that surface changes can often be seen much more readily in colour
948 data (*e.g.*, McEwen et al 2010; also, see section 3.5.2 below). Although most
949 colour changes may reflect the removal and transport of surficial materials (dust,
950 sand), they may also indicate areas of new mineralization, which would be
951 expected from an active near-surface methane-generating serpentinization
952 processes.

953 Serpentine may be the most obvious mineral to look for in this context, but any
954 newly-fromed distinctly coloured aqueous minerals (*e.g.*, Wray and Ehlmann,

2011; Viviano-Beck et al 2013) may point to modern-day aqueous processes that might relate to contemporaneous trace gas activity. The detection of talc or chlorite may also be equally important, as discussed by Viviano-Beck et al (2013), as the chloritization of smectites may have provided the silica-rich fluids necessary for the serpentinization of olivine in the Nili Fossae area. Figure 14 shows a fully-simulated CaSSIS product that covers the CRISM spectral mineral/phase type-locality for the mineral talc. This compositionally diverse example again shows to what extent the full 4-colour capability of CaSSIS will not only enable, but greatly enhance detailed spectral mapping in this area. This example also demonstrates the effectiveness of the CaSSIS CBRC1 that uses all 4 CaSSIS bands, including both NIR bands, over a HiRISE-equivalent CBRC, which is limited to 3 bands and only a single NIR band (Figure 14). The anticipated result from such detailed spectral mapping augmented by CaSSIS colour/morphologic detail, will not only inform us on the general geologic history of methane-source regions such as this, but also place further constraints on the possible connection between surface/subsurface mineral reactions that may be a primary source of methane on Mars today.

[FIGURE 14]

It is clearly demonstrated through our simulations that CaSSIS will be ideal for documenting the compositional diversity of the Martian surface. This is due to fact that the 4 bandpasses of CaSSIS are sensitive to the VNIR spectral range, and that Mars hosts such a diversity of Fe-bearing minerals and phases, which produce key absorptions in this range that are related to the iron oxidation state and the coordination of iron in the specific mineral or phase. HiRISE has demonstrated similar colour capabilities over the last decade, providing the most diversely coloured images over regions with minimal contributions from surface dust (Delamere et al 2010; McEwen et al 2010). Indeed, the colour capabilities of HiRISE have also been used successfully to extend map compositional units at scales below those of these spectrometers (*e.g.*, Delamere et al 2010), and provide additional insights into the spatial relationships between different spectral units at a local scale. It is important to note that morphologic and stratigraphic context that are often not realized in just the spectral dataset alone, especially when

presented in a spectral parameter space calculated relative to the spectral continuum (*e.g.*, Pelkey et al 2007; Murchie et al 2009; Viviano-Beck et. 2014), which results in an image that appears "flat" because incidence effects have generally been generally divided out.

In summary, the CaSSIS examples shown here demonstrate that CaSSIS will provide a similar extension to spectral mapping, but with better coverage and spectral fidelity then HiRISE. The improved spectral sensitivity is provided by the "splitting" of the HiRISE IR band into two separate bands on CaSSIS (*i.e.*, RED and NIR; see Table 1). This added spectral capability is best exemplified by comparing a simulated CaSSIS CBRC1 with a HiRISE CBRC equivalent constructed from only 3 bands (see Figure 14; *c.f.*, Figure 7 and Figure 12 in Delamere et al [2010]). Compared to CaSSIS, HiRISE also has a smaller footprint (~5-6 km in width) and a more limited colour swath (Figure 10), which is ~20% of the HiRISE nominal image width (~1 to 1.2 km in width). This HiRISE colour-coverage limitation has always made it challenging to "hit" or maximise coverage of a colourful surface target, and has made it extremely challenging to plan, acquire and mosaic colour images over large sites of interest (*e.g.*, potential landing sites). Moreover, the length of a typical full-resolution HiRISE images is generally ~10 km, but typically no more than ~25 km. CaSSIS will be able to provide full-colour images that are just over ~1.5x the width, and up to ~4x the length of a typical HiRISE (~4x the length of the image in Figure 10). As such, CaSSIS provides improved colour coverage that is ~8 times greater than HiRISE per image. Extending the mineral/phase mapping of coarser-spatial resolution orbiting spectrometers to the spatial scale of CaSSIS will be necessary for investigating the link between surface composition, and particularly subsurface composition (*e.g.*, crater-excavated), and the origin of seasonal trace gases such as methane. These capabilities, in conjunction with the ability to acquire stereo images on a single orbit and produce DTMs from them, will facilitate a greater understanding of spectral units and their spatial relationships, and thereby greatly enhance composition and photometric investigations into key sites of interest on Mars, including those that are possible sources for transient methane in the atmosphere.

3.5.2 Change detection and Seasonal processes

Aeolian Processes

Aeolian bedforms (such as dunes and ripples) record the interaction between surface material and wind and provide important data about the past and current surface conditions, as well as the climate in which they formed and evolved (*e.g.*, Greeley and Iversen 1985). High spatial resolution HiRISE orthoimages combined with DTMs have allowed for the precise quantification of dune and ripple displacement rates and for an improved understanding of the evolution of bedforms under different Martian settings and conditions (Silvestro et al 2010; Bridges et al 2011, 2013; Ayoub et al 2012; Chojnacki et al 2014, 2015, 2016a; Cardinale et al 2016). However, many of these reports are only based on a few sets of observations separated by ~1-2 Mars-year intervals, and are spatially limited because of the relatively small HiRISE image footprint (~5-6 km). The more than double surface coverage of a CaSSIS image will provide the means to characterise broader-scale changes in dune fields, and possibly bedform migration, provided that the CaSSIS spatial resolution and length of the time-series will be sufficient to detect the changes.

Although bedform migration rates in many locations on Mars (e.g., Herschel crater, Gale crater) are frequently relatively low (~0.3-0.4 m/year) (Silvestro et al 2013; Cardinale et al 2016), and would require long time periods for detection, several locations with faster dunes are better candidates for monitoring by CaSSIS. Nili Patera is one of such location where ripples and dunes are observed to migrate rapidly (Silvestro et al 2010; Bridges et al 2012). To test the potential for future CaSSIS dune monitoring, we generated oversampled (4.6 m/pixel) orthorectified CTX images of the Nili Patera dune field to assess if CaSSIS would be able to spatially resolve changes resulting from dune migration observed with HiRISE stereo-derived DTMs and orthorectified images in previous studies.

Although the reported displacement at the Nili Patera dune field is on the order of, or less than, a CaSSIS or CTX pixel (<5 m; see Bridges et al 2012), we detect dune displacement as changes primarily associated with lightening and darkening between the two images at the top and the bottom of the slip face, and at the trailing edge of the windward face (see Figure 15 and animated GIFs

provided as part of our supporting online supplemental materials). These changes are highlighted by normalizing the difference between the two orthorectified images, which highlight the pixels with a largest change in the relative intensity between the two images. The normalized difference image is colour-coded and then stretched to highlight these pixels, essentially highlighting changes at both the lower (darkest) and upper (brightest) ends of the histogram. These changes reflect either a change in the surface tonality/albedo (*e.g.*, dark dune materials on the windward face moving to reveal an underlying brighter surface) or illumination. As a dune migrates, we observe Illumination changes on the slopes of slip face and near the dune crest, typically brightening along the base and darkening along the advancing crest due to a change in slope and thereby illumination. The southwest-facing slip faces of the Nili Patera dunes are illuminated due to the mid-afternoon timing of MRO observations. As the slip face advances towards the southwest, the illuminated slope also advances to the southwest. Pixels that previously covered parts of the dune with little to no slope in the before image, are now covering the base of the illuminated slope of the slip face. This is consistent with an observable brightening in the pixels near the base of the slip face in the southwest direction (*i.e.*, magenta leading-edge in Figure 15). There is also an observable darkening of pixels at the crest of the slip face (*i.e.*, blue edge in Figure 15). Essentially, the pixels that are now stoss-ward from the crest and where the slope faces away from the sun in the after-image, were once on the sun-facing slopes of the slip face in the before image. We also observe a brightening of pixels at the trailing edge of the stoss-ward face (*i.e.*, magenta training-edge in Figure 15). This is consistent with surface brightening in the pixels that occupy this area because as the dune advances the dark sands are being actively removed by saltation in this area, which reveals the underlying lighter-toned surface.

[FIGURE 15]

Based on the CTX orthoimages, which were acquired 7.5 Earth years (~4 Mars years) apart, the migration rate of the upwind (stoss) dunes is estimated to be ~1.1 m/year. We note that this rate is slightly higher than the rate measured for the same dunes from HiRISE orthoimages PSP_005684_1890, and

ESP_023353_1890 (~0.8 m/year), but these are only separated by just over half of the time frame of the CTX images used here. Another reason for the small discrepancy (~1 HiRISE pixel width) could be due to the greater spacecraft-jitter issues recorded in the CTX orthoimages, and/or an overestimation of dune displacements. Alternatively, the longer-baseline estimates could be larger due to the possibility of higher annual sand fluxes in the later years spanned by the oversampled CTX measurements (2007-2014), over the HiRISE-based observations (2007-2011). Indeed, large annual variations in sand fluxes that were described elsewhere on Mars (*e.g.*, Meridiani Planum; see Chojnacki et al 2016a) may be feasible here. In general, Nili Patera dunes have been shown to have relatively high rates with respect to other active dunes on Mars (Bridges et al 2013). Even then, only motion of the fastest dunes found in the stoss-ward section of the dune field is measurable at the oversampled 4.6 m/pixel resolution and a relatively long time-series or temporal baseline.

Without ongoing studies of the Nili Patera dune field and other zones of known active aeolian activity by HiRISE and CaSSIS, previous comparisons and estimation of rates remain somewhat speculative. With the spatial resolution, colour capability, and the ability to acquire stereo pairs on a single orbit, the new CaSSIS data will be able to continue to detect changes and provide refined estimated on dune migration on Mars given the acquisition of a time-series of images over a sufficient period (*i.e.*, several Martian years). Ripple movement detection will not likely be possible at CaSSIS resolution scales.

Recurring Slope Lineae (RSL)

Recurring Slope Lineae (RSL) are dark-toned linear features that initiate at bedrock outcrops and extend down steep slopes (McEwen et al 2011). Individual slopes may have hundreds of lineae, with widths up to 5 m and lengths as long as 1.5 km (McEwen et al 2014). RSL appear and lengthen gradually or incrementally, fade when inactive, and recur each year, normally in the warmest season (McEwen et al 2011). HiRISE has also detected newly-formed slumps associated with RSL fans in at least 7 locations (Chojnacki et al 2016b), which are now part of an ongoing investigation to understand these enigmatic seasonal features. These slumps begin, like RSL, as dark-toned features that are up to 30 m wide, which will

1113 be readily resolvable by CaSSIS. In some cases, RSL have been observed to leave
1114 behind bright or distinctly coloured deposits (Chojnacki et al 2016b). Seasonal RSL
1115 activity has been shown to be associated with the transient presence of hydrated
1116 salts, which strongly suggests that brines play some role in the formation (Ojha et
1117 al 2015). Recently, Dundas et al (2016) showed RSL are confined to angle-of-
1118 repose slopes or steeper (> 28°), indicating they are predominantly granular flows
1119 whose activity may be triggered by or somehow associated with small amounts of
1120 water. Transient uniform darkening of fans upon which the RSL form, such as in
1121 Valles Marineris, also occur (McEwen et al 2014) and may also be due to
1122 deliquescence of small amounts of water (Heinz et al 2016) or some, as of yet,
1123 unknown process.

1124 Given the width, and colour or relatively darker-tonality of these features,
1125 in addition to the SNR, the point-spread function (PSF) and pixel-scale (~4.6
1126 m/pixel) of CaSSIS, the largest observed lineae, and slopes with high densities of
1127 smaller RSL should be detectable. This is further supported by the fact that the
1128 largest RSL fans have been characterised with ~6 m/pixel CTX images (Chojnacki
1129 et al 2016b). Figure 16 provides a portion of a fully-simulated CaSSIS infrared
1130 colour image covering a portion of the RSL-monitoring site in the central uplift of
1131 Horowitz crater. A close-up image reveals several dark-toned slope streaks that
1132 are indeed HiRISE-confirmed RSL (*c.f.*, with Figure 1 in McEwen et al [2011]), which
1133 have been shown to have clear incremental seasonal growth through repeat
1134 imaging.

1135 **[FIGURE 16]**

1136 The time of day when RSL are most active remains unconstrained at this
1137 time. This is largely because MRO is in a Sun-synchronous orbit and can only
1138 observe in the middle afternoon – the driest time of day. However, the 74°-
1139 inclined polar orbit of TGO migrates through all local times ~1-2 times per Mars
1140 year, affording unique opportunities to image in the early morning hours when
1141 deliquescent liquids are most stable on the surface (Gough et al 2011). CaSSIS
1142 images will be vital towards testing the "deliquescence" hypothesis for the role of
1143 brines in the origin and evolution of RSL features via the detection of early-
1144 morning wet patches and their patterns in space and time. If the RSL or their fans
1145 are transiently dark due to deliquescence (*i.e.*, wetting), then this process is not

likely to be restricted to steep slopes; rather, it causes downhill flows (RSL) only on the steepest slopes. Therefore, a key goal for CaSSIS would be to detect transient dark patches at this earlier time of day. Unfortunately, CaSSIS can only re-image these locations in the afternoon several months before or after the morning images, so that seasonal changes will make the identification and characterization of diurnal changes difficult. Fortunately, a coordinated investigation with TGO and MRO can mitigate this issue. HiRISE and CTX can image these sites in the mid-afternoon hours within a couple of weeks of the CaSSIS early-morning images. New techniques in cross-instrument time-series change detection methods (*e.g.*, Unsalan and Boyer, 2004) will be used to create a consistent time-series set of images that uses camera models and DTMs as inputs; these inputs are specifically used to minimize the effects of distortions, different lighting conditions and different resolutions between the images in the set, and thereby facilitate cross-instrument change detection. This technique may also be used to study changes associated with the other features described in the remaining subsections below.

Active Gullies

The term "gully" is used on Mars to describe a kilometre-scale erosion-deposition system, where material is transported downslope via a channel. They are divided into three parts: an alcove, a transport-dominated channel and a depositional apron, or fan (Malin and Edgett 2000) where the materials of the fan materials are sourced from the wall into which the alcove formed. The results from the most comprehensive global survey utilizing CTX images at ~5-6 m/pixel indicate that well-developed gullies are found commonly on steep slopes at latitudes poleward of 30° in both hemispheres, and that there are tens of thousands of individual gullies located in at least 4861 separate sites (*e.g.*, craters, massifs, valleys, etc.) (Harrison et al 2015). Smaller gullies are also observed in equatorial regions with HiRISE images, some of which are commonly associated with RSLs (McEwen et al 2014; Auld and Dixon 2016). Gullies are found on steep slopes independent of slope type; hence, they are most commonly found on inner crater walls, but are also found on crater-rim slopes, valley walls, massifs, pits, dunes and slopes associated with both complex crater central peaks and pits (*e.g.*,

Balme et al 2006). Between 30-40° latitude in both hemispheres, gullies are almost exclusively pole-facing; poleward of 40°, gullies exhibit less of an orientation preference, but are generally more equator-facing (Harrison et al 2015; Conway et al 2017). When latitudinal variation is normalised as a function of the availability of steep slopes, no particular latitude appears to have a higher density of gullies than any other; they are, however, less common in areas with high concentrations of glacier-like landforms (Conway et al 2017). The orientation preference of gullies at certain latitude ranges (Harrison et al 2015; Conway et al 2017) strongly points to a link between the Martian climate and their formation (*e.g.*, Costard et al 2002).

Repeat imaging by MOC, CTX, and HiRISE continues to reveal that gullies are evolving under the present-day climate regime (Malin et al 2006; Diniega et al 2010; Dundas et al 2010, 2012, 2015, submitted; Harrison et al 2009; Raack et al 2015). This activity is quite common, with changes observed at 14% of non-dune monitoring sites in the southern hemisphere (Dundas et al 2015). Dune gullies are reported to be even more active (*e.g.*, Pasquon et al 2016) than gully sites that occur in bedrock and other deposits. The morphologic expression of active gullies includes the: **1**) appearance of metre-to-decametre scale failure scars in the source regions; **2**) evacuation/deposition of sediments on the order of metres deep from pre-existing channels; **3**) transport of metre-scale boulders; **4**) formation of new channels on fans; and **5**) formation of new deposits. The new deposits present the largest surface area (up to hundreds of metres wide and ~1 km in length) and range from digitate deposits with no detectable thickness at HiRISE-scale to metre-thick boulder-bearing lobes. These deposits can be light-, dark-, or neutral-toned relative to the surroundings, and are sometimes distinctive in colour. Of these HiRISE-detected changes, new deposits associated with gully activity are of a scale that are most likely observable by CaSSIS.

[FIGURE 17]

The gullies of Gasa crater are amongst the most highly active on Mars today. The gullies in Gasa crater are notable because of their very deeply incised alcoves (de Haas et al 2015; Okubo et al 2011) and accumulation of deposits over time which has led to the formation of very large fan deposits (relative to other

1210 gully fans on Mars) that have merged to become a bajada (Kolb et al 2010; Schon
1211 and Head 2012). At least 15 documented changes have been observed between
1212 2007–2016 (Dundas et al 2017); however, it is highly likely that all the gullies in
1213 the crater are active on timescales of a few decades or less.
1214 Here we present a two-image change detection time-series using two fully-
1215 simulated CaSSIS images of Gasa crater taken 2 years (~1 Mars year) apart, one
1216 from 2009 and the other from 2011 (Figure 17). Both pre-existing light- and dark-
1217 toned gully deposits are clearly visible in our simulated CaSSIS image (Figure 17a-
1218 e), in addition to the new dark gully deposits which appeared between 2009 and
1219 2011 (*c.f.*, with Figure 8 in Dundas et al 2012). Figure 17b and 17e shows new gully
1220 deposits, including one specific deposit in the northwestern corner, included and
1221 discussed in the studies by Dundas et al (2012; 2015). This deposit formed
1222 somewhere between L_S = 109–152° of Mars Year 30 (June 24–Sept. 20, 2010) and
1223 resulted in substantial topographic changes at the meter scale (see animated GIF
1224 included as part of our supporting online supplemental materials and Dundas et
1225 al [2012]), including lobate deposits and channel widening. Interestingly, the new
1226 deposit in the northwestern part of Gasa closely matches the background surface
1227 brightness in a greyscale HiRISE RED image (*i.e.*, its nearly invisible at red
1228 wavelengths), but is extremely distinctive in the colour swath of HiRISE (*c.f.*,
1229 Figures 8a and 8b in Dundas et al 2015). This deposit is also easily identified in our
1230 fully-simulated CaSSIS infrared colour image shown in Figure 17b. The
1231 distinctiveness in colour is attributed to NIR-band sensitivity to ferrous-bearing
1232 bedrock, originally documented by Okubo et al (2011), which can be seen exposed
1233 in the gully alcoves that have incised deeply into the carter wall of Gasa.
1234 In order to determine the process(es) responsible for new mass wasting
1235 events in gullies, it is important to understand both their seasonal timing and their
1236 relationship with seasonal volatiles (surface CO_2 or water frost). Repeat-imaging
1237 with HiRISE has revealed that the majority of monitored sites are active in the
1238 winter or early spring when CO_2 frost is present (Diniega et al 2010; Dundas et al
1239 2012, 2015; Raack et al 2015), but the appearances of some of the low-relief light-
1240 toned deposits are better correlated with the presence of H_2O frost (Vincendon
1241 2015), or small patches of CO_2 frost (Dundas et al submitted). With its narrow field

of view, HiRISE is not able to monitor many sites frequently – especially in colour; a handful of flows can be constrained to intervals of days or weeks, but most intervals between images span months or years.

The full-colour coverage over a ~9.4-km swath provided by CaSSIS will be ideal for readily detecting deposits like those observed in Gasa, which are most distinctive in colour IRB images. As such, new deposits detected by CaSSIS can be later followed up with HiRISE to document the finer meter-scale details. Our simulated CaSSIS time-series set of images covering Gasa crater also demonstrates that CaSSIS will be able to clearly detect changes associated with active mass wasting features, as demonstrated by our example in which a new feature is detected in the non-gullied southwestern crater wall (*c.f.*, Figure 17f and 17g). CaSSIS will also be ideal for looking for flows burying seasonal frost (*c.f.*, Dundas et al 2015). Furthermore, CaSSIS will be able to take images at different times of the day, which will allow us to determine whether transient morning/evening surface frosts are present at the sites of active gullies and monitor east-facing crater walls and slopes without the persistent shadowing that afternoon observations must contend with. Such observations with CaSSIS are anticipated provide vital inputs into models that will place further constraints on whether or not gullies are active via a "wet" or "dry" processes on Mars today (*e.g.*, Pilorget and Forget 2016).

New and recent impacts

Over five hundred new or recent impact sites on Mars have now been imaged by MOC, CTX, and HiRISE. These recent impact sites are most easily seen due to their large dark-toned blast zones, and are most easily detected in dusty regions by the MOC wide-angle camera and/or CTX, which are then imaged and confirmed subsequently by MOC narrow-angle camera and/or HiRISE (Malin et al 2006; Daubar et al 2013). HIRISE imaging shows that many of these recent impacts manifest as clusters of individual craters, which provides information on the strengths and densities of the impactor bodies that created them, impact incidence, and atmospheric thickness (*e.g.*, Ivanov et al 2009).

One of the most intriguing investigations into recent impacts on Mars revealed that they act as probes of subsurface ice in the mid- to high-latitude

regions (Byrne et al 2009; Dundas et al 2014). Based on studies of repeat imaging provided by HiRISE, the impact-exposed ice may remain bright and distinctly coloured for periods of months to years (Dundas and Byrne, 2010; Dundas et al 2014); this suggests that the ice is nearly pure, and not consistent with an ice-cemented regolith. In Figure 18, we compare a simulated CaSSIS image with a full-resolution HiRISE IRB image of a recent 20-m diameter impact crater showing bright deposits consistent with water-ice excavated by the crater (Dundas et al 2014). We can see in this comparative example that the simulated CaSSIS image reproduces most of the details of the crater that are visible to HiRISE. This includes the distribution of its dark-toned ejecta rays and, more significantly, the brighter icy deposits. This example demonstrates that CaSSIS will not only be able to support studies of current impact rates on Mars, but also provide constraints on the distribution of subsurface ice at the mid- to high-latitudes (*e.g.*, Daubar et al 2013; Dundas et al 2014). The distribution of ground ice serves as a proxy for the recent climate, integrated over the time required for ground ice to sublimate or deposit. The current extent of ice-exposing impacts acts as a lower limit on the extent of ground ice, which is more extensive than expected. This suggests an average atmospheric humidity somewhat higher than present (Byrne et al 2009; Dundas et al 2014), and/or some other factor(s) with an equivalent effect on ice stability. The larger than expected extent of ground ice in the northern hemisphere may also be inherited from previous climates rather than reflecting present day conditions making interpreting these results ambiguous. However, the southern ground ice boundary is not as sensitive to recent changes of orbital elements as that in the northern hemisphere (Chamberlain and Boynton 2007). Knowledge of the extent of the southern hemisphere ice boundary would thus help to resolve the ambiguity between the ice resulting from unexpectedly-humid present-day conditions versus being a relic of a previous climate that is unexpectedly slow to catch up to current conditions.

[FIGURE 18]

Like CTX, CaSSIS is expected to have sufficient spatial capability for detecting new impacts in dusty regions of Mars. Although it clearly has the advantages of colour and a slightly higher spatial resolution over CTX, the CaSSIS

areal coverage will be ~3 times narrower than CTX (~9.4 vs. 30 km swath width). Additionally, the TGO data rate may be much lower than that of MRO, which will likely limit CaSSIS surface coverage. As such, CTX is likely to remain the best dataset for finding new features due to its ability to provide extensive repeat coverage and global-mosaicking capabilities, while CaSSIS and HiRISE would be able to provide follow-up investigations of any new CTX-detected recent impact candidates (Malin et al 2006; Daubar et al 2013). One exception to this is observations over low-albedo regions, where CTX images are noisy, and recent impacts do not create a large contrasted spot on the surface. This includes the majority of the southern mid- to high-latitudes, where CaSSIS may be better suited to discover new icy impacts, which are needed to determine the ice table boundary in the southern hemisphere. Because CaSSIS will be able to resolve these new impacts well, it will be an excellent tool for monitoring the darkening and reddening of their ejecta as the surface-exposed ice sublimates.

Sublimation processes: Frosting/Defrosting

Every winter the polar regions of Mars are covered with a seasonal polar cap composed of CO_2 ice that extends down to latitudes of approximately 50° (Leighton and Murray 1966), with some patches of CO_2 frost forming closer to the equator under favourable conditions (Schorghofer and Edgett 2005). Seasonal CO_2 ice deposits can reach around one metre in thickness (Smith et al 2001), which during the spring sublimates, and thereby mobilizes sediment at the Martian surface (*e.g.*, Kieffer 2000). Despite the limited access to the poles due the TGO orbit being inclined 74°, CaSSIS will still have access to interesting regions with active seasonal processes shaping the terrain. With the ability to turn off-nadir, CaSSIS may be able to image near-polar targets as high as 75° latitude.

[FIGURE 19]

A rather distinctive example of seasonal sublimation-abetted sediment mobilisation features are araniforms, or "spiders", found in the south polar regions of Mars (Malin and Edgett 2001). Figure 19 illustrates a type-locality, dubbed "Inca City", where this morphologic feature commonly occurs. These landforms are thought to be caused by jets of gas escaping through cracks from the seasonal slab of CO_2 that forms on the surface in the winter months (Kieffer et

al 2006). These features are suggested to be produced by the increasing and more direct sunlight (higher sun elevation) with the progression of spring, which largely transmits through the translucent slab CO_2 ice, and thereby causes the underlying surface to differentially and drastically heat-up with respect to the overlying slab ice. This differential heating between the ice and surface results in vigorous sublimation at contact between the slab ice and surface, thereby initially trapping and pressurising the sublimated gas. When a weak spot in the ice ruptures due to the mounting pressure, fractures form conduits that allow the gas to escape; with repeated activity along these conduits, branching "channels" are carved into the surface that are quasi-radial to the initiation site giving rise to their distinctive dendritic or spider-like appearance (Kieffer 2000; Piqueux et al 2003; Kieffer et al 2006; Kieffer 2007). The escaping gas jets into the ambient atmosphere and deposits the surface material both locally as a dark spot and as a fan-shaped deposit with respect to the predominant direction of the wind or, in some cases, down local slopes. Dark spots and fans are clearly resolved in the simulated CaSSIS change-detection image pair, and some changes can also be discerned between the two images (Figure 19; see animated GIF included as part of our supporting online supplemental materials). Unfortunately, CaSSIS will not be able to resolve individual araniform fractures/channels that are resolved by HiRISE, so monitoring the changes of these features will specifically remain a HiRISE activity. However, CaSSIS will certainly be able to aid with systematic monitoring of their most prominent features – dark-toned spots and fans (as seen in Figure 19). New araniform detections and activity was recently aided by a HiRISE-based citizen science project. The project measured fan azimuths with the aim of using these features as a "weathervanes" for monitoring seasonal changes to local and regional wind directions (Aye et al 2016). CaSSIS image coverage and resolution would provide the means to readily extend such work since the fans are readily resolved at a decametre-scale.

The observation of an active plume remains a requirement to validate the aforementioned formation-model for araniforms. Such an observation has eluded HiRISE due to the sun-synchronous orbit of MRO, an afternoon observation time, and temporal repeatability of no less than 2 hours near the poles. Models suggest

1370 that the plumes are likely to be short-lived, and most active around noon. The
1371 capability of CaSSIS to image at various times of day, due to the orbital inclination
1372 of TGO, and the ability to capture a stereo pair mere minutes-apart, may enable
1373 observations of plumes jetting above the surface around that time of day.
1374 Although the "Inca City" site is outside the latitudes observable by CaSSIS, there
1375 are numerous araniform sites reported between 70°N and 75°N (*e.g.*, Piqueux et
1376 al 2003). One example is HiRISE image ESP_039781_1075, which is located at
1377 ~72.3°S – well within reach of a CaSSIS observation.
1378 **[FIGURE 20]**
1379 A similar sublimation process for producing araniform features is thought
1380 to be responsible for seasonal dark-toned deposits that manifest as "flows" and
1381 "spots" that are visible on frost coated sand dunes in the mid- to high-latitudes of
1382 both hemispheres (Malin and Edgett 2001; Hansen et al 2013). However, some
1383 workers have argued for a role of liquid brines instead of sublimation of seasonal
1384 frost to explain these features (*e.g.*, Kereszturi et al 2009). Figure 20 shows such a
1385 simulated CaSSIS change-detection pair location dubbed "Arrakis", which resolves
1386 multiple dark-toned spots and deposits at the base of the slopes of the dunes that
1387 appear to merge or grow between the season pairs (see animated GIF included as
1388 part of our supporting online supplemental materials). Although "Arrakis" is just
1389 beyond the reach of CaSSIS, a portion of the north polar erg observed between
1390 300°E and 350°E and below 75° is accessible to CaSSIS.
1391 Another example of an active seasonal process currently under
1392 investigation are changes associated with linear dune gully features (*e.g.*, Reiss
1393 and Jaumann 2003; Diniega et al 2013; Pasquon et al 2016). Linear dune gullies are
1394 peculiar landforms, which have only been identified on Mars, and are typified by
1395 those observed on the southwest-facing slip face of the Russell crater "mega"-
1396 dune site. Linear dune gullies are comparatively distinctive from other Martian
1397 gullies as they are characterized by an abbreviated alcove, and a long, narrow
1398 channel with little evidence of any terminal deposition. Such gullies have only
1399 been identified in the southern hemisphere of Mars and are thought to be
1400 restricted to ~33 locations at latitudes poleward of 35° (Pasquon et al 2016).
1401 Pasquon et al (2016) showed that these gullies are active towards the end of the

seasonal defrosting and suggested that changes may be episodic rather than incremental. One hypothesis explaining the formation of linear dune gullies entails the initial carving or lengthening of a gully channel from blocks of ice that dislodge themselves from shadowed cold traps in alcoves, which then sublimate as they travel downward on a largely defrosted and much warmer surface (Diniega et al 2013).

The simulated CaSSIS infrared colour image shown in Figure 21 resolves the dune gully alcoves and channels, and distinctive colours associated with both frost and sites of sublimation (*i.e.*, dark-toned spots and slope-streaks). The example clearly demonstrates that new channels and the lengthening of existing channels may be resolved clearly with CaSSIS. The extended CaSSIS colour coverage over HiRISE may help determine relationships between frosted surfaces and the active sites. Although highly unlikely, with the ability of CaSSIS to acquire stereo on a single orbit, it may be possible to observe the ice blocks while in motion down slope.

[FIGURE 21]

Studies of other seasonal changes associated with polar dunes also include the formation of new alcoves and associated debris aprons, and the erasure of older ones, which are typically undetectable with HiRISE in less than 3 years (Hansen et al 2011; Diniega et al 2017). An outstanding question of this study is: what is the driving mechanism for triggering sand avalanches that form new alcoves and fans? Is it simply aeolian degradation, or some other seasonal process driven by volatiles (Horgan and Bell 2012; Hansen et al 2015)? HiRISE already has 10 sites that are being actively monitored every year and that are within the latitudinal imaging limits of CaSSIS. A correlation between new alcove formation and regional snowstorms is currently under investigation (Hayne et al 2016). CaSSIS images will allow us to extend our temporal and spatial colour-coverage to a larger region for analysis. CaSSIS stereo-derived DTMs will help us to determine if some dunes are over-steepened by autumnal winds, and whether they are thus susceptible to sand avalanches. New alcoves detected with HiRISE can be quite large, as much as ~60 to 100 m wide, which will be readily detectable by CaSSIS.

In summary, the evolution of seasonal processes linked to defrosting and sublimation of surface ice can be monitored using CaSSIS images. Particularly useful will be the full colour-coverage, single-orbit acquisition stereo capabilities and the opportunity to image at different times of day. CaSSIS will enable improved constraints on the extent and rate of seasonal defrosting through full-colour coverage of the area covered by CO_2 frost over the span of several images taken in a seasonal time-series. The fact that that polar dunes are so active, in addition to being comprised of low-albedo materials, has made the extraction of HiRISE or CTX stereo-derived DTMs challenging, but CaSSIS offers full-colour, at a higher SNR, and stereo images that will be taken with very little time delay, which will vastly improve our ability to produce elevation and orthorectified time-series data products required to validate the changes observed between images.

3.5.3 Landing Sites and Future Exploration

One of the most important and fundamental mission objectives for Mars orbiters and their instrument payload is supporting the scientific exploration and engineering/safety of landed assets on the surface (*e.g.*, Golombek et al 2003, 2016; Grant et al 2011). This requires an assortment of datasets that generally provide information on surfaces properties that include*:* 1) geologic context/morphology (both context and high-resolution images); 2) topography/morphometry (elevation/slope); 3) composition (spectral and colour images); and 4) physical properties (thermal and/or radar). The uses of these datasets for this particular purpose generally entails a full-characterisation and synthesis of both the scientific merits of the site, as well as both the landing safety, traversability, and accessibility to sites of interest determined from orbit.

Indeed, one of three mission objectives for CaSSIS is to: "*certify and characterise safety and hazards (e.g., rocks, slopes, etc.) associated with candidate landing sites for ExoMars 2020, and other future surface missions*" (Thomas et al this issue). It is important to note that this particular supportive role not only entails pre-landing characterisation, but now also includes: 1) monitoring during the Entry Decent and Landing (EDL) phase (Phoenix and Curiosity); 2) observations of landing sites immediately following EDL (Spirit, Opportunity and Phoenix); 3)

1464 monitoring during the mission (Spirit, Opportunity, Phoenix and Curiosity); 4)
1465 observations of landing sites after the mission (Vikings 1 and 2, Pathfinder,
1466 Phoenix and Spirit); and 5) searching for and assessing what happened to "lost"
1467 missions to the surface (*e.g.*, Schiaparelli EDM, Beagle 2 and possibly Mars 3, etc.).
1468 Such collections of landing site images have provided vast insights into pre- syn-
1469 and post-mission activities (*e.g.*, McEwen et al 2010; Seelos et al 2014).

1470 EDL images can provide important insights into the events leading up to
1471 landing on Mars, while imaging of landing sites both before and after EDL provide
1472 the means to facilitate localization of our surface assets. The ability of HiRISE to
1473 resolve the landers/rovers themselves, in addition to rover tracks, have also been
1474 invaluable in these regards (*e.g.*, McEwen et al 2010; Golombek et al 2010, 2011;
1475 Geissler et al 2011; Arvidson et al 2015). High-resolution orbital images provide
1476 the best resource for determining both local- and regional-scale geologic context
1477 and for matching observations with rover/lander acquired panoramic image
1478 mosaics. This is not as easily accomplished with spectral and other types of
1479 datasets that are coarser resolution (*e.g.*, MOLA and THEMIS, etc.), but high-
1480 resolution orbital images may act as a "bridge" to match these coarser resolution
1481 datasets to that of the local-scale of the lander/rover. The augmented geologic
1482 context provided by the synthesis of the *in situ* investigations of by surface
1483 missions with orbital datasets, including decameter-scale geologic mapping of
1484 landing sites, have facilitated the long-term planning of active roving missions, and
1485 maximised the science return of both landed and roving missions alike (*e.g.*,
1486 Golombek et al 2003; McEwen et al 2010; Grant et al 2011). Meter- to decameter-
1487 scale elevation data derived from stereo images are critical towards assessing
1488 potential landing site hazards, and the traversability of a landing site and its
1489 surrounding regions for long-term planning and science investigations of complex
1490 features, such as the ejecta and rim-wall region of impact craters (*e.g.*, Golombek
1491 et al 2003; McEwen et al 2010).

1492 In this section, we provide simulated CaSSIS images as examples of past,
1493 current and future candidate landing sites. Although surface roughness and slope
1494 are two of the most important engineering parameters to assess during the

landing site proposal and selection stages (*e.g.*, Golombek et al 2003; Kirk et al 2003, 2008; Beyer and Kirk 2012; Fergason et al 2016), it is beyond the scope of this particular study to perform a full hazard and safety assessment of our simulated CaSSIS landing site images. Our goal is to simply assess the ability of anticipated CaSSIS images to resolve and characterise various aspects of a landing site, as well as provide site monitoring support for an active surface mission.

Before presenting and discussing our simulated CaSSIS images covering various landing sites, it is worth noting two examples of post-EDL imaging by CTX, which is a reasonable proxy for the spatial capabilities of CaSSIS as these two imagers have similar pixel-scales. The post-EDL imaging of the Phoenix lander is our first example. Figure S7 shows a close-up of a low emission angle (~0.5°) ~6 m/pixel CTX image taken on July 20th in 2008 of the Phoenix landing site, which resolves three dark spots and one bright one. Of the three dark spots, one is relatively larger than the other two, with the other two being more or less similar in size. One of these similar-sized dark spots (slightly lighter than the other) is associated with a nearby cluster of bright pixels, which are consistent with the backshell impact site and the parachute, respectively. The other similar-sized (slightly darker) dark spot is consistent with the impact site of the heatshield. The largest dark spot is attributed to the removal of unconsolidated, light-toned and fine-grained surface materials from the firing of the retrorockets of Phoenix lander during landing. A single darker pixel can be observed in the central region of the largest dark spot and is suggested to possibly represent the Phoenix lander. The lander when fully deployed is approximately 5.52 meters in diameter, so it is conceivable. If CTX had colour capabilities, like HiRISE and CaSSIS does, it may have been possible to determine if the dark pixel is indeed consistent with the lander, as solar panels are distinctive in the infrared colour image. Indeed, a rescaled HiRISE IRB image, using a pixel aggregate resampling algorithm to rescale to 4.6 m/pixel, shows a single blue pixel in the central region of the largest dark spot, which is consistent with subpixel mixing of the relatively dust-free solar panels of the Phoenix lander early on in the mission (Figure S7).

Our second CTX-based example is based on the post-EDL image of the ExoMars Schiaparelli EDL Demonstrator Module (EDM). Due to the fact that the

exact location of the EDM was initially unknown, and the large 30-km swath width of a CTX image, CTX was the first to document and observe surface changes associated with the components of the Schiaparelli EDM (see MRO-views of the Schiaparelli EDM Landing Site). Despite the high emission angle (~25°) and a ~6 m/pixel spatial resolution of the initial CTX image (see CTX image J08_47975_1779_02S006W), the location of surface changes associated with the four crucial components of the Schiaparelli EDM were resolved. This includes the parachute, the impact sites of the module, and both the rear (attached to the parachute) and front heatshields. The information provided by CTX, and the subsequent follow-up with HiRISE colour, in conjunction with spacecraft telemetry, were critical to the investigation of the EDL events that led to the demise of the Schiaparelli EDM.

These two above CTX examples indicate that CaSSIS will be able to resolve some of the aspects of future EDL events on Mars. Of course, the higher SNR and colour capabilities will provide additional benefits in this regard.

Landing Sites of Past and Current Missions

In this section, we describe three fully-simulated CaSSIS images of landing sites from past and ongoing missions.

Figure 22 shows portions of a fully-simulated CaSSIS infrared colour image constructed from a coordinated CRISM cube and CTX image of the Mars Exploration Rover (MER) "Spirit" landing site in Gusev crater, taken on the 15th of February 2010. This was just one month before Spirit fell silent near the location known as "Troy" (red star in Figure 22) just to the west of the ~90-m wide feature known as "Home Plate". This is the location where the rover got entrenched in unconsolidated deposits almost one year prior to when the CRISM-CTX-HiRISE image set was acquired. The Spirit rover landing site (orange star in Figure 22), rover, and rover tracks are not resolvable in the simulated CaSSIS image; however, numerous dust storm events, and dust devil activity since Spirit arrived at the Columbia Hills in 2006, likely erased any distinctive surface changes associated with the EDL and traverse of Spirit prior to its long-term science investigation at the "Home Plate".

[FIGURE 22]

Figure S8 shows a comparison of the coverage HiRISE IRB images and the surface coverage provided by a single fully-simulated CaSSIS infrared colour image, which is approximately 10 km at its narrowest (*i.e.*, close to the nominal 9.4 km swath width of CaSSIS). This comparison example demonstrates the challenges of obtaining HiRISE IRB coverage with reasonably similar observation angles, and the relative ease the CaSSIS full-colour swath-width will provide colour context. This is particularly relevant for this example, as the Columbia Hills and surrounding plans, which are an active site of change with respect to dust devil activity; as such, mosaics produced from images over active sites, and where sufficient time has elapsed between acquisitions, will suffer from multiple mismatches. The full-colour coverage of CaSSIS will provide more than 8x the colour coverage of a HiRISE colour image (~1-1.2 km wide), providing colour coverage and context for landing sites as well as other key sites of interest.

Figure 23 shows two fully-simulated CaSSIS images of the Curiosity MSL rover landing site. One of the landing site shortly after EDL, and including coverage of a portion of the long-term science target for MSL – Aeolis Mons (i.e., "Mount Sharp"). The fully-simulated CaSSIS image of Aeolis Mons, or Mount Sharp, provides a beautiful infrared colour context image that may prove useful for MSL long-term planning; indeed, the exploration of the Gale central mound is just beginning as of writing this paper. While, the post-EDL image of the Curiosity MSL rover taken in January of 2013, 5 months after landing, shows similarities to both the post-EDL CTX images of Phoenix lander (see Figure S7) and the Schiaparelli EDM images. Our fully-simulated CaSSIS image shows that the landing site, and the descent stage ("sky crane") multiple-impact site, can all be resolved with some detail. Unlike the previous Spirit rover example, rover tracks are indeed present and resolvable with full-resolution HiRISE images taken at the time of the MRO coordinated image set observations used for our simulation. As such, this particular fully-simulated CaSSIS image provides a better test to observe if the surface contrasts produced by rover tracks are sufficient to effect subpixel mixing to where they might be resolved. Unfortunately, and even when considering the larger size of MSL with respect to the MERs, neither the rover nor the rover tracks

1590 are resolvable in the simulated image. This is even the case when using the HiRISE
1591 RED mosaic image resampled to the CaSSIS pixel-scale instead of CTX. While it is
1592 not likely that CaSSIS will resolve landed assets on the Martian surface or rover
1593 tracks from its nominal 400-km orbit, it might be possible to resolve these features
1594 from a lower orbit. Resampling the HiRISE RED mosaic image to ~2 m/pixel shows
1595 that the rover tracks are discernible, which suggests that resolving such features
1596 might be possible in the event that the TGO orbit is adjusted to include a periapsis
1597 of ~200 km.

1598 **[FIGURE 23]**

1599 *Landing Sites for Future Missions: ExoMars 2020 and Mars 2020*

1600 In 2013, the ESA ExoMars 2020 landing site call was released to the
1601 scientific community, which included two overarching mission objectives: ***1)*** *to*
1602 *search for signs of past and present life on Mars; and* ***2)*** *to investigate the*
1603 *water/geochemical environment as a function of depth in the shallow subsurface.*
1604 To satisfy these requirement eight landing sites were suggested (seven located
1605 around Chryse Planitia, and one located on Isidis Planitia), all characterised by
1606 evidence in support of potentially long exposures to aqueous environments (*e.g.*,
1607 Erkeling et al 2013; Vago et al 2017; Pajola et al 2016a). At the time of writing this
1608 paper, only two of the three finalists from early 2017 (Bridges et al 2017) are
1609 currently under consideration. One is the Oxia Planum site, an extensive clay-
1610 bearing flat ~300 km across, located at the just south of the margin of the crustal
1611 dichotomy and Chryse Planitia (Carter et al 2016; Quantin et al 2016; Pajola et al
1612 2017b), and the other is situated amongst the well-exposed clay-bearing terrain
1613 of Mawrth Vallis (Gross et al 2016).

1614 Figure 24 shows a simulated CaSSIS synthetic "true" colour image and
1615 simulated CaSSIS CBRC1 image covering the southeastern portion of the Oxia
1616 Planum landing ellipse. In HiRISE images the "capping unit" and smectite clay-
1617 bearing unit, described by previous workers (Carter et al 2016; Quantin et al 2016),
1618 seems to have different VNIR colours than the majority of the surface. The
1619 "capping unit" manifests as a generally spectrally "bland", darker-toned crater
1620 retaining unit (also see Figure S9). Although the smectite clay-bearing unit does

not appear to be distinctive in our fully-simulated CaSSIS synthetic "true" colour (or infrared colour - not shown), the unit can be readily mapped as an orange unit in the simulated CBRC1 image (Figure 24). This is due to the ferric absorptions associated with the Fe-bearing smectites observed in CRISM data (Carter et al 2016; Quantin et al 2016). The CBRC1 orange unit is consistent with a subtle, light-toned beige unit (orange arrows) in the RGB image, which underlies the distinctive "capping unit". This and other examples herein clearly demonstrate that CaSSIS-based CBRC images are particularly useful for expanding the spectral mapping from CRISM (and other spectral datasets). We note that there are similar relationships between different colour units in Mawrth Vallis (Gross et al 2016) as the one described and shown here with the Oxia Planum example. That would be readily mapped out in CaSSIS images.

[FIGURE 24]

Following the definition of the scientific threshold criteria for the NASA Mars 2020 landing site call in 2013 (Mustard, Beaty and Bass 2013), multiple landing sites have been proposed (*e.g.*, Rice et al 2013; Edwards and Ehlmann 2015; Pajola et al 2016a, 2016b). The scientific selection criteria state that a candidate landing site must provide: *1) a geologic setting and history that can be characterised from orbit and in situ; 2) preservation of an ancient habitable environment; 3) access to samples with high biosignature preservation potential; and 4) returned samples of abundance, diversity, and quality that will be used to address questions regarding astrobiology; and planetary evolution*.

As of writing this paper, eight landing sites for Mars 2020 (see Golombek et al 2016b) have been narrowed down to 3 finalists by the scientific community. The currently favoured Mars 2020 landing site is Jezero crater (Figure S10), which is located in the Syrtis Major quadrangle. The crater is thought to have once been flooded with water, and currently contains a clay-bearing fan-shaped deposit that is consistent with a lacustrine delta (see Goudge et al 2015). This site is followed by: the northeast portion of Syrtis Major (*a.k.a.*, "NE Syrtis"), and the Columbia Hills within the Gusev crater basin (Figure 22). All eight sights going into the 3rd Mars 2020 landing site workshop, held in February of 2017, showed substantial scientific merit (Golombek et al 2016b). It is conceivable that one of the sites that

1653 did not make the final cut, sites such as Eberswalde crater (Figure S11), Mawrth
1654 Vallis (Figure S12), "Nili Fossae Trough" (Figures 9d, 25 and S13), Southwestern
1655 Melas Basin, and Holden crater, may still be considered over the next year or so
1656 based on any redeeming engineering safety merits.

1657 By combining the spatial and colour details with elevation data provided
1658 by CaSSIS, and synthesizing them with spectrometer data such as CRISM, we would
1659 not only greatly enhance the strategic and long-term planning of a rover mission,
1660 but improve on our ability for the rover to sample and cache the diverse
1661 compositions that are dispersed throughout a given landing site. As an example,
1662 we present a portion of a fully-simulated CaSSIS infrared colour image of the
1663 scoured deposits of the Hargraves ejecta blanket (Figure 25), which covers the
1664 eastern portion of the proposed Mars 2020 rover "Nili Fossae Trough" landing
1665 ellipse. The Hargraves crater ejecta, observed and described in brief by McEwen
1666 et al (2010), offers access to one of the best-exposed ejecta blankets on Mars. The
1667 ejecta exhibits a sharp juxtaposition of diverse "mega"-brecciated clasts and
1668 matrix materials comprised of the diverse target lithologies offered by the Nili
1669 Fossae region. The target materials of this region largely include unaltered, ferrous
1670 iron-bearing materials (pyroxene-bearing clasts and possible impact melt-bearing
1671 materials), and altered ferric iron-bearing materials consistent with Fe/Mg
1672 smectites, but also includes other alteration phases such as serpentine and
1673 carbonates. Both infrared colour and CBRC1 images in Figure 25 show sharp
1674 contacts between unaltered (blues in the CBRC1) and altered (yellows/oranges in
1675 the CBRC1) surface materials representing chemical redox gradients. Notably,
1676 these sharp redox boundaries have been shown to be important sites on Earth for
1677 sustaining metabolic processes for chemotrophic life (*e.g.*, De Marais et al 2003).
1678 CaSSIS is well-designed to map out these Fe-redox boundaries in detail and will
1679 thus provide support for planning *in situ* investigations, and sampling, of the best-
1680 candidate materials that may preserve biosignatures of chemophilic lifeforms.

1681 **[FIGURE 25]**

In summary, in addition to producing highly accurate DTMs (*e.g.*, Thomas et al this issue; Cremonese et al 2017) for assessing the engineering and safety constraints of landing sites, CaSSIS will provide some improvements over HiRISE towards the scientific characterisation of landing sites. This includes improved NIR-sensitivity, higher coverage in full-colour, and the means for rapid stereo completion and DTM production. The larger footprint and full-colour coverage will facilitate the extension of spectral and colour mapping needed to plan and explore within a landing ellipse or beyond (*i.e.*, "go to" sites of interest). In the past, it has been extremely difficult to acquire complete coverage of large landing ellipses with imagers that have small image footprints on the surface (MOC-NAC and HiRISE); thus, some landing site characterization studies have had to rely on staggered surface statistics (*e.g.*, the Insight lander; see Golombek et al 2016). CaSSIS has ~1.5x the width and up to 4x the length of a typical HiRISE image; as such, CaSSIS will improve our ability to cover and mosaic a landing ellipse and various surrounding sites of interest. The 4.6m/pixel full-colour and CBRC mosaics possible with CaSSIS will enable decameter-scale mapping, both morphologically and spectrally/thermophysically via the extension of coarser resolution datasets. These synthesized map products will provide invaluable geologic context. The synthesis and context provided by these products with with the *in situ* results from the suite of instruments included as part of the payload of the rover will augment long-term planning goals on an active mission, and maximise our understanding of the geologic history and potential habitability of the site being explored.

In the event of a future EDL failure, and assuming future landed hardware size and mass are similar to recent missions, a CaSSIS image immediately following the event would be able to answer several questions such as: **1)** Did the parachute open? and **2)** Did the heat shield and backshell separate? A "no" to the first question would likely result in an image of a single disturbed surface spot or small crater. If "yes", we would expect to see a few bright pixels representing the parachute on the surface. If "yes" for question two, we would see additional disturbed surface spots representing the impact sites for these components.

4 Summary & Conclusions

This study uses the instrument response function for the Colour and Stereo Surface Imaging System (CaSSIS) imager on the ExoMars Trace Gas Orbiter (TGO) to assess the sensitivity of the anticipated dataset to common phases on Mars identified by past orbiting and *in situ* platforms. This study also provides a methodology to produce a robusts simulation, both spectrally and spatially, of CaSSIS image cubes that are constructed from previously acquired and coordinated Mars Reconnaissance Orbiter (MRO) observations.

Using these simulated CaSSIS products, our analysis focuses on assessing the spatial and spectral performance and capabilities of CaSSIS, and provides insight into the best suggestions for higher-level derived colour data products to produce when real CaSSIS data are obtained. For example, prescribed sets of band-ratio colour composites are shown to enhance studies that are keen on identifying the spatial distribution of ferrous (Fe^{2+}) and ferric (Fe^{3+}) surface materials, as well as rapidly differentiating between ice/frost and atmospheric phenomena from other surface materials for seasonal, atmospheric and climatological studies (*e.g.*, haze, fog, clouds, dust devils, avalanche clouds, etc.). These simulations also demonstrate that CaSSIS images will continue to provide insight into spatial and temporal changes that occur due to various active surface phenomena (*e.g.*, seasonal deposition/sublimation of ices, gullies, RSL, dust avalanche streaks, dust devil tracks, landed/roving surface missions, etc.).

Despite the lower spatial resolution of CaSSIS when compared to HiRISE, this work demonstrates that CaSSIS will not only supplement HiRISE-scale investigations of various geological and seasonal phenomena, but enhance them by providing: **1**) additional geologic context with its wider and longer full-colour coverage; **2**) increased sensitivity to iron-bearing materials from two IR bands (RED and NIR) with the ability to produce colour band ratio composite images to facilitate mapping the spatial distribution and stratigraphic relations of compositionally diverse surface materials; **3**) greater flexibility in monitoring seasonal and recent recurrent changes due to variations in local time of image acquisition enabled by the TGO orbit; and **4**) near-simultaneous acquisition of stereo images (along-track stereo), which will ensure the stereo pairs are always

taken under similar atmospheric and illumination conditions, and perhaps even capture rapidly evolving processes "in action" (*e.g.*, dust devils, CO_2 jets, avalanches, etc).

Our simulated CaSSIS images demonstrate the detection of subtle surface changes that were either ambiguous or not sampled by the HiRISE colour swath or footprint (*e.g.*, Gasa crater active gullies, and additional dune movements in Nili Patera). This result demonstrates the power of the improved spatial colour-coverage of CaSSIS over HiRISE, as well as demonstrating that CaSSIS has sufficient resolving power to detect most surface changes currently being studied with HiRISE. However, we note that surface mission landers/rovers and rover tracks were not resolved in our simulated images. This clearly demonstrates the need for a full-colour sub-meter pixel-scale imager on a future orbiter (*e.g.*, on the Next Mars Orbiter - NeMO 2022) to enable the monitoring and tracking of future robotic, and possibly manned, missions to Mars.

Lastly, spectral pan-sharpening is commonly used for terrestrial datasets to mitigate data management and volume issues, or when there is a lack of coverage by other high-resolution colour imaging platforms. Indeed, the robustness of our methodology, and the resulting fully-simulated CaSSIS image cube product substantiates them as a stand-alone product, not just for the planning for the acquisition of real CaSSIS images and calibration efforts, but as a supplemental colour product for comparison and co-analysis with other Mars datasets. Fully-simulated CaSSIS image cubes may also be used to extend a time series set of images used for the monitoring of seasonal targets and change detection sites to the pre-TGO era (*i.e.*, fully-simulated CaSSIS cubes produced from coordinated MRO datasets spanning 2006 to present). These simulated products will provide the means to detect changes that occur over longer time-scales on Mars (*e.g.*, dune migration). Finally, we recommend that colour/spectral pan-sharpening of higher-resolution panchromatic grayscale images from CTX and HiRISE, beyond this simulation, would also be of great benefit to ongoing studies of the Martian surface. We note that the methodology detailed herein can be readily modified towards this specific goal. These products would be immediately useful where colour-coverage may be vital, and where HiRISE colour coverage is

specifically lacking or difficult to achieve. Indeed, the use of actual CaSSIS colour images to pan-sharpen available HiRISE RED mosaic grayscale images is not only desirable, but highly recommended for high-level investigations of the Martian surface, such as landing site characterisation, selection and exploration.

The results of this study indicate that the TGO mission objectives, as well as the instrument-specific mission objectives, will be achievable with CaSSIS.

Acknowledgements

The authors wish to thank the spacecraft and instrument engineering teams for the successful completion of the instrument. CaSSIS is a project of the University of Bern and funded through the Swiss Space Office via ESA's PRODEX programme. The instrument hardware development was also supported by the Italian Space Agency (ASI) (ASI-INAF agreement no.I/018/12/0), INAF/Astronomical Observatory of Padova, and the Space Research Center (CBK) in Warsaw. Support from SGF (Budapest), the University of Arizona (Lunar and Planetary Lab.) and NASA are also gratefully acknowledged.

The lead author wishes to personally acknowledge funding and support through the Planetary [ExoMars] Co-Investigator programme from the Canadian Space Agency (CSA) (14EXPUWO-002) and a Canadian NSERC Discovery Grant programme (RGPIN/04215-2014). A special thanks to the science and operations teams of the CRISM, CTX and HiRISE instruments, from which the spectacular coordinated datasets/images, which were required to simulate CaSSIS, would not be possible.

We would also like to acknowledge DTM technician Allison McGraw at University of Arizona for her contribution towards generating the HiRISE and CTX stereo-derived DTMs used in this study.

REFERNCES

Adams J. B., Lunar and martian surfaces: petrologic significance of absorption bands in the near-infrared. Science **159**, 1453-1455 (1968)

Adams J. B., McCord T. B., Mars: Interpretation of spectral reflectivity of light and dark regions. J. Geophys. Res. **74**(20), 4851-4856 (1969)

Adams J.B., Visible and near-infrared diffuse reflectance spectra of pyroxenes as applied to remote sensing of solid objects in the solar system. Journal of Geophysical Research **79**(32), pp.4829-4836 (1974)

Aharonson O., Zuber M.T., Smith D.E., Neumann, G.A., Feldman, W.C., Prettyman T.H., Depth, distribution, and density of CO2 deposition on Mars. Journal of Geophysical Research: Planets **109**, E5 (2004)

Appéré T. et al., Winter and spring evolution of northern seasonal deposits on Mars from OMEGA/Mars Express. J. Geophys. Res. **116**, E05001 (2011). http:// dx.doi.org/10.1029/2010JE003762

Arvidson, R.E., Bell, J.F., Catalano, J.G., Clark, B.C., Fox, V.K., Gellert, R., Grotzinger, J.P., Guinness, E.A., Herkenhoff, K.E., Knoll, A.H. and Lapotre, M.G.A., 2015. Mars Reconnaissance Orbiter and Opportunity observations of the Burns formation: crater hopping at Meridiani Planum. Journal of Geophysical Research: Planets, 120 (3), 429-451.

Auld, K. S., Dixon, J. C. (2016). A classification of martian gullies from HiRISE imagery. Planetary and Space Science, 131, 88-101.

Aye, K. M., Schwamb, M. E., Portyankina, G., & Hansen, C. J. (2016). Analysis Pipeline and Results from the PlanetFour Citizen Science Project. 47th Lunar and Planetary Science Conference abst. 3056.

Ayoub, F., Avouac, J.P., Newman, C.E., Richardson, M.I., Lucas, A., Leprince, S. and Bridges, N.T., 2014. Threshold for sand mobility on Mars calibrated from seasonal variations of sand flux. Nature communications, 5.

Bailen, M.S., Sucharski, R.M., Akins, S.W., Hare, T.M. and Gaddis, L.R., 2013, March. Using the PDS Planetary Image Locator Tool (PILOT) to Identify and Download Spacecraft Data for Research. In Lunar and Planetary Science Conference (Vol. 44, p. 2246).

Balme, M., Mangold, N., Baratoux, D., Costard, F., Gosselin, M., Masson, P., Pinet, P., Neukum, G., 2006. Orientation and distribution of recent gullies in the southern hemisphere of Mars: Observations from High Resolution Stereo Camera/Mars Express (HRSC/MEX) and Mars Orbiter Camera/Mars Global Surveyor (MOC/MGS) data. J. Geophys. Res. Planets 111, doi:10.1029/2005JE002607.

Bandfield, J.L., Hamilton, V.E. and Christensen, P.R., 2000. A global view of Martian surface compositions from MGS-TES. Science, 287(5458), pp.1626-1630.

Bell, J. F., Wolff, M. J., James, P. B., Clancy, R. T., Lee, S. W., & Martin, L. J. (1997). Mars surface mineralogy from Hubble Space Telescope imaging during 1994–1995: Observations, calibration, and initial results. Journal of Geophysical Research: Planets, 102(E4), 9109-9123.

Becerra, P., Byrne, S. and Brown, A.J., 2015. Transient bright “halos” on the South Polar Residual Cap of Mars: Implications for mass-balance. Icarus, 251, pp.211-225.

1845 Beyer, R. A., & Kirk, R. L. (2012). Meter-scale slopes of candidate MSL landing sites
1846 from point photoclinometry. Space science reviews, 170(1-4), 775-791.
1847 Bishop, J.L., Parente, M., Weitz, C.M., Noe Dobrea, E.Z., Roach, L.H., Murchie, S.L.,
1848 McGuire, P.C., McKeown, N.K., Rossi, C.M., Brown, A.J. and Calvin, W.M.,
1849 2009. Mineralogy of Juventae Chasma: Sulfates in the light-toned mounds,
1850 mafic minerals in the bedrock, and hydrated silica and hydroxylated ferric
1851 sulfate on the plateau. Journal of Geophysical Research: Planets, 114(E2).
1852 Bridges, J. C., Loizeau, D., Sefton-Nash, E., Vago, J., Williams, R. M. E., Balme, M.,
1853 ... & WG, E. L. S. S. (2017). Selection and Characterisation of the ExoMars
1854 2020 Rover Landing Sites. Lunar and Planetary Science 48, 1964, 2378.
1855 Bridges, N.T., Ayoub, F., Avouac, J.P., Leprince, S., Lucas, A. and Mattson, S., 2012a.
1856 Earth-like sand fluxes on Mars. Nature, 485(7398), pp.339-342.
1857 Bridges, N.T., Bourke, M.C., Geissler, P.E., Banks, M.E., Colon, C., Diniega, S.,
1858 Golombek, M.P., Hansen, C.J., Mattson, S., McEwen, A.S. and Mellon, M.T.,
1859 2012b. Planet-wide sand motion on Mars. Geology, 40(1), pp.31-34.\
1860 Bridges, N.T., Geissler, P., Silvestro, S. and Banks, M., 2013. Bedform migration on
1861 Mars: Current results and future plans. Aeolian Research, 9, pp.133-151.
1862 Burns, R.G., 1970. Mineralogical applications of crystal field theory, Cambridge
1863 University Press, New York.
1864 Burns, R. G. (1993). In Remote Geochemical Analysis: Elemental and Mineralogical
1865 Composition, edited by C.M. Pieters, and P.A.J. Englert, Cambridge
1866 University Press, 4, 3-29.
1867 Byrne, S., Dundas, C.M., Kennedy, M.R., Mellon, M.T., McEwen, A.S., Cull, S.C.,
1868 Daubar, I.J., Shean, D.E., Seelos, K.D., Murchie, S.L. and Cantor, B.A., 2009.
1869 Distribution of mid-latitude ground ice on Mars from new impact craters.
1870 Science, 325(5948), pp.1674-1676.
1871 Calvin, W.M., Roach, L.H., Seelos, F.P., Seelos, K.D., Green, R.O., Murchie, S.L. and
1872 Mustard, J.F., 2009. Compact Reconnaissance Imaging Spectrometer for
1873 Mars observations of northern Martian latitudes in summer. Journal of
1874 Geophysical Research: Planets, 114(E2).
1875 Cardinale, M., Silvestro, S., Vaz, D.A., Michaels, T., Bourke, M.C., Komatsu, G. and
1876 Marinangeli, L., 2016. Present-day aeolian activity in Herschel Crater, Mars.
1877 Icarus, 265, pp.139-148.
1878 Carter, J., Poulet, F., Bibring, J.P., Mangold, N. and Murchie, S., 2013. Hydrous
1879 minerals on Mars as seen by the CRISM and OMEGA imaging
1880 spectrometers: Updated global view. Journal of Geophysical Research:
1881 Planets, 118(4), pp.831-858.
1882 Carter, J., Quantin, C., Thollot, P., Loizeau, D., Ody, A. and Lozach, L., 2016, March.
1883 Oxia Planum: A Clay-Laden Landing Site Proposed for the ExoMars Rover
1884 Mission: Aqueous Mineralogy and Alteration Scenarios. In Lunar and
1885 Planetary Science Conference (Vol. 47, p. 2064).
1886 Caudill, C.M., Tornabene, L.L., McEwen, A.S., Byrne, S., Ojha, L. and Mattson, S.,
1887 2012. Layered MegaBlocks in the central uplifts of impact craters. Icarus,
1888 221(2), pp.710-720.
1889 Chamberlain, M.A. and Boynton, W.V., 2007. Response of Martian ground ice to
1890 orbit-induced climate change. Journal of Geophysical Research: Planets,
1891 112(E6).

Chojnacki, M., Burr, D.M. and Moersch, J.E., 2014. Valles Marineris dune fields as compared with other martian populations: Diversity of dune compositions, morphologies, and thermophysical properties. Icarus, 230, pp.96-142.

Chojnacki, M., Johnson, J.R., Moersch, J.E., Fenton, L.K., Michaels, T.I. and Bell, J.F., 2015. Persistent aeolian activity at Endeavour crater, Meridiani Planum, Mars; new observations from orbit and the surface. Icarus, 251, pp.275-290.

Chojnacki, M., Urso, A., Fenton, L. K., & Michaels, T. I. (2016a). Aeolian dune sediment flux heterogeneity in Meridiani Planum, Mars. Aeolian Research.

Chojnacki, M., A. McEwen, C. Dundas, L. Ojha, A. Urso, and S. Sutton (2016b), Geologic context of recurring slope lineae in Melas and Coprates Chasmata, Mars, J. Geophys. Res. Planets, 121, 1204–1231, doi:10.1002/2015JE004991.

Christensen, P.R., Bandfield, J.L., Smith, M.D., Hamilton, V.E. and Clark, R.N., 2000a. Identification of a basaltic component on the Martian surface from Thermal Emission Spectrometer data. Journal of Geophysical Research, 105(E4), pp.9609-9621.

Christensen, P.R., Bandfield, J.L., Clark, R.N., Edgett, K.S., Hamilton, V.E., Hoefen, T., Kieffer, H.H., Kuzmin, R.O., Lane, M.D., Malin, M.C. and Morris, R.V., 2000b. Detection of crystalline hematite mineralization on Mars by the Thermal Emission Spectrometer: Evidence for near-surface water. Journal of Geophysical Research: Planets, 105(E4), pp.9623-9642.

Christensen, P.R., Bandfield, J.L., Bell III, J.F., Gorelick, N., Hamilton, V.E., Ivanov, A., Jakosky, B.M., Kieffer, H.H., Lane, M.D., Malin, M.C. and McConnochie, T., 2003. Morphology and composition of the surface of Mars: Mars Odyssey THEMIS results. Science, 300(5628), pp.2056-2061.

Christensen, P., Wyatt, M., Glotch, T., Rogers, A., Anwar, S., Arvidson, R., . . . Wolff, M. (2004). Mineralogy at Meridiani Planum from the Mini-TES Experiment on the Opportunity Rover. Science, 306(5702), 1733-1739. Retrieved from http://www.jstor.org/stable/3839768

Christensen, P.R., Engle, E., Anwar, S., Dickenshied, S., Noss, D., Gorelick, N. and Weiss-Malik, M., 2009, December. JMARS-A Planetary GIS. In AGU Fall Meeting Abstracts (Vol. 1, p. 06).

Clark, R.N., Swayze, G.A., Gallagher, A.J., King, T.V. and Calvin, W.M., 1993. The US Geological Survey, Digital Spectral Library: Version 1 (0.2 to 3.0 um) (No. 93-592). Geological Survey (US).

Clark, R.N., Swayze, G.A., Wise, R., Livo, K.E., Hoefen, T., Kokaly, R.F. and Sutley, S.J., 2007. USGS digital spectral library splib06a. US Geological Survey, Digital Data Series, 231.

Conway, S.J., Harrison, T.N., Soare, R.J., Britton, A., Steele, L., 2017. Reanalysis of global data on orientation and slope of gullies on Mars. Geol. Soc. Lond. Spec. Publ. in review.

Costard, F., Forget, F., Mangold, N., Peulvast, J.P., 2002. Formation of recent Martian debris flows by melting of near-surface ground ice at high obliquity. Science 295, 110–113. doi:10.1126/science.1066698

Cremonese, G., Simioni, E., Re, C., Mudric, T., Lucchetti, A., Massironi, M., ... & Thomas, N. (2017). First Mars Surface Stereo Reconstruction with the

CaSSIS Stereo Camera. Lunar and Planetary Science Conference 48, 1964, 1464.

D'Aoust, Bianca, "Morphological, Structural and Spectral Mapping of the Central Uplifts of the Alga and Verlaine Craters, Mars" (2015). Electronic Thesis and Dissertation Repository. 3441. http://ir.lib.uwo.ca/etd/3441

Daubar, I.J., McEwen, A.S., Byrne, S., Kennedy, M.R. and Ivanov, B., 2013. The current martian cratering rate. Icarus, 225(1), pp.506-516.

de Haas, T., Conway, S.J., Krautblatter, M., 2015. Recent (Late Amazonian) enhanced backweathering rates on Mars: paracratering evidence from gully-alcoves? J. Geophys. Res. Planets 120, 2169–2189. doi:10.1002/2015JE004915

Delamere, W.A., Tornabene, L.L., McEwen, A.S., Becker, K., Bergstrom, J.W., Bridges, N.T., Eliason, E.M., Gallagher, D., Herkenhoff, K.E., Keszthelyi, L. and Mattson, S., 2010. Color imaging of Mars by the High Resolution Imaging Science Experiment (HiRISE). Icarus, 205(1), pp.38-52.

Des Marais, D. J., Nuth III, J. A., Allamandola, L. J., Boss, A. P., Farmer, J. D., Hoehler, T. M., ... & Spormann, A. M. (2003). The NASA astrobiology roadmap. Astrobiology, 8(4), 715-730.

Ding, N., Bray, V.J., McEwen, A.S., Mattson, S.S., Okubo, C.H., Chojnacki, M. and Tornabene, L.L., 2015. The central uplift of Ritchey crater, Mars. Icarus, 252, pp.255-270.

Diniega, S., Byrne, S., Bridges, N.T., Dundas, C.M., McEwen, A.S., 2010. Seasonality of present-day Martian dune-gully activity. Geology 38, 1047–1050. doi:10.1130/G31287.1

Diniega, S., Hansen, C.J., McElwaine, J.N., Hugenholtz, C.H., Dundas, C.M., McEwen, A.S. and Bourke, M.C., 2013. A new dry hypothesis for the formation of martian linear gullies. Icarus, 225(1), pp.526-537.

Diniega, S., C.J. Hansen, A. Allen, N. Grigsby, Z. Li, T. Perez, M. Chojnacki, Dune-slope activity due to frost and wind, throughout the north polar erg, Mars. Geol. Soc. London Spec. Pub., (2017) in press, doi:

Dundas, C.M., McEwen, A.S., Diniega, S., Byrne, S., Martinez-Alonso, S., 2010. New and recent gully activity on Mars as seen by HiRISE. Geophys. Res. Lett. 37, doi:10.1029/2009gl041351. doi:10.1029/2009gl041351

Dundas, C.M., Diniega, S., Hansen, C.J., Byrne, S., McEwen, A.S., 2012. Seasonal activity and morphological changes in martian gullies. Icarus 220, 124–143. doi:10.1016/j.icarus.2012.04.005

Dundas, C.M., Byrne, S., McEwen, A.S., Mellon, M.T., Kennedy, M.R., Daubar, I.J. and Saper, L., 2014. HiRISE observations of new impact craters exposing Martian ground ice. Journal of Geophysical Research: Planets, 119(1), pp.109-127.

Dundas, C.M., Diniega, S., McEwen, A.S., 2015. Long-Term Monitoring of Martian Gully Formation and Evolution with MRO/HiRISE. Icarus 251, 244–263. doi:10.1016/j.icarus.2014.05.013

Dundas, C.M., McEwen, A.S. and Milazzo, M.P., 2016, March. How wet is recent Mars? Insights from Gullies and RSL. In Lunar and Planetary Science Conference (Vol. 47, p. 2327).

Dundas, C. M., McEwen, A. S., Diniega, S., Hansen, C. J., Byrne, S., McElwaine, J. N. The formation of gullies on Mars today. Geol. Soc. London Spec. Pub., in press, doi:10.1144/SP467.5.

Edwards, C.S., Christensen, P.R. and Hamilton, V.E., 2008. Evidence for extensive olivine-rich basalt bedrock outcrops in Ganges and Eos chasmas, Mars. Journal of Geophysical Research: Planets, 113(E11).

Edwards, C.S. and Ehlmann, B.L., 2015, December. Carbon Sequestration on Mars: Constraints from the Nili Fossae Carbonate Plains. In AGU Fall Meeting Abstracts.

Ehlmann, B.L., Mustard, J.F., Murchie, S.L., Poulet, F., Bishop, J.L., Brown, A.J., Calvin, W.M., Clark, R.N., Des Marais, D.J., Milliken, R.E. and Roach, L.H., 2008. Orbital identification of carbonate-bearing rocks on Mars. Science, 322(5909), pp.1828-1832.

Ehlmann, B.L., Mustard, J.F., Swayze, G.A., Clark, R.N., Bishop, J.L., Poulet, F., Des Marais, D.J., Roach, L.H., Milliken, R.E., Wray, J.J. and Barnouin-Jha, O., 2009. Identification of hydrated silicate minerals on Mars using MRO-CRISM: Geologic context near Nili Fossae and implications for aqueous alteration. Journal of Geophysical Research: Planets, 114(E2).

Ehlmann, B.L., Mustard, J.F. and Murchie, S.L., 2010. Geologic setting of serpentine deposits on Mars. Geophysical research letters, 37(6).

Ehlmann, B.L., Mustard, J.F., Murchie, S.L., Bibring, J.P., Meunier, A., Fraeman, A.A. and Langevin, Y., 2011. Subsurface water and clay mineral formation during the early history of Mars. Nature, 479(7371), pp.53-60.

Ehlmann, B.L. and Edwards, C.S., 2014. Mineralogy of the Martian surface. Annual Review of Earth and Planetary Sciences, 42, pp.291-315.

Erkeling, G., Reiss, D., Hiesinger, H., Poulet, F., Carter, J., Ivanova, M.A., Hauber, E. and Jaumann, R., 2013. Two New Candidate Landing Sites for the European 2018 ExoMars Mission Near Libya Montes Alluvial Fans, In Lunar and Planetary Science Conference, (Vol. 44, p. 2378)

Fergason, R.L., Kirk, R.L., Cushing, G., Galuszka, D.M., Golombek, M.P., Hare, T.M., Howington-Kraus, E., Kipp, D.M. and Redding, B.L., 2016. Analysis of Local Slopes at the InSight Landing Site on Mars. Space Science Reviews, pp.1-25.

Fernando, J., Schmidt, F., & Douté, S. (2016). Martian surface microtexture from orbital CRISM multi-angular observations: A new perspective for the characterization of the geological processes. Planetary and Space Science, 128, 30-51.

Fernando, J., Douté, S., McEwen, A., Byrne, S., Thomas, N. (2017). Mars atmospheric dust contamination of surface albedo and color measurements. In Lunar and Planetary Science Conference, vol. 48, p. 1635. 2014.

Fonti, S., and Marzo, G. A. (2010). Mapping the methane on Mars. Astronomy & Astrophysics, 512, A51.

Formisano, V., Atreya, S., Encrenaz, T., Ignatiev, N., & Giuranna, M. (2004). Detection of methane in the atmosphere of Mars. Science, 306(5702), 1758-1761.

Gendrin, A., Mangold, N., Bibring, J.P., Langevin, Y., Gondet, B., Poulet, F., Bonello, G., Quantin, C., Mustard, J., Arvidson, R. and LeMouélic, S., 2005. Sulfates

in Martian layered terrains: the OMEGA/Mars Express view. Science, 307(5715), pp.1587-1591.
Gellert, R., et al. (2006), Alpha particle X-ray spectrometer (APXS): Results from Gusev crater and calibration report, J. Geophys. Res., 111, E02S05, doi:10.1029/2005JE002555.
Geissler, P.E., Sullivan, R., Golombek, M., Johnson, J.R., Herkenhoff, K., Bridges, N., Vaughan, A., Maki, J., Parker, T. and Bell, J., 2010. Gone with the wind: Eolian erasure of the Mars Rover tracks. Journal of Geophysical Research: Planets, 115(E7).
Glotch, T.D., Bandfield, J.L., Tornabene, L.L., Jensen, H.B. and Seelos, F.P., 2010. Distribution and formation of chlorides and phyllosilicates in Terra Sirenum, Mars. Geophysical Research Letters, 37(16).
Golombek, M.P., Grant, J.A., Parker, T.J., Kass, D.M., Crisp, J.A., Squyres, S.W., Haldemann, A.F.C., Adler, M., Lee, W.J., Bridges, N.T. and Arvidson, R.E., 2003. Selection of the Mars Exploration Rover landing sites. Journal of Geophysical Research: Planets, 108(E12).
Golombek, M., Robinson, K., McEwen, A., Bridges, N., Ivanov, B., Tornabene, L. and Sullivan, R., 2010. Constraints on ripple migration at Meridiani Planum from Opportunity and HiRISE observations of fresh craters. Journal of Geophysical Research: Planets, 115(E7).
Golombek, M., Grant, J., Kipp, D., Vasavada, A., Kirk, R., Fergason, R., Bellutta, P., Calef, F., Larsen, K., Katayama, Y. and Huertas, A., 2012. Selection of the Mars Science Laboratory landing site. Space science reviews, 170(1-4), pp.641-737.
Golombek, M., Kipp, D., Warner, N., Daubar, I.J., Fergason, R., Kirk, R.L., Beyer, R., Huertas, A., Piqueux, S., Putzig, N.E. and Campbell, B.A., 2016a. Selection of the InSight landing site. Space Science Reviews, pp.1-91.
Golombek, M.P., Grant, J.A., Farley, K.A., Williford, K., Chen, A., Otero, R.E. and Ashley, J.W., 2016b, March. Downselection of landing sites proposed for the Mars 2020 Rover Mission. In Lunar and Planetary Science Conference (Vol. 47, p. 2324).
Gough, R.V., Chevrier, V.F. and Tolbert, M.A., 2016. Formation of liquid water at low temperatures via the deliquescence of calcium chloride: Implications for Antarctica and Mars. Planetary and Space Science, 131, pp.79-87.
Grant, J.A., Golombek, M.P., Grotzinger, J.P., Wilson, S.A., Watkins, M.M., Vasavada, A.R., Griffes, J.L. and Parker, T.J., 2011. The science process for selecting the landing site for the 2011 Mars Science Laboratory. Planetary and Space Science, 59(11), pp.1114-1127.
Greeley, R., and Iversen, J.D., 1985, Wind as a geological process on Earth, Mars, Venus and Titan: Cambridge Planetary Science Series 4: Cambridge, Cambridge University Press, 333 p.
Hamilton, V.E. and Christensen, P.R., 2005. Evidence for extensive, olivine-rich bedrock on Mars. Geology, 33(6), pp.433-436.
Hansen, C.J., Bourke, M., Bridges, N.T., Byrne, S., Colon, C., Diniega, S., Dundas, C., Herkenhoff, K., McEwen, A., Mellon, M. and Portyankina, G., 2011. Seasonal erosion and restoration of Mars' northern polar dunes. Science, 331(6017), pp.575-578.

Hansen, C.J., Byrne, S., Portyankina, G., Bourke, M., Dundas, C., McEwen, A., Mellon, M., Pommerol, A. and Thomas, N., 2013. Observations of the northern seasonal polar cap on Mars: I. Spring sublimation activity and processes. Icarus, 225(2), pp.881-897.

Hansen, C.J., Diniega, S., Bridges, N., Byrne, S., Dundas, C., McEwen, A. and Portyankina, G., 2015. Agents of change on Mars' northern dunes: CO_2 ice and wind. Icarus, 251, pp.264-274.

Hare, T.M., Akins, S.W., Sucharski, R.M., Bailen, M.S. and Anderson, J.A., 2013, March. Map projection web service for PDS images. In Lunar and Planetary Science Conference (Vol. 44, p. 2068).

Harrison, T. N. , Malin, and K. S. Edgett (2009), Present-day Gully Activity Observed by the Mars Reconnaissance Orbiter (MRO) Context Camera (CTX), Bulletin of the American Astronomical Society 41, 3, 113, abstract 57.03.

Harrison, T.N., Osinski, G.R., Tornabene, L.L., Jones, E., 2015. Global Documentation of Gullies with the Mars Reconnaissance Orbiter Context Camera and Implications for Their Formation. Icarus 252, 236–254. doi:10.1016/j.icarus.2015.01.022

Hayne, P.O., Hansen, C.J., Byrne, S., Kass, D.M., Kleinböhl, A., Piqueux, S., McCleese, D.J., Diniega, S. and Portyankina, G., 2016. SNOWFALL VARIABILITY AND SURFACE CHANGES IN THE POLAR REGIONS OF MARS. LPI Contributions, 1926.

Heinz, J., Schulze-Makuch, D., & Kounaves, S. P. (2016). Deliquescence-induced wetting and RSL-like darkening of a Mars analogue soil containing various perchlorate and chloride salts. Geophysical Research Letters, 43(10), 4880-4884.

Hoefen, T. M., Clark, R. N., Bandfield, J. L., Smith, M. D., Pearl, J. C., & Christensen, P. R. (2003). Discovery of olivine in the Nili Fossae region of Mars. Science, 302(5645), 627-630.

Holm, N.G., Oze, C., Mousis, O., Waite, J.H. and Guilbert-Lepoutre, A., 2015. Serpentinization and the formation of H2 and CH4 on celestial bodies (planets, moons, comets). Astrobiology, 15(7), pp.587-600.

Hopkins, R.T., Tornabene, L.L. and Osinski, G.R., 2017. The central uplift of Elorza Crater: Insights into its geology and possible relationships to the Valles Marineris and Tharsis regions. Icarus, 284, pp.284-304.

Horgan, B.H. and Bell, J.F., 2012. Seasonally active slipface avalanches in the north polar sand sea of Mars: Evidence for a wind-related origin. Geophysical Research Letters, 39(9).

Hunt, G. R., and Salisbury, J. W., 1970, Visible and near-infrared spectra of minerals and rocks—I. Silicate minerals, Modern Geology, v. 1, p. 283-300.

Hunt, G.R., 1977. Spectral signatures of particulate minerals in the visible and near infrared. Geophysics, 42(3), pp.501-513.

Hunt, G.R. and Ashley, R.P., 1979. Spectra of altered rocks in the visible and near infrared. Economic Geology, 74(7), pp.1613-1629.

Ivanov, B.A., Melosh, H.J., McEwen, A.S., HiRISE Team, 2009. Small impact crater clusters in high resolution HiRISE images – II. Lunar Planet. Sci. 40. Abstract 1410.

James, P. B., Clancy, R. T., Lee, S. W., Martin, L. J., Singer, R. B., Smith, E., ... & Zurek, R. W. (1994). Monitoring Mars with the Hubble space telescope: 1990-1991 observations. Icarus, 109(1), 79-101.

Kieffer, H.H., 2000, August. Annual punctuated CO2 slab-ice and jets on Mars. In Second International Conference on Mars Polar Science and Exploration (Vol. 1, p. 93).

Kieffer, H.H., Christensen, P.R. and Titus, T.N., 2006. CO2 jets formed by sublimation beneath translucent slab ice in Mars' seasonal south polar ice cap. Nature, 442(7104), pp.793-796.

Kieffer, H.H., 2007. Cold jets in the Martian polar caps. Journal of Geophysical Research: Planets, 112(E8).

Kirk, R.L., Howington-Kraus, E., Redding, B., Galuszka, D., Hare, T.M., Archinal, B.A., Soderblom, L.A. and Barrett, J.M., 2003. High-resolution topomapping of candidate MER landing sites with Mars Orbiter Camera narrow-angle images. Journal of Geophysical Research: Planets, 108(E12).

Kirk, R. L., Howington-Kraus, E., Rosiek, M. R., Anderson, J. A., Archinal, B. A., Becker, K. J., ... & Holmberg, I. M. (2008). Ultrahigh resolution topographic mapping of Mars with MRO HiRISE stereo images: Meter-scale slopes of candidate Phoenix landing sites. Journal of Geophysical Research: Planets, 113(E3).

Klingelhöfer, G., Morris, R., Bernhardt, B., Schröder, C., Rodionov, D., De Souza, P., . . . Arvidson, R. (2004). Jarosite and Hematite at Meridiani Planum from Opportunity's Mössbauer Spectrometer. Science, 306(5702), 1740-1745. Retrieved from http://www.jstor.org/stable/3839769

Koeppen, W.C. and Hamilton, V.E., 2008. Global distribution, composition, and abundance of olivine on the surface of Mars from thermal infrared data. Journal of Geophysical Research: Planets, 113(E5).

Kolb, K.J., McEwen, A.S., Pelletier, J.D., 2010. Investigating gully flow emplacement mechanisms using apex slopes. Icarus 208, 132–142.

Kounaves, S. P., Hecht, M. H., Kapit, J., Quinn, R. C., Catling, D. C., Clark, B. C., ... & Shusterman, J. (2010). Soluble sulfate in the martian soil at the Phoenix landing site. Geophysical Research Letters, 37(9).

Kereszturi, A., Möhlmann, D., Berczi, S., Ganti, T., Horvath, A., Kuti, A., Sik, A. and Szathmary, E., 2010. Indications of brine related local seepage phenomena on the northern hemisphere of Mars. Icarus, 207(1), pp.149-164.

Laben, C.A. and Brower, B.V., Eastman Kodak Company, 2000. Process for enhancing the spatial resolution of multispectral imagery using pan-sharpening. U.S. Patent 6,011,875.

Langevin, Y., Poulet, F., Bibring, J.P. and Gondet, B., 2005. Sulfates in the north polar region of Mars detected by OMEGA/Mars Express. Science, 307(5715), pp.1584-1586.

Leighton, R.B. and Murray, B.C., 1966. Behavior of carbon dioxide and other volatiles on Mars. Science, 153(3732), pp.136-144.

Malin, M.C., Edgett, K.S., 2000. Evidence for recent groundwater seepage and surface runoff on Mars. Science 288, 2330–2335. doi:10.1126/science.288.5475.2330

Malin, M.C. and Edgett, K.S., 2001. Mars global surveyor Mars orbiter camera: interplanetary cruise through primary mission. Journal of Geophysical Research: Planets, 106(E10), pp.23429-23570.

Malin, M.C., Edgett, K.S., Posiolova, L.V., McColley, S.M., Dobrea, E.Z.N., 2006. Present-day impact cratering rate and contemporary gully activity on Mars. Science 314, 1573–1577.

Mangold, N., Poulet, F., Mustard, J.F., Bibring, J.P., Gondet, B., Langevin, Y., Ansan, V., Masson, P., Fassett, C., Head, J.W. and Hoffmann, H., 2007. Mineralogy of the Nili Fossae region with OMEGA/Mars Express data: 2. Aqueous alteration of the crust. Journal of Geophysical Research: Planets, 112(E8).

Martin, P.D., Pinet, P.C., Bacon, R., Rousset, A. and Bellagh, F., 1996. Martian surface mineralogy from 0.8 to 1.05 µm TIGER spectro-imagery measurements in Terra Sirenum and Tharsis Montes formation. Planetary and space science, 44(8), pp.859-888.

Maurer, T., 2013. How to pan-sharpen images using the Gram-Schmidt pan-sharpen method-a recipe. International Archives of the Photogrammetry, Remote Sensing and Spatial Information Sciences, 1, p.W1.

McCord, T. B. and Westphal, J. A., 1971. Mars: narrow-band photometry from 0.3 to 2.5 microns of surface regions during the 1969 apparition. Astrophys. J. 168, 141-153.

McCord, T. B., Huguenin, R. L., Mink, D. and Pieters, C. M., 1977. Spectral reflectance of martian areas during the 1973 opposition: Photoelectric filter photometry 0.33-I. IO pm. Icarus 31, 25-39.

McCord, T. B., Clark, R. N. and Huguenin, R. L., 1978. Mars: Near-infrared spectral reflectance and compositional implication. J. Geophys. Res., 83(Bll), 5433-5441.

McLennan, S.M., Anderson, R.B., Bell, J.F., Bridges, J.C., Calef, F., Campbell, J.L., Clark, B.C., Clegg, S., Conrad, P., Cousin, A. and Des Marais, D.J., 2014. Elemental geochemistry of sedimentary rocks at Yellowknife Bay, Gale crater, Mars. Science, 343(6169), p.1244734.

McSween, H.Y., 2002. The rocks of Mars, from far and near. Meteoritics & Planetary Science, 37(1), pp.7-25.

McEwen, A. S., & Soderblom, L. A. (1984). High-resolution color images of Io. LUNAR AND PLANETARY SCIENCE XV, P. 529. Abstract.

McEwen, A.S., Eliason, E.M., Bergstrom, J.W., Bridges, N.T., Hansen, C.J., Delamere, W.A., Grant, J.A., Gulick, V.C., Herkenhoff, K.E., Keszthelyi, L. and Kirk, R.L., 2007. Mars reconnaissance orbiter's high resolution imaging science experiment (HiRISE). Journal of Geophysical Research: Planets, 112(E5).

McEwen, A.S., Banks, M.E., Baugh, N., Becker, K., Boyd, A., Bergstrom, J.W., Beyer, R.A., Bortolini, E., Bridges, N.T., Byrne, S. and Castalia, B., 2010. The high resolution imaging science experiment (HiRISE) during MRO's primary science phase (PSP). Icarus, 205(1), pp.2-37.

McEwen, A.S., Ojha, L., Dundas, C.M., Mattson, S.S., Byrne, S., Wray, J.J., Cull, S.C., Murchie, S.L., Thomas, N. and Gulick, V.C., 2011. Seasonal flows on warm Martian slopes. Science, 333(6043), pp.740-743.

McEwen, A.S., Dundas, C.M., Mattson, S.S., Toigo, A.D., Ojha, L., Wray, J.J., Chojnacki, M., Byrne, S., Murchie, S.L. and Thomas, N., 2014. Recurring

slope lineae in equatorial regions of Mars. Nature geoscience, 7(1), pp.53-58.

McLennan, S. M., Anderson, R. B., Bell, J. F., Bridges, J. C., Calef, F., Campbell, J. L., ... & Des Marais, D. J. (2014). Elemental geochemistry of sedimentary rocks at Yellowknife Bay, Gale crater, Mars. Science, 343(6169), doi:10.1126/science.1244734.

Morris, R. V., et al. (2006a), Mössbauer mineralogy of rock, soil, and dust at Gusev crater, Mars: Spirit's journey through weakly altered olivine basalt on the plains and pervasively altered basalt in the Columbia Hills, J. Geophys. Res., 111, E02S13, doi:10.1029/2005JE002584.

Morris, R. V., et al. (2006b), Mössbauer mineralogy of rock, soil, and dust at Meridiani Planum, Mars: Opportunity's journey across sulfate-rich outcrop, basaltic sand and dust, and hematite lag deposits, J. Geophys. Res., 111, E12S15, doi:10.1029/2006JE002791.

Mumma, M. J., Villanueva, G. L., Novak, R. E., Hewagama, T., Bonev, B. P., DiSanti, M. A., ... & Smith, M. D. (2009). Strong release of methane on Mars in northern summer 2003. Science, 323(5917), 1041-1045.

Murchie, S., Arvidson, R., Bedini, P., Beisser, K., Bibring, J.P., Bishop, J., Boldt, J., Cavender, P., Choo, T., Clancy, R.T. and Darlington, E.H., 2007. Compact reconnaissance imaging spectrometer for Mars (CRISM) on Mars reconnaissance orbiter (MRO). Journal of Geophysical Research: Planets, 112(E5).

Mustard, J.F., Poulet, F., Head, J.W., Mangold, N., Bibring, J.P., Pelkey, S.M., Fassett, C.I., Langevin, Y. and Neukum, G., 2007. Mineralogy of the Nili Fossae region with OMEGA/Mars Express data: 1. Ancient impact melt in the Isidis Basin and implications for the transition from the Noachian to Hesperian. Journal of Geophysical Research: Planets, 112(E8).

Mustard, J.F., Murchie, S.L., Pelkey, S.M., Ehlmann, B.L., Milliken, R.E., Grant, J.A., Bibring, J.P., Poulet, F., Bishop, J., Dobrea, E.N. and Roach, L., 2008. Hydrated silicate minerals on Mars observed by the Mars Reconnaissance Orbiter CRISM instrument. Nature, 454(7202), pp.305-309.

Mustard, J.F., Ehlmann, B.L., Murchie, S.L., Poulet, F., Mangold, N., Head, J.W., Bibring, J.P. and Roach, L.H., 2009. Composition, morphology, and stratigraphy of Noachian crust around the Isidis basin. Journal of Geophysical Research: Planets, 114(E2).

Ockert-Bell, M. E., J. F. Bell, J. B. Pollack, C. P. McKay, and F. Forget (1997), Absorption and scattering properties of the Martian dust in the solar wavelengths, J. Geophys. Res., 102, 9039–9050, doi:10.1029/96JE03991.

Ojha, L., Wilhelm, M.B., Murchie, S.L., McEwen, A.S., Wray, J.J., Hanley, J., Massé, M. and Chojnacki, M., 2015. Spectral evidence for hydrated salts in recurring slope lineae on Mars. Nature Geoscience, 8(11), pp.829-832.

Okubo, C.H., Tornabene, L.L., Lanza, N.L., 2011. Constraints on mechanisms for the growth of gully alcoves in Gasa crater, Mars, from two-dimensional stability assessments of rock slopes. Icarus 211, 207–221.

Osinski, G.R., Tornabene, L.L. and Grieve, R.A., 2011. Impact ejecta emplacement on terrestrial planets. Earth and Planetary Science Letters, 310(3), pp.167-181.

Osterloo, M.M., Hamilton, V.E., Bandfield, J.L., Glotch, T.D., Baldridge, A.M., Christensen, P.R., Tornabene, L.L. and Anderson, F.S., 2008. Chloride-bearing materials in the southern highlands of Mars. Science, 319(5870), pp.1651-1654.

Osterloo, M.M., Anderson, F.S., Hamilton, V.E. and Hynek, B.M., 2010. Geologic context of proposed chloride-bearing materials on Mars. Journal of Geophysical Research: Planets, 115(E10).

Oze, C. and Sharma, M., 2005. Have olivine, will gas: Serpentinization and the abiogenic production of methane on Mars. Geophysical Research Letters, 32(10).

Pajola, M., Rossato, S., Baratti, E., Mangili, C., Mancarella, F., McBride, K., & Coradini, M. (2016a). The Simud–Tiu Valles hydrologic system: A multidisciplinary study of a possible site for future Mars on-site exploration. Icarus, 268, 355-381.

Pajola, M., Rossato, S., Carter, J., Baratti, E., Pozzobon, R., Erculiani, M. S., ... & McBride, K. (2016b). Eridania Basin: An ancient paleolake floor as the next landing site for the Mars 2020 rover. Icarus, 275, 163-182.

Pajola, M., Simioni, E., Lucchetti, A., Re, C., Cremonese, G., Thomas, N., Pommerol, A., Tornabene, L. & the CaSSIS Team (2017a). Refining the boundary between the Phobos Blue/Red spectral units with the ExoMars-CaSSIS imagery. European Planetary Science Congress 2017, Vol. 11, EPSC2017-68-1.

Pajola, M., Rossato, S., Baratti, E., Pozzobon, R., Quantin, C., Carter, J., & Thollot, P. (2017b, in press). Boulder abundances and size-frequency distributions on Oxia Planum-Mars: Scientific implications for the 2020 ESA ExoMars rover. Icarus.

Pasquon, K., Gargani, J., Massé, M., Conway, S.J., 2016. Present-day formation and seasonal evolution of linear dune gullies on Mars. Icarus 274, 195–210. doi:10.1016/j.icarus.2016.03.024

Pelkey, S.M., Mustard, J.F., Murchie, S., Clancy, R.T., Wolff, M., Smith, M., Milliken, R., Bibring, J.P., Gendrin, A., Poulet, F. and Langevin, Y., 2007. CRISM multispectral summary products: Parameterizing mineral diversity on Mars from reflectance. Journal of Geophysical Research: Planets, 112(E8).

Pilorget, C., & Forget, F. (2016). Formation of gullies on Mars by debris flows triggered by CO2 sublimation. Nature Geoscience, 9(1), 65-69.

Piqueux, S., Byrne, S., & Richardson, M. I. (2003). Sublimation of Mars's southern seasonal CO2 ice cap and the formation of spiders. Journal of Geophysical Research: Planets, 108(E8).

Planetary Data System (PDS), Geosciences Node, Spectral Library: http://speclib.rsl.wustl.edu/, accessed 2017

Quantin, C., Flahaut, J., Clenet, H., Allemand, P. and Thomas, P., 2012. Composition and structures of the subsurface in the vicinity of Valles Marineris as revealed by central uplifts of impact craters. Icarus, 221(1), pp.436-452.

Raack, J., Reiss, D., Appéré, T., Vincendon, M., Ruesch, O., Hiesinger, H., 2015. Present-Day Seasonal Gully Activity in a South Polar Pit (Sisyphi Cavi) on Mars. Icarus 251, 226–243. doi:j.icarus.2014.03.040

Reiss, D. and Jaumann, R., 2003. Recent debris flows on Mars: Seasonal observations of the Russell Crater dune field. Geophysical Research Letters, 30(6).

Rieder, R., Gellert, R., Anderson, R., Brückner, J., Clark, B., Dreibus, G., . . . Zipfel, J. (2004). Chemistry of Rocks and Soils at Meridiani Planum from the Alpha Particle X-ray Spectrometer. Science, 306(5702), 1746-1749. Retrieved from http://www.jstor.org/stable/3839770

Roach, L.H., Mustard, J.F., Murchie, S.L., Bibring, J.P., Forget, F., Lewis, K.W., Aharonson, O., Vincendon, M. and Bishop, J.L., 2009. Testing evidence of recent hydration state change in sulfates on Mars. Journal of Geophysical Research: Planets, 114(E2).

Roloff, V., et al. On-Ground Performance and Calibration of the ExoMars Trace Gas Orbiter CaSSIS Imager, submitted to SSR, November 2016

Schon, S.C., Head, J.W., 2012. Gasa impact crater, Mars: Very young gullies formed from impact into latitude-dependent mantle and debris-covered glacier deposits? Icarus 218, 459–477. doi:10.1016/j.icarus.2012.01.002

Schorghofer, N. and Edgett, K.S., 2006. Seasonal surface frost at low latitudes on Mars. Icarus, 180(2), pp.321-334.

Seelos, F. P., S. L. Murchie, D. C. Humm, O. S. Barnouin, F. Morgan, H. W. Taylor, C. Hash, and CRISM Team (2011a), CRISM Data Processing and Analysis Products Update — Calibration, Correction, and Visualization, in Lunar and Planetary Institute Science Conference Abstracts, vol. 42, p. 1438.

Seelos, F. P., S. L. Murchie, A. McGovern, M. P. Milazzo, and K. E. Herkenhoff (2011b), CRISM/HiRISE Correlative Spectroscopy, in AGU Fall Meeting Abstracts, vol. 23, p. 1714.

Seelos, F. P., M. F. Morgan, H. W. Taylor, S. L. Murchie, D. C. Humm, K. D. Seelos, O. S. Barnouin, C. E. Viviano, and CRISM Team (2012), CRISM Map Projected Targeted Reduced Data Records (MTRDRs) – High Level Analysis and Visualization Data Products, in Planetary Data: A Workshop for Users and Software Developers, vol. Open-File Report 2014–1056, pp. 159–162, USGS, Flagstaff, AZ.

Seelos, F. P., C. E. Viviano-Beck, M. F. Morgan, G. Romeo, J. J. Aiello, and S. L. Murchie (2016), CRISM Hyperspectral Targeted Observation PDS Product Sets — TERs and MTRDRs, vol. 47, p. 1783.

Seelos, K. D., F. P. Seelos, C. E. Viviano-Beck, S. L. Murchie, R. E. Arvidson, B. L. Ehlmann, and A. A. Fraeman (2014), Mineralogy of the MSL Curiosity landing site in Gale crater as observed by MRO/CRISM, Geophys. Res. Lett., 41, 4880–4887, doi:10.1002/2014GL060310.

Silvestro, S., Vaz, D.A., Fenton, L.K. and Geissler, P.E., 2011. Active aeolian processes on Mars: A regional study in Arabia and Meridiani Terrae. Geophysical Research Letters, 38(20).

Silvestro, S., Vaz, D.A., Ewing, R.C., Rossi, A.P., Fenton, L.K., Michaels, T.I., Flahaut, J. and Geissler, P.E., 2013. Pervasive aeolian activity along rover Curiosity's traverse in Gale Crater, Mars. Geology, 41(4), pp.483-486.

Skok, J.R., Mustard, J.F., Tornabene, L.L., Pan, C., Rogers, D. and Murchie, S.L., 2012. A spectroscopic analysis of Martian crater central peaks: Formation of the ancient crust. Journal of Geophysical Research: Planets, 117(E11).

Smith, D.E., Zuber, M.T. and Neumann, G.A., 2001. Seasonal variations of snow depth on Mars. Science, 294(5549), pp.2141-2146.

Sun, V.Z. and Milliken, R.E., 2014. The geology and mineralogy of Ritchey crater, Mars: Evidence for post-Noachian clay formation. Journal of Geophysical Research: Planets, 119(4), pp.810-836.

Sun, V.Z. and Milliken, R.E., 2015. Ancient and recent clay formation on Mars as revealed from a global survey of hydrous minerals in crater central peaks. Journal of Geophysical Research: Planets, 120(12), pp.2293-2332.

Thomas, N., et al. The Colour and Stereo Surface Imaging System (CaSSIS) for the ExoMars Trace Gas Orbiter, submitted to SSR, November 2016

Tornabene, L.L., Moersch, J.E., McSween, H.Y., Hamilton, V.E., Piatek, J.L. and Christensen, P.R., 2008. Surface and crater-exposed lithologic units of the Isidis Basin as mapped by coanalysis of THEMIS and TES derived data products. Journal of Geophysical Research: Planets, 113(E10).

Tornabene, L.L., Osinski, G.R., Barlow, N.G., Bray, V.J., Caudill, C.M., D'Aoust, B., Ding, N., Hopkins, R., Nuhn, A.M., Mayne, A. and McEwen, A.S., 2015. Meter-to Decameter-Scale Characteristics of Central Uplifts Revealed by the Mars Reconnaissance Orbiter. LPI Contributions, 1861, p.1043.

Tulyakov S, Ivanov A, Thomas N, Roloff V, Pommerol A, Cremonese G, Weigel T, Fleuret F Geometric calibration of Colour and Stereo Surface Imaging System of ESA's Trace Gas Orbiter. ArXiv e-prints, (2017). 1707.00606

Unsalan, Cem., and K. L. Boyer. (2004). A system to detect houses and residential street networks in multispectral satellite images. Proceedings of the 17th International Conference on Pattern Recognition (ICPR '04), Volume 3.

Vago, J., O. Witasse, H. Svedhem, P. Baglioni, A. Haldemann, G. Gianfiglio, T. Blancquaert, D. McCoy, and R. de Groot (2015), ESA ExoMars program: The next step in exploring Mars, Solar System Research, 49, 518-528.

Villanueva, G. L., Mumma, M. J., Novak, R. E., Radeva, Y. L., Käufl, H. U., Smette, A., ... & Hartogh, P. (2013). A sensitive search for organics (CH4, CH3OH, H2CO, C2H6, C2H2, C2H4), hydroperoxyl (HO2), nitrogen compounds (N2O, NH3, HCN) and chlorine species (HCl, CH3Cl) on Mars using ground-based high-resolution infrared spectroscopy. Icarus, 223(1), 11-27.

Vincendon, M., 2015. Identification of Mars gully activity types associated with ice composition. J. Geophys. Res. Planets 120, 1859–1879. doi:10.1002/2015JE004909Viviano, C.E., Moersch, J.E. and McSween, H.Y., 2013. Implications for early hydrothermal environments on Mars through the spectral evidence for carbonation and chloritization reactions in the Nili Fossae region. Journal of Geophysical Research: Planets, 118(9), pp.1858-1872.

Viviano-Beck, C.E., Seelos, F.P., Murchie, S.L., Kahn, E.G., Seelos, K.D., Taylor, H.W., Taylor, K., Ehlmann, B.L., Wiseman, S.M., Mustard, J.F. and Morgan, M.F., 2014. Revised CRISM spectral parameters and summary products based on the currently detected mineral diversity on Mars. Journal of Geophysical Research: Planets, 119(6), pp.1403-1431.

Webster, C. R., Mahaffy, P. R., Atreya, S. K., Flesch, G. J., Mischna, M. A., Meslin, P. Y., ... & Martín-Torres, J. (2015). Mars methane detection and variability at Gale crater. Science, 347(6220), 415-417.

2407 Williams Jr, R. S., & Ferrigno, J. G. (1988). Satellite image atlas of glaciers of the
2408 world (No. 1386). US Geological Survey.
2409 Wolff, M. J., Smith, M. D., Clancy, R. T., Arvidson, R., Kahre, M., Seelos, F., ... &
2410 Savijärvi, H. (2009). Wavelength dependence of dust aerosol single
2411 scattering albedo as observed by the Compact Reconnaissance Imaging
2412 Spectrometer. Journal of Geophysical Research: Planets, 114(E2).
2413 Wulf, G., Poelchau, M.H. and Kenkmann, T., 2012. Structural asymmetry in martian
2414 impact craters as an indicator for an impact trajectory. Icarus, 220(1),
2415 pp.194-204.
2416 Wray, J.J., Ehlmann, B.L., Squyres, S.W., Mustard, J.F. and Kirk, R.L., 2008.
2417 Compositional stratigraphy of clay-bearing layered deposits at Mawrth
2418 Vallis, Mars. Geophysical Research Letters, 35(12).
2419 Wray, J.J., Murchie, S.L., Bishop, J.L., Ehlmann, B.L., Milliken, R.E., Wilhelm, M.B.,
2420 Seelos, K.D. and Chojnacki, M., 2016. Orbital evidence for more
2421 widespread carbonate-bearing rocks on Mars. Journal of Geophysical
2422 Research: Planets, 121(4), pp.652-677.
2423 Wray, J.J. and Ehlmann, B.L., 2011. Geology of possible Martian methane source
2424 regions. Planetary and Space Science, 59(2), pp.196-202.
2425 Wyatt, M.B. and McSween, H.Y., 2002. Spectral evidence for weathered basalt as
2426 an alternative to andesite in the northern lowlands of Mars. Nature,
2427 417(6886), pp.263-266.
2428 Zurek, R.W. and Smrekar, S.E., 2007. An overview of the Mars Reconnaissance
2429 Orbiter (MRO) science mission. Journal of Geophysical Research: Planets,
2430 112(E5).
2431 Zurek, R. W., Chicarro, A., Allen, M. A., Bertaux, J. L., Clancy, R. T., Daerden, F., ...
2432 & Smith, M. D. (2011). Assessment of a 2016 mission concept: The search
2433 for trace gases in the atmosphere of Mars. Planetary and Space Science,
2434 59(2), 284-291.

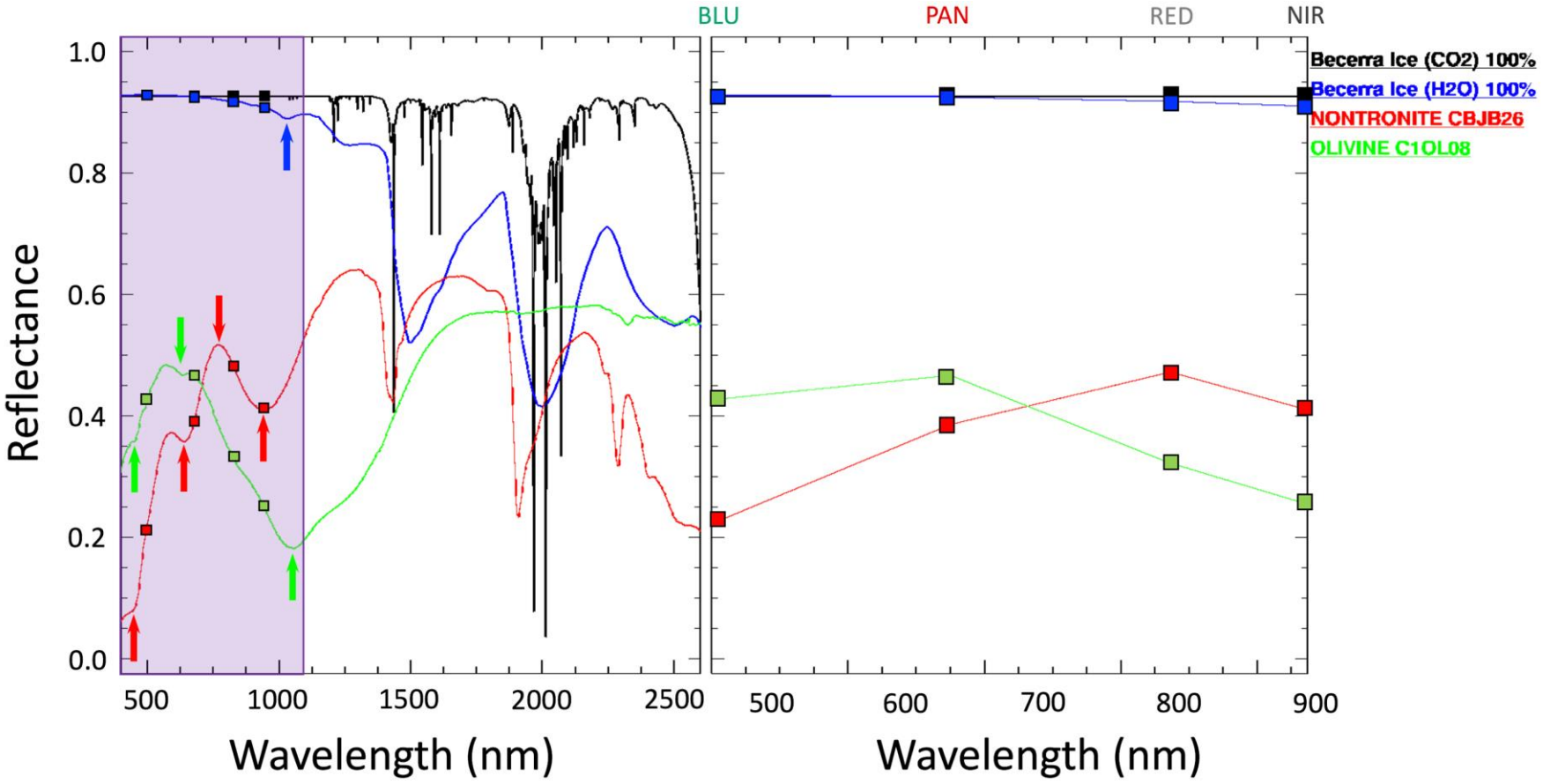

Figure 1 Selected ferric (Fe^{3+}) iron-bearing (nontronite – ID# CBJB26) and ferrous (Fe^{2+}) iron-rich (olivine - ID# C10L08) mineral spectra (300 bands) from the CRISM spectral library (**left**) and Hapke-modeled cos (i)-corrected I/F ice spectra (750 bands) for pure CO_2 and H_2O at an incidence of 68° (after Beccera et al 2015) compared to their 4-point CaSSIS convolved equivalents (**right**). Arrows show the general location of key diagnostic spectral features, which the CaSSIS bands (**squares**) would be sensitive to. The shaded region on the left denotes the instrument filter response range of CaSSIS (~400-1100 nm; *c.f.*, Figure 2 and see Thomas et al this issue).

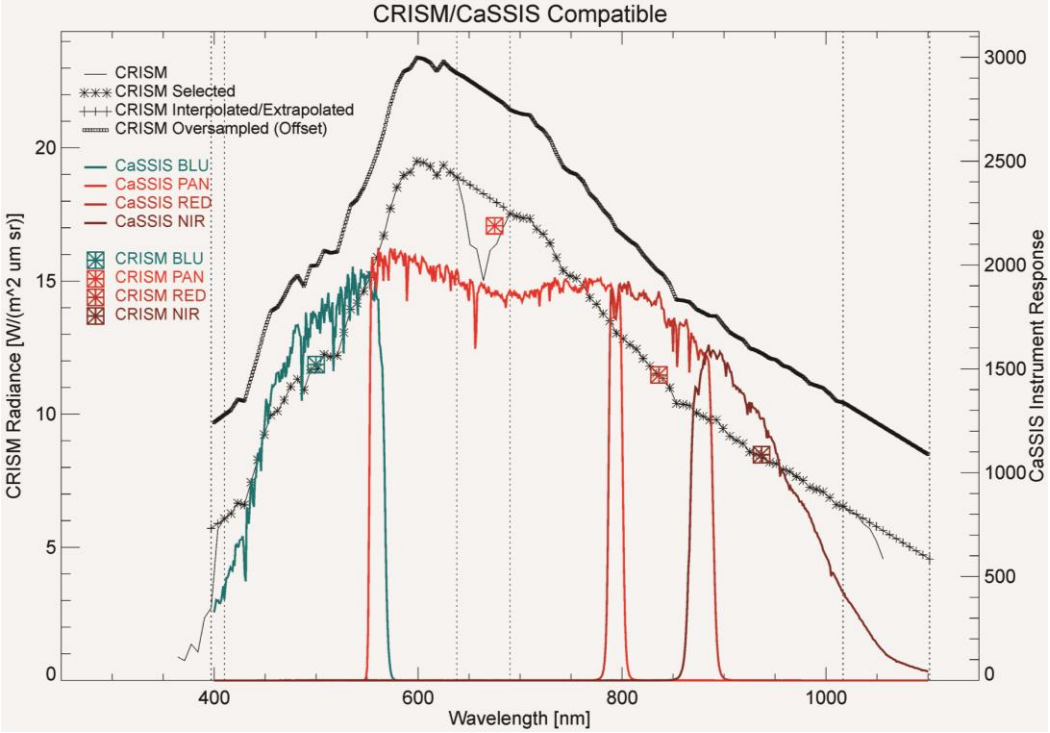

Figure 2 CRISM-CaSSIS compatible spectral processing. CRISM FRT00003E12 median radiance spectrum at native spectral sampling (**unadorned black line**), selected channels (**black asterisks**) with interpolated and extrapolated points (**black crosses**), and oversampled (**black squares - offset**), CaSSIS instrument response functions (**coloured lines – refer to alternate axis on right**), and CRISM/CaSSIS compatible radiance values (**large coloured symbols**). Vertical dotted lines indicate interpolation and extrapolation wavelength boundaries. Each CRISM VNIR I/F spectrum in the input image cube is transformed to spectral radiance, interpolated/extrapolated to cover the full spectral range of the CaSSIS response, oversampled to the CaSSIS response spectral sampling, integrated by the response functions, and the result transformed back to I/F.

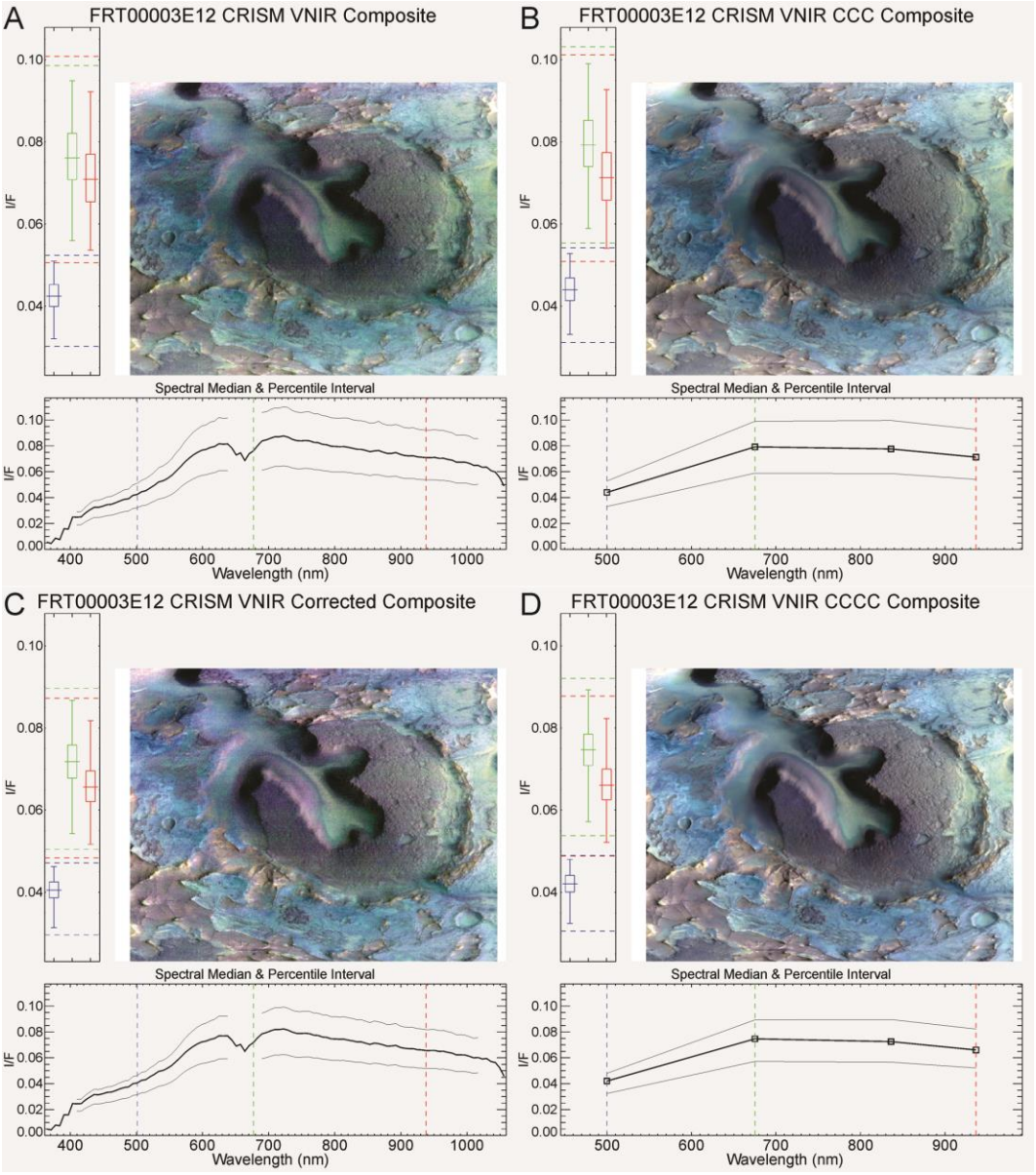

Figure 3 CRISM-CaSSIS Compatible (C^3) and Corrected CRISM-CaSSIS Compatible (C^4) processing progression presented as a series of 3-panel plots for CRISM observation FRT00003E12. Each 3-panel plot is composed of a sensor space (non-map projected) RGB composite (~10-12 km in width) with a 0.25% linear stretch on each band, a spectral plot with the median spectrum for the scene and a 1-99% spectral envelope, and box-plots illustrating the data distribution of the RGB composite bands. The vertical dashed lines on the spectral plot indicate the spectral bands that are mapped into the RGB composite channels, and the horizontal dashed lines on the box-plots indicate the stretch limits applied to each RGB composite band. (**A**) The RGB composite bands are individual CRISM channels that closely match the effective wavelengths of the CaSSIS bandpass (see Table 1). Note that effective wavelength of the CaSSIS PAN band (~675 nm) is in the spectral region affected by the CRISM VNIR filter boundary. (**B**) Visualization of the corresponding CRISM-CaSSIS Compatible (C^3) data product. The spectrum for each spatial pixel in (**A**) has been processed to CaSSIS 4-band colour as described in the text. (**C**) CRISM observation FRT00003E12 after application of the Empirical Geometric Normalization. (**D**) Corrected CRISM-CaSSIS Compatible (C^4) data product (simulated CaSSIS colours at 18-20m/pixel). The spectrum for each spatial pixel in (**C**) has been processed to CaSSIS 4-band colour as described in the text.

Figure4 and caption

Click here to download figure
Tornabene_et_al_2016_CaSSIS_sim_SSR_FIGURE4_revised.docx

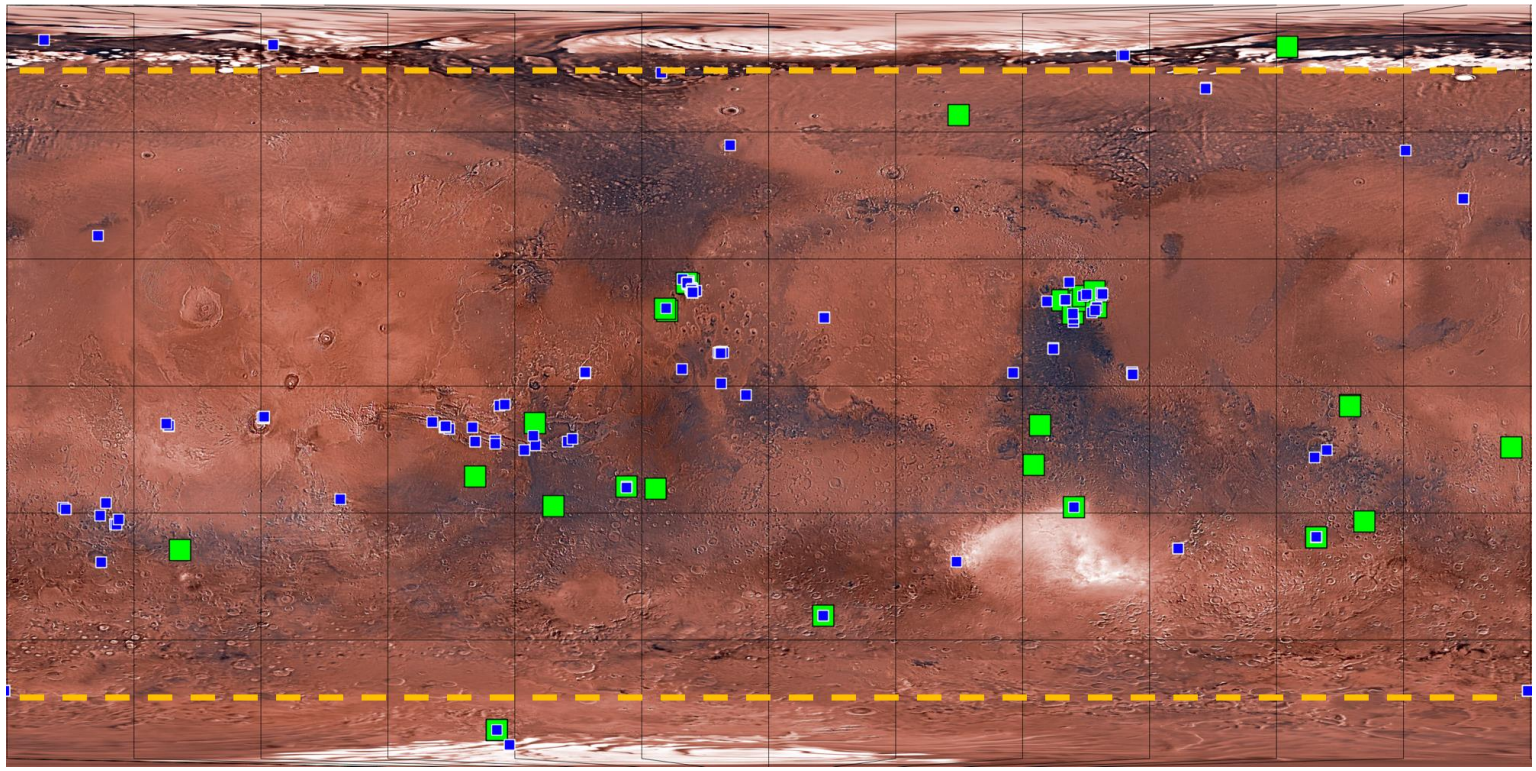

Figure 4 Map of target locations of 180 simulated CaSSIS images on Mars. Green squares denote the locations of the 33 "fully"-simulated CaSSIS image cubes, which includes 30 unique locations; while the smaller blue squares indicate the locations of the CRISM-CaSSIS compatible colour only products *(i.e.*, the C^3 and C^4 CRISM-derived cubes), which retain the spatial resolution of the CRISM cube from which they were derived (~18-36 m/pixel). This includes several of the CRISM mineral/phase localities reported in Viviano-Beck et al (2014). The location map uses the Viking colour MDIM 2.1. mosaic to show that the simulations are selected from diverse surfaces ranging in brightness and ferric/ferrous content. The map also shows that our simulated CaSSIS images cover diverse surfaces across a wide latitudinal and longitudinal range. The dashed-line denotes the 74th parallel in both hemispheres marking the approximate boundary of CaSSIS observations based on its orbital inclination. See Table S1 and the associated help file included with our supporting online supplementary materials for more information on the 181 simulated locations (180 surface locations plus one of Phobos). **Background image credits: JPL/NASA and USGS/NASA-AMES.**

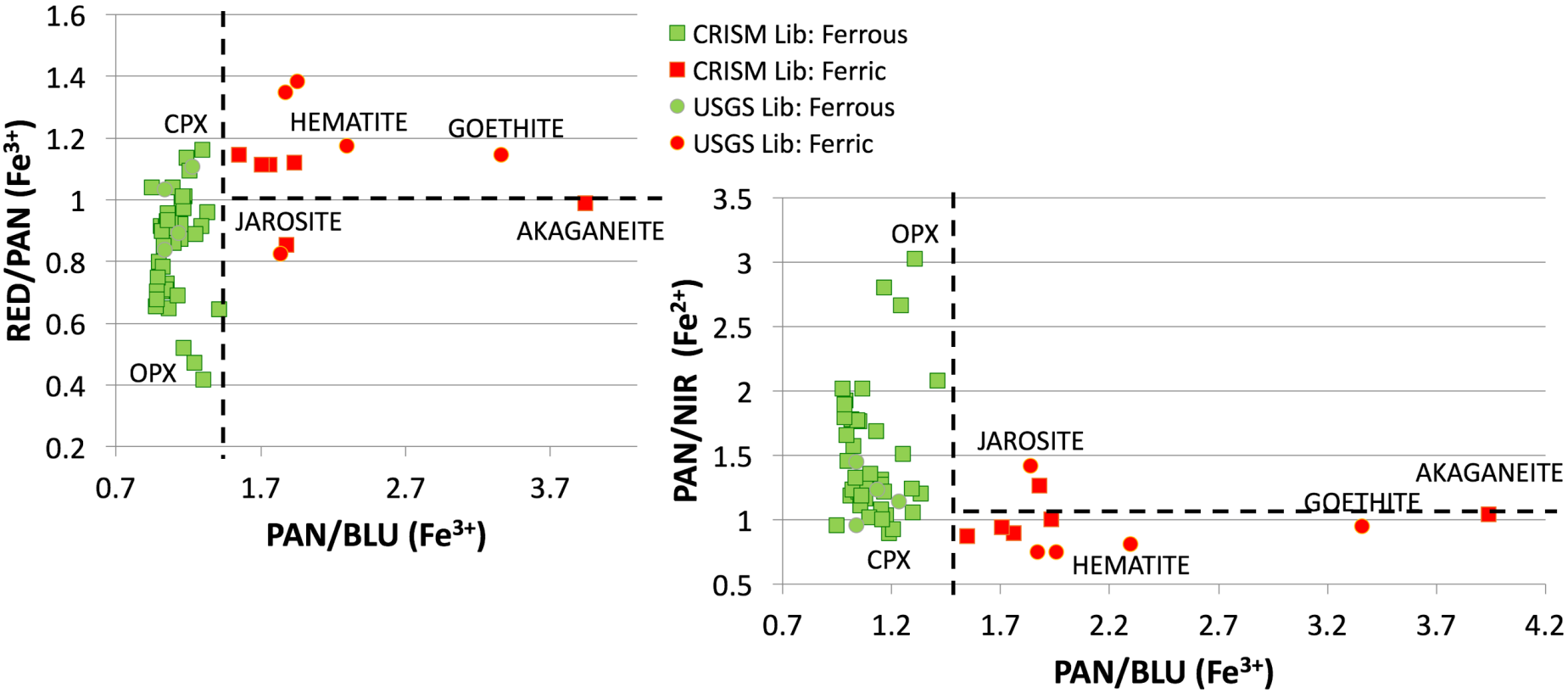

Figure 5 Band ratio bivariate plots of CaSSIS instrument response-convolved laboratory spectra of selected ferrous (Fe^{2+}) iron (green) and ferric (Fe^{3+}) iron (red) bearing minerals from the USGS and CRISM team spectral mineral libraries (Clark et al 1993; http://speclib.rsl.wustl.edu/). The plot indicates that 2PAN/1BLU ratios fully discriminate ferrous from ferric minerals, with all ferric minerals generally having 2PAN/1BLU values of < 1.41 (most < 1.3); and all ferric with 2PAN/1BLU values > 1.55 (most > 1.7). The 2PAN/4NIR does a reasonable job of discriminating ferrous from ferric minerals (**right**), with most ferrous materials having values generally > 1 and most ferric materials with values < 1. The 3RED/2PAN provides additional discrimination of ferric minerals (**left**). Dashed lines demark the general ferrous vs. ferric domains (See text and Table 3 for additional information on these ratios).

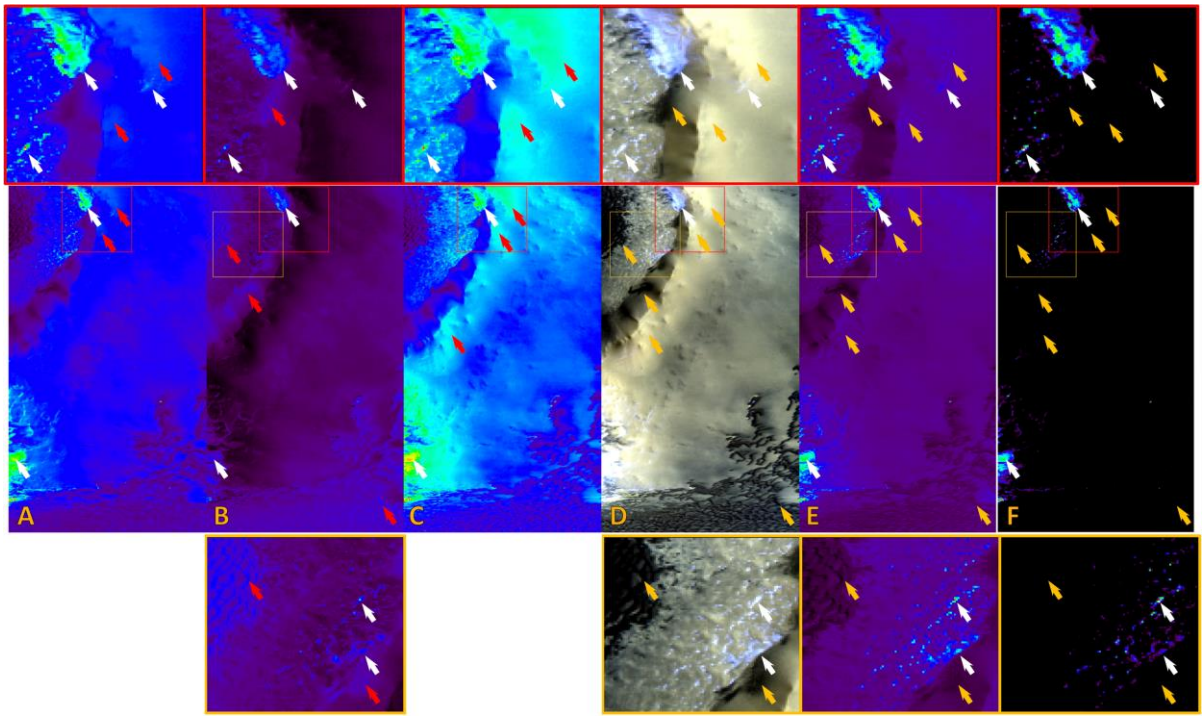

Figure 6 A comparison of a set of simulated CaSSIS products (**A**-**E**) to a CRISM IR 1500nm band-depth spectral parameter image (*i.e.*, BD1500) for H_2O ice (**F**). The CRISM cube used here is derived from S-detector data and the targeted observation HRL00002885, which covers the Viviano-Beck et al (2014) CRISM mineral/phase locality for H_2O ice. White arrows are locations of positive H_2O ice detections, while red arrows are negative detections (based on [**F**]). Comparing these two sets of arrows in (**A**-**C**) highlights the ambiguities between ice and non-ice-bearing surfaces in the first 3 panels. Orange arrows (in **D**-**F**) are used to indicate where false-detections occurred in (**A**-**C**), but are not ambiguous in images (**D**-**F**). Red and orange boxes in panels (**A**-**F**) correspond to the colour-coded rows of 3x zoomed subimages at the top and bottom. **A**) This colourized simulated CaSSIS BLU band image shows strongly illuminated (red arrows) areas that are ambiguous with ices. **B**) This colourized simulated CaSSIS NIR/BLU ratio image shows basaltic dunes (red arrows) that are ambiguous with ices. **C**) This colourized simulated CaSSIS mean multiband reflectance or I/F intensity image also shows illuminated areas (red arrows) that are ambiguous with ices. **D**) Shows a simulated CaSSIS infrared colour image (IRB1) for context. **E**) This colourized simulated CaSSIS image produced by dividing panels (**C**) by (**B**) and most effectively highlights surface ice and frost (*c.f.*, with (**F**)). (**A**-**C**, **E**) all have linear min-max stretches and an ENVI pre-defined BLUE-RED colour table applied, while (**D**) has a linear 0.5% stretch applied to each band, and (**F**) has a linear stretch from a value of 0 to its maximum value of 0.25. **Image credits: WesternU-CPSX/ASC-CSA/NASA, NASA/JPL/JHU-APL and ESA/Roscosmos/ExoMars/CaSSIS.**

Figure7 and caption

Click here to download figure
Tornabene_et_al_2016_CaSSIS_sim_SSR_FIGURE7_revised.docx

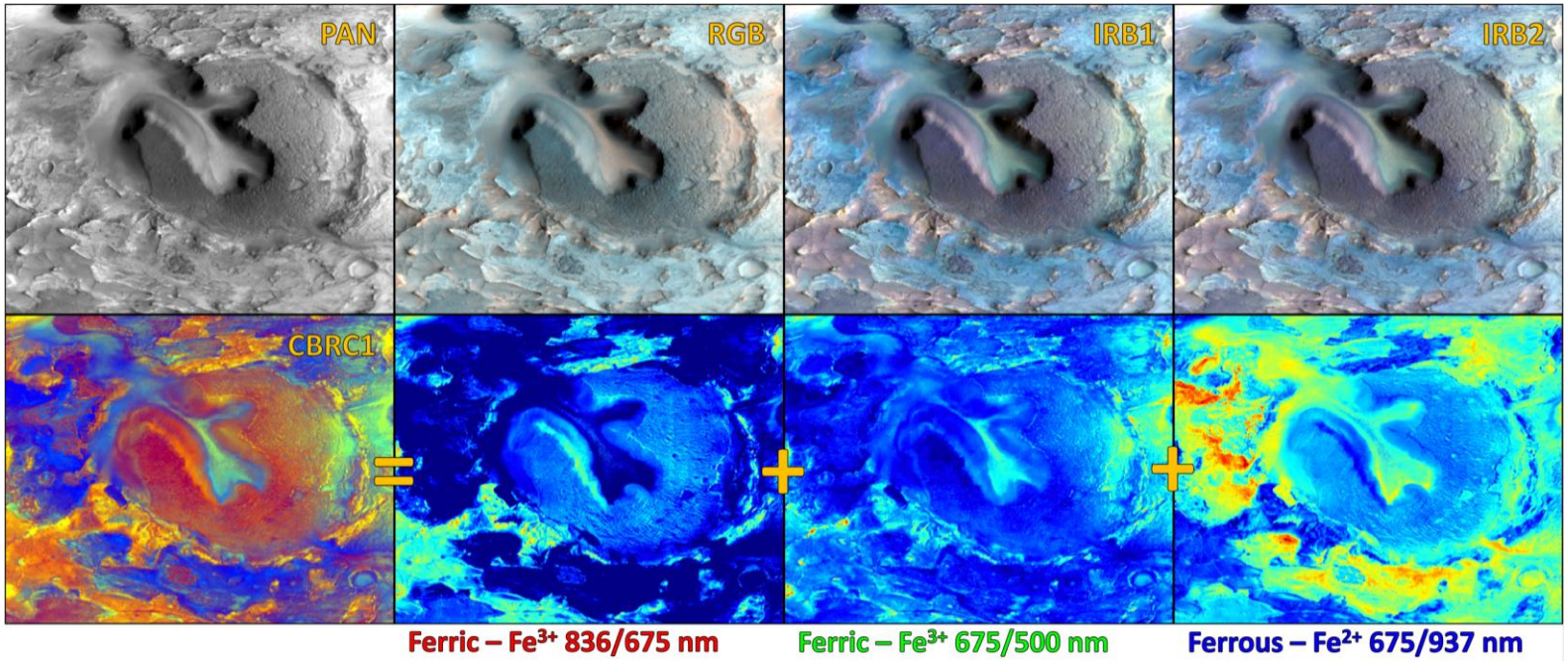

Figure 7 A set of suggested CaSSIS image modes/colour-products based on a non-map-projected (~10-12 km in width) C^4 cube produced from S-detector data from the targeted observation FRT00003E12, centred at 77.1°E, E, 22.24°N, in the Nili Fossae region. **PAN** = Greyscale red image using the 2PAN Band; **RGB** = Synthetic "true" colour (bands 2-1-0); **IRB1** = Infrared colour image using the last NIR band – 4NIR (Bands 4-2-1); **IRB2** = Infrared colour image using the first NIR band – 3RED (Bands 3-2-1); (**bottom**) **CBRC1** = band ratios using 3RED/2PAN, 2PAN/1BLU, 2PAN/4NIR in R-G-B. The last 3 images in the bottom row are the individual band ratios of which CBRC1 at the beginning of the row is comprised (in R-G-B order). Each of these greyscale images have a colour table applied to them to show areas with low and high values (*i.e.*, variations of relative band-strength as a proxy for exposure or concentration of Fe-bearing species). The top row, and the CBRC1, images all have a linear 0.5% stretch on each band, while the last three images in the bottom row all have linear min-max stretches to the upper part of their histograms and an ENVI pre-defined BLUE-RED colour table applied. **Image credits: WesternU-CPSX/ASC-CSA/NASA, NASA/JPL/JHU-APL and ESA/Roscosmos/ExoMars/CaSSIS.**

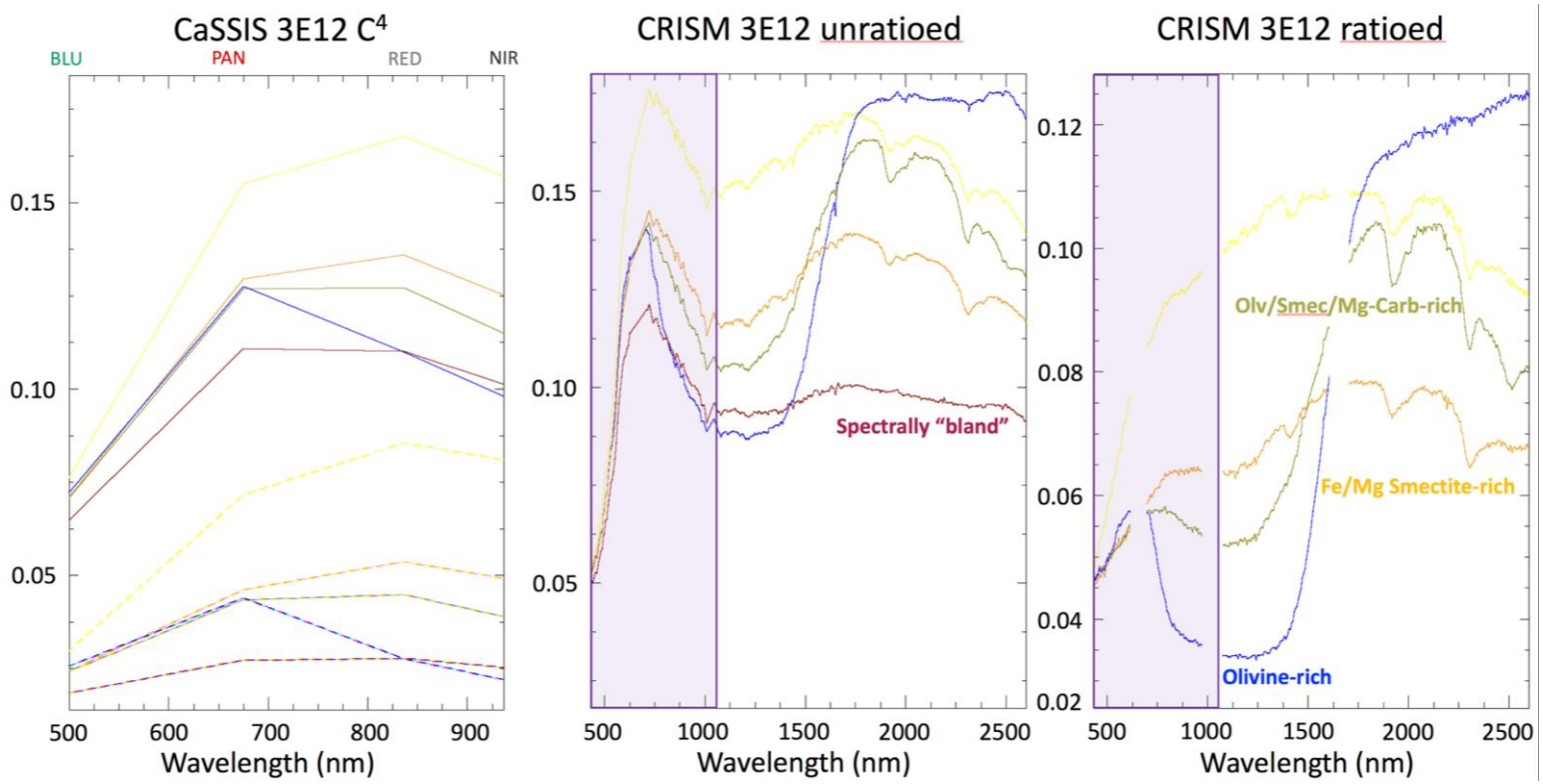

Figure 8 Simulated CaSSIS C^4 image-derived averaged spectra (3x3 pixel) compared to CRISM spectra derived from a "joined" CRISM MTRDR cube. Locations of the averaged spectra were based on spectral/colour units defined off our CBRC1 composite presented in Figure 7, and the known location for Mg-carbonate bearing deposits, reported by Ehlmann et al (2008) and Viviano-Beck et al (2014), in the scene. The sensitivity range of the 4 colour bands of CaSSIS is represented by the shaded regions shown in the two plots on the right. The set of coloured 4-point simulated CaSSIS spectra (**left**) are extracted from a C^4 cube created from CRISM targeted observation FRT00003E12, with the lower I/F coloured set of spectra (**dashed lines**) originating from an *ad hoc* atmospheric/haze-corrected cube using a dark subtraction method. These simulated CaSSIS spectra are compared to unratioed (**centred**) and ratioed (**right**) spectra extracted from the joined CRISM MTRDR cube. The olivine- and smectite-rich spectra (**right**) are consistent with the results of previous studies (*e.g.*, Mustard et al 2009), but can also be compared to lab spectra presented in Figure 1.

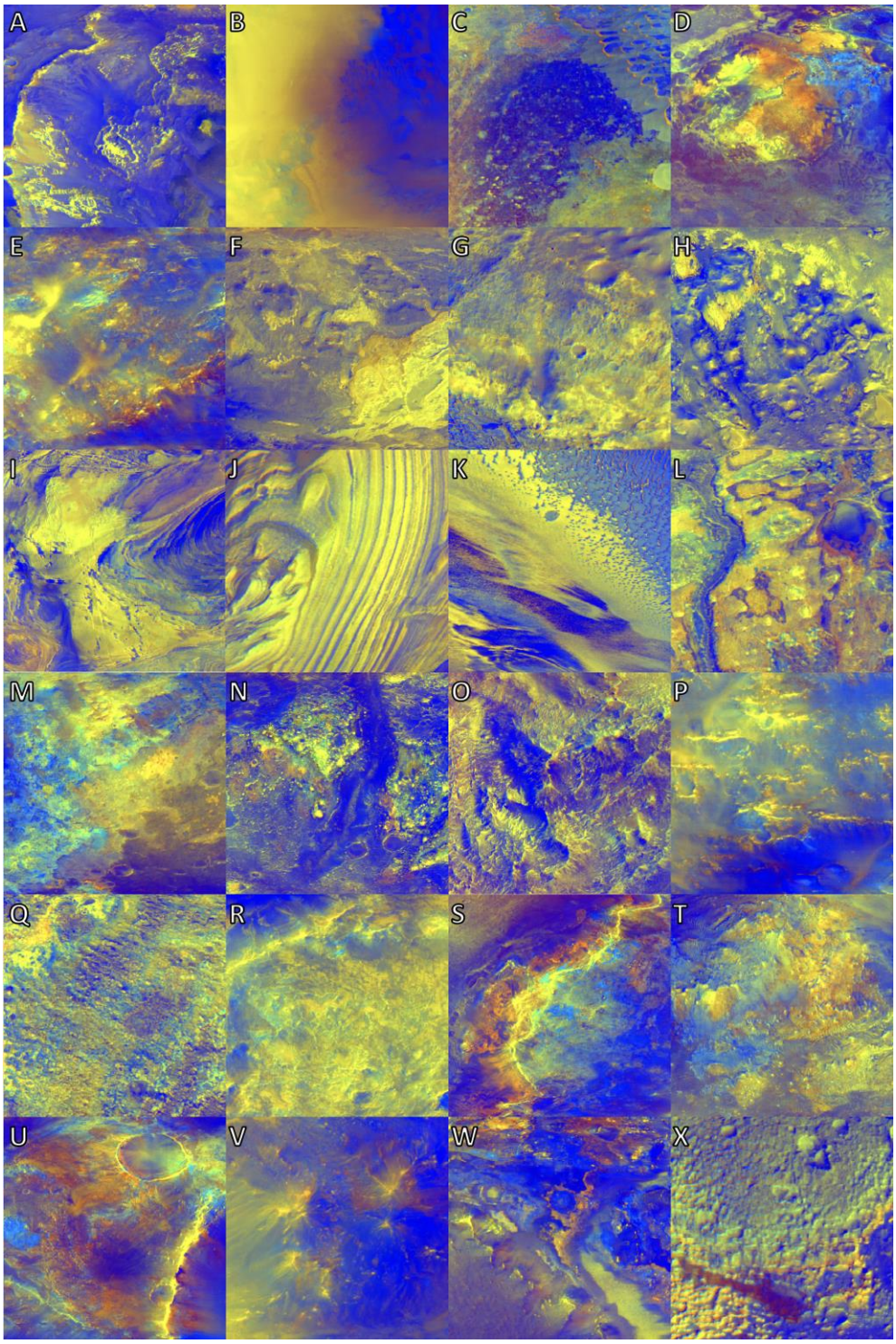

Figure 9 Cropped examples of simulated CaSSIS CBRC1s produced from non-map projected C^4 cubes based off the CRISM targeted observations covering 24 of the Viviano-Beck et al (2014) CRISM mineral/spectral-type localities on Mars. Starting from the top and moving to the right, these include the type localties for: (**A**) Hematite (B385), (**B**) Mg-Olivine (C26C), (**C**) Plagioclase (82EE), (**D**) Low-Ca Pyroxene (64D9), (**E**) High-Ca Pyroxene (8F68), (**F**) Monohydrated sulfate (A91C), (**G**) Alunite (B252), (**H**) Hydroxlated Fe-sulfate (98B2), (**I**) Jarosite (13F5B), (**J**) Polyhydrated sulfate (9C0A), (**K**) Gypsum (CA5C), (**L**) Bassanite (9326), (**M**) Kaolinite (ABCB), (**N**) Al-smectite (3BFB), (**O**) Margarite & Serpentine (634B), (**P**) Illite/Muscovite(454E), (**Q**) Fe-smectite (A425), (**R**) Mg-smectite (9365), (**S**) Talc (9D44) (**T**) Chlorite & Ca/Fe-Carbonate (A546), (**U**) Prehnite (50F2), (**V**) Hydrated silica & Analcime (9312), (**W**) Epidote (CBE5), and (**X**) Chloride (AB81). Fe-Olivine & Mg-Carbonate (3E12) CBRC1 is shown in Figure 7. **Image credits: WesternU-CPSX/ASC-CSA/NASA, NASA/JPL/JHU-APL and ESA/Roscosmos/ExoMars/CaSSIS.**

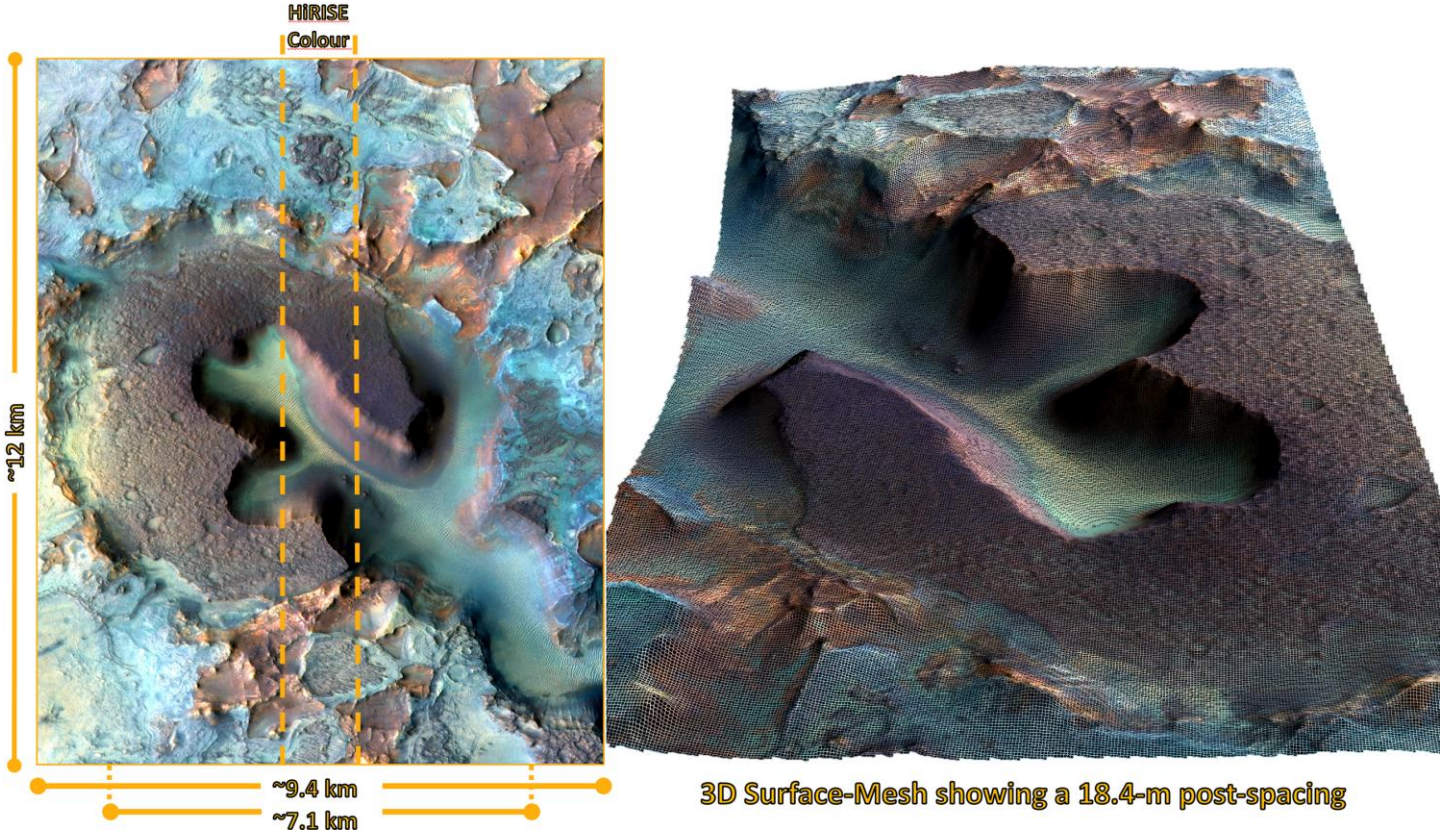

Figure 10 A fully-simulated CaSSIS infrared colour image (IRB1) at 4.6 m/pixel covering olivine-, serpentine-, smectite- and carbonate-bearing terrain in the Nili Fossae region (77.1°E, E, 22.24°N). (**Left**) The fully-simulated CaSSIS IRB1 image was cropped and annotated to show the two swath width modes currently being planned for CaSSIS, and compared with the maximum colour coverage provided by HiRISE (**dashed-lines**). The length of cropped image is ~12 km; however, CaSSIS will be able to achieve ~4x this length. (**Right**) A 3D perspective view (looking southward) made from overlaying the fully-simulated CaSSIS IRB1 image on a HiRISE DTM resampled to the anticipated CaSSIS DTM resolution (18.4 m/post) and set to a vertical exaggeration of 2x. **Image credits: WesternU-CPSX/ASC-CSA/NASA, NASA/JPL/JHU-APL/MSSS/UofA and ESA/Roscosmos/ExoMars/CaSSIS.**

Figure11 and caption

Click here to download figure
Tornabene_et_al_2016_CaSSIS_sim_SSR_FIGURE11_revised.docx

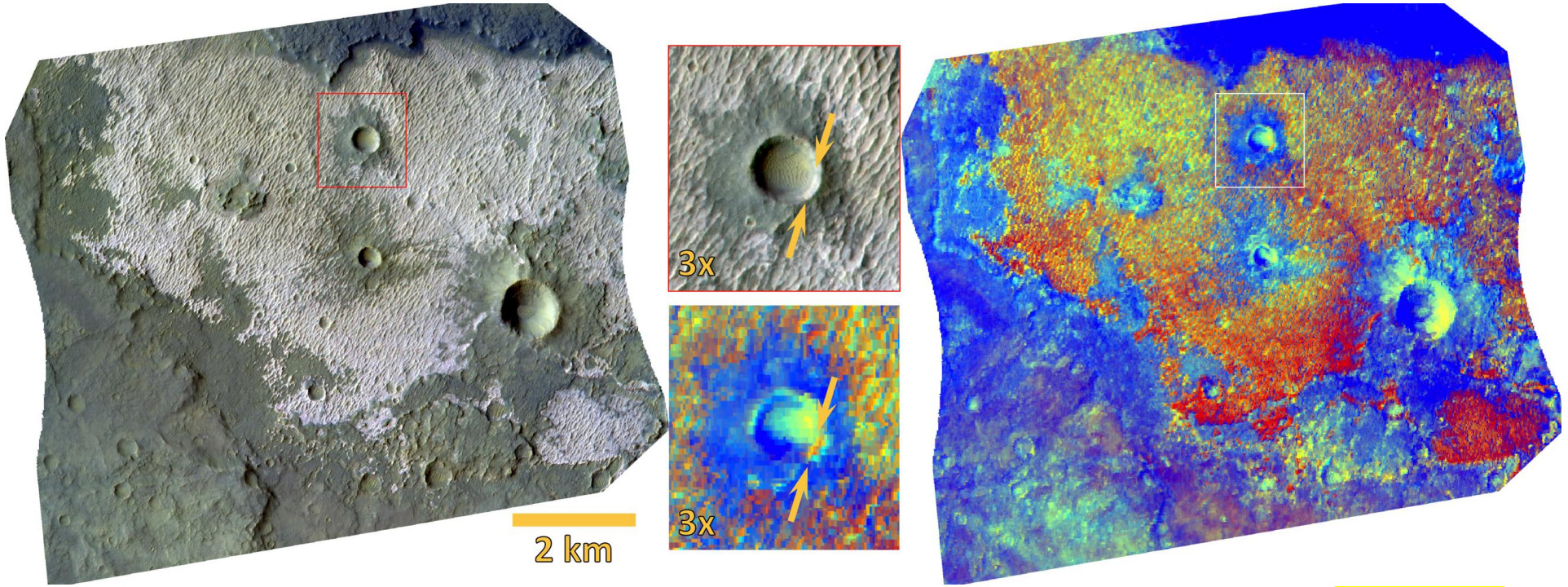

Figure 11 Fully-simulated CaSSIS colour images of a chloride-bearing site (221.04°E, 39.05°S) documented in the Martian chloride discovery paper (see Osterloo et al 2008). Colour infrared – IRB1 (**left**), and CBRC1 (**right**). The zoomed images (**centre**) highlight a ~500-m crater. The colour characteristics of its ejecta, and an exposure in the crater wall, (**arrows**) suggest that the chloride-bearing deposits are consistent with representing a salt pan or flat (*i.e.*, a superficial surface layer/crust of salts) underlain by ancient lava flows. In the upper right of the image is a more recent lava flow emanating from Daedalia Planum, which possesses a strong Ferrous iron-bearing signature consistent with relatively unaltered mafic-bearing materials. The image is ~9.3 km across at its narrowest. **Image credits: WesternU-CPSX/ASC-CSA/NASA, NASA/JPL/JHU-APL/MSSS/UofA and ESA/Roscosmos/ExoMars/CaSSIS.**

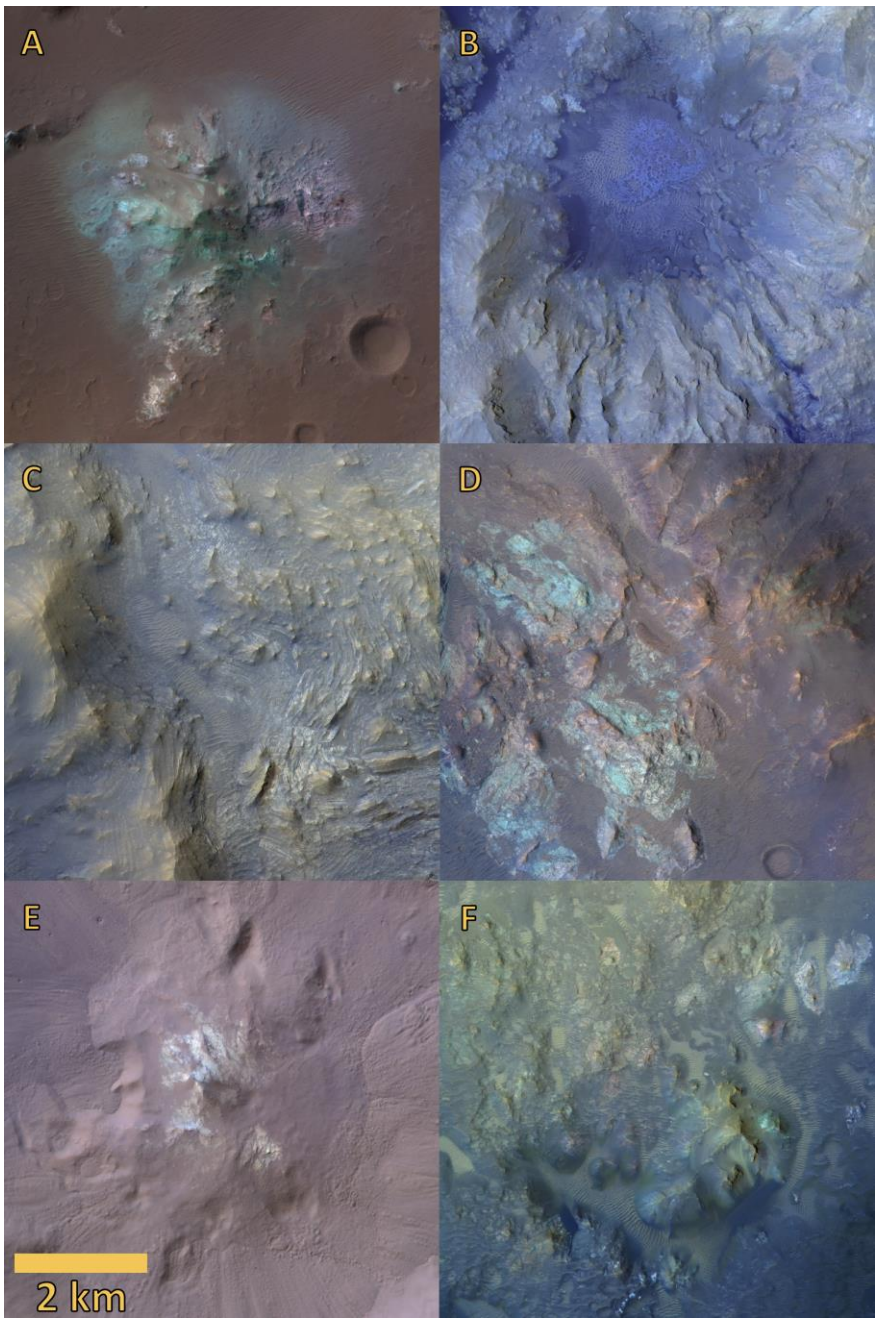

Figure 12 Fully-simulated CaSSIS infrared colour images (IRB1) of various crater central uplifts exposing the bedrock textural types defined and described by Tornabene et al (2015 and references therein): Layered (LB), Fractured and Massive (FMB) and "Mega"-brecciated (MBB). (**A**) Central peak of Alga crater (333.35°E, 24.34°S) exposing FMB with various coatings of impact melt-rich breccia deposits with diverse clast compositions (see Skok et al 2012 and D'Aoust 2015), (**B**) Peak pit of Elorza crater (304.79°E, 8.75°S) exposing hydrated silica, LCP, and smectite-bearing FMB coated by clast-poor impact melt-bearing deposits (see Hopkins et al 2016), (**C**) Eastern portion of the of the Martin crater central uplift (290.65°E, 21.42°S) exposing LB (see Caudill et al 2012 and Wulf et al 2012), (**D**) and (**E**) Central peaks of unnamed craters (72.14°E, 28.64°S and 72.14°E, 28.64°S) with well-exposed FMB. (**F**) Central peak complex of Verlaine crater (64.14°E, 9.25°S) exhibiting partial exposures of both FMB and MMB including coatings and flows of diverse impact melt-bearing deposits. (see D'Aoust 2015). Note: the scale bar is on the order of ~2x the width of the HiRISE colour swath. **Image credits: WesternU-CPSX/ASC-CSA/NASA, NASA/JPL/JHU-APL/MSSS/UofA and ESA/Roscosmos/ExoMars/CaSSIS**

Figure13 and caption

Click here to download figure
Tornabene_et_al_2016_CaSSIS_sim_SSR_FIGURE13_revised.docx

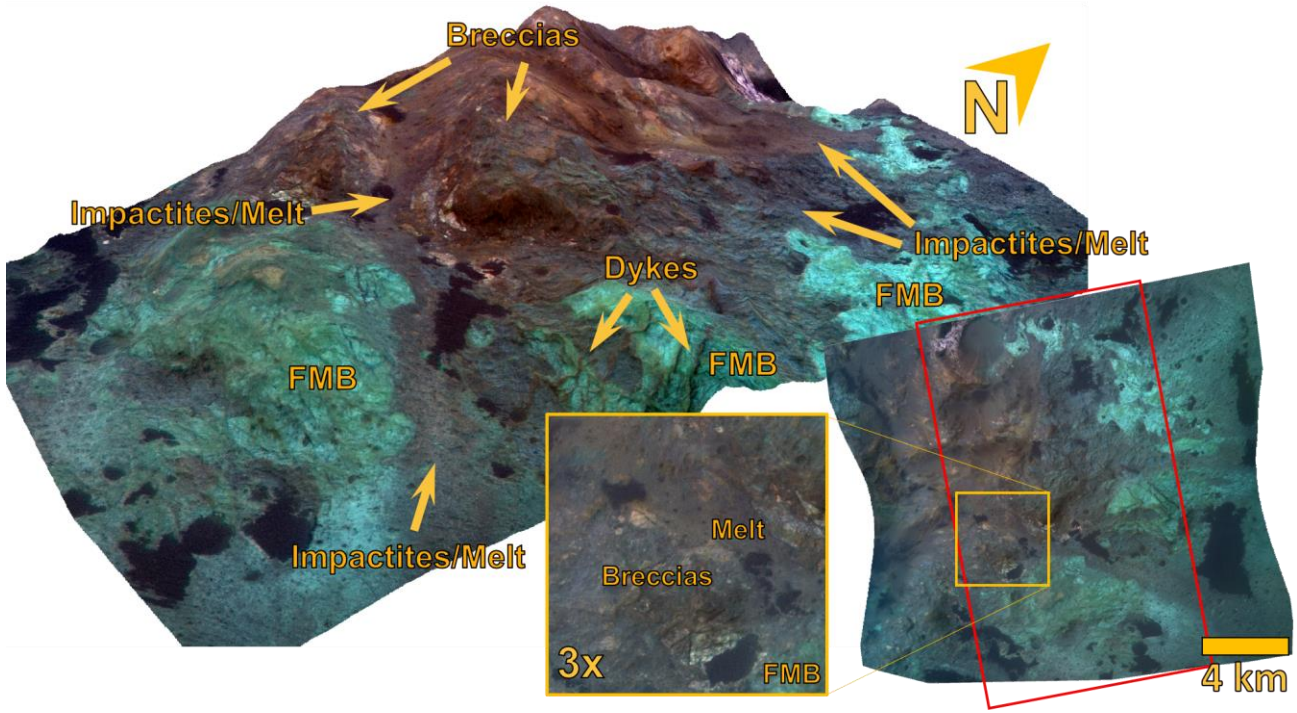

Figure 13 A 3D perspective of fully-simulated CaSSIS infrared colour image (IRB1) covering the eastern portion of the central peak of Ritchey crater (309.15°E, -28.45°N). The red box covers an area in 2D that corresponds to the approximate area covered by the 3D perspective image. Fractured-Massive Bedrock (FMB) is particularly well-exposed in the lower slopes of the uplift (cyan), while the upper slopes appear to be comprised of a "mega"brecciated core exhibiting mostly white or light yellow clasts that are predominately draped by relatively thin dark-toned deposits of melts and breccias. A spectacular continuous flow deposit of impact melt-bearing materials is observed starting at the summit near the annotation "Breccias" and continues down slope beyond the annotation "Impactites/Melt" and conforms with the local topography over its entire extent. Dark-toned lineaments are interpreted to be dykes, which can be seen cross-cutting a well-exposed block of FMB in the eastern flank of the uplift. Based on full-CRISM spectral characteristics, the cyan-coloured bedrock is consistent with LCP-bearing bedrock, limited exposures or clasts of olivine-bearing rocks are white or light yellow, and altered bedrock is magenta in colour. For more details on the Ritchey crater uplift, see Sun and Miliken (2014) and Ding et al (2015). **Image credits: WesternU-CPSX/ASC-CSA/NASA, NASA/JPL/JHU-APL/MSSS/UofA and ESA/Roscosmos/ExoMars/CaSSIS**

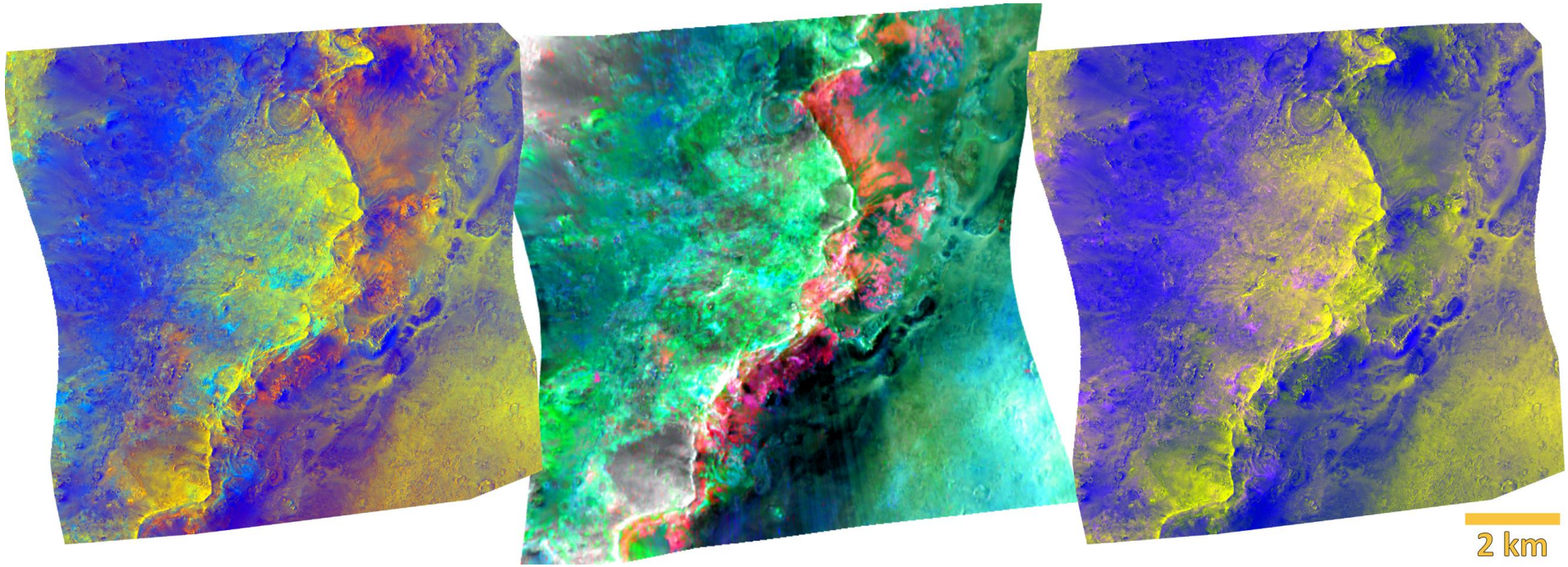

Figure 14 Fully-simulated CaSSIS colour images of the talc CRISM spectral mineral/phase type-locality (Viviano-Beck et al 2013, 2014) centred at 73.68°E, 20.06°N in the Nili Fossae region. Here we compare a simulated CaSSIS CBRC1 image that utilizes all 4 bands (**left**) with a HiRISE-equivalent CBRC image (**right**) that uses only three bands (see Delamere et al 2010). A simulated CaSSIS 4 band-derived CBRC1, which shows a greater variety of colours, to a 3 band-derived HiRISE CBRC. The colours of the simulated CaSSIS CBRC1 correlate better with the CRISM spectral parameter composite image (**centre**), which was constructed by combining the standard CRISM-derived "phyllosilicate" (PHY1) and "mafic" (MAF1) spectral parameter images, and then overlain on a CRISM IR brightness image (IRA; ~1330 nm). Viviano-Beck et al (2013) have shown CRISM spectral characteristics consistent with a talc-bearing unit that overlies a chlorite-bearing unit within the scarp-face exposed in this scene. These two notable mineral-bearing units are reddish-orange and yellow, respectively, in the simulated CaSSIS CBRC1 (**left**); these two units only show up as a single coloured unit (yellowish) in the HiRISE CBRC (**right**). **Image credits: WesternU-CPSX/ASC-CSA/NASA, NASA/JPL/JHU-APL/MSSS/UofA and ESA/Roscosmos/ExoMars/CaSSIS.**

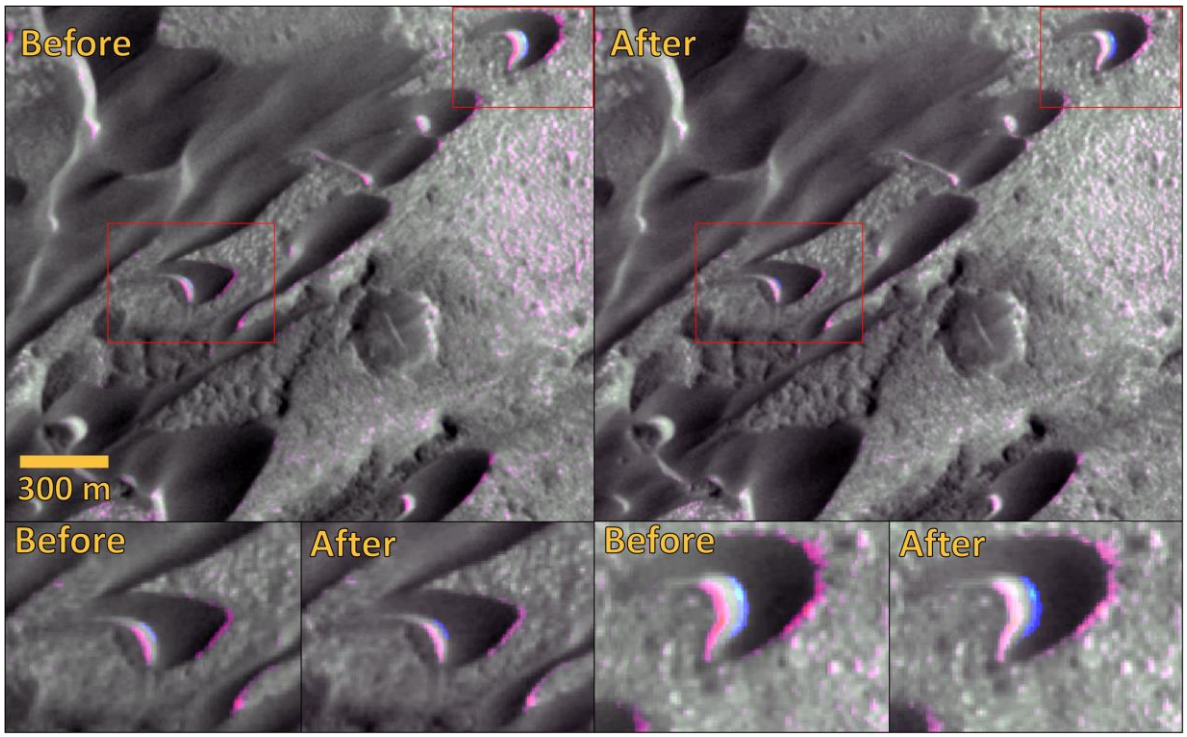

Figure 15 Nili Patera dune field (centered at 67.3°E, 8.8°N) movement recorded by two orthorectified CTX images taken 7.5 years apart and oversampled to the CaSSIS pixel-scale (4.6m/pix). The colour overlay here was created by taking the normalized difference between the two images P04_002427_1888_XI_08N292W (2/1/2007) and F05_037792_1891_XN_09N292W (8/19/2014), and highlights pixels with drastic changes in their intensity values (*i.e.*, at the lower and upper areas of the image histogram). Magenta highlights pixels that move from the lowest parts of the histogram in the "before" image to the highest parts (darker to lighter) in the "after" image, and blue highlights pixels that move from the highest parts of the histogram to the lowest parts (lighter to darker). Highlighted-changes are a consequence of dune migration, which is readily observed in animated GIFs provided as online supplemental materials. This new technique for highlighting changes between images in this fashion is described in more detail in the supporting online supplementary materials included with this manuscript. **Image credits: WesternU-CPSX/ASC-CSA/NASA, NASA/JPL/MSSS/UofA and ESA/Roscosmos/ExoMars/CaSSIS.**

figure16 and caption

Click here to download figure
Tornabene_et_al_2016_CaSSIS_sim_SSR_FIGURE16_revised.docx

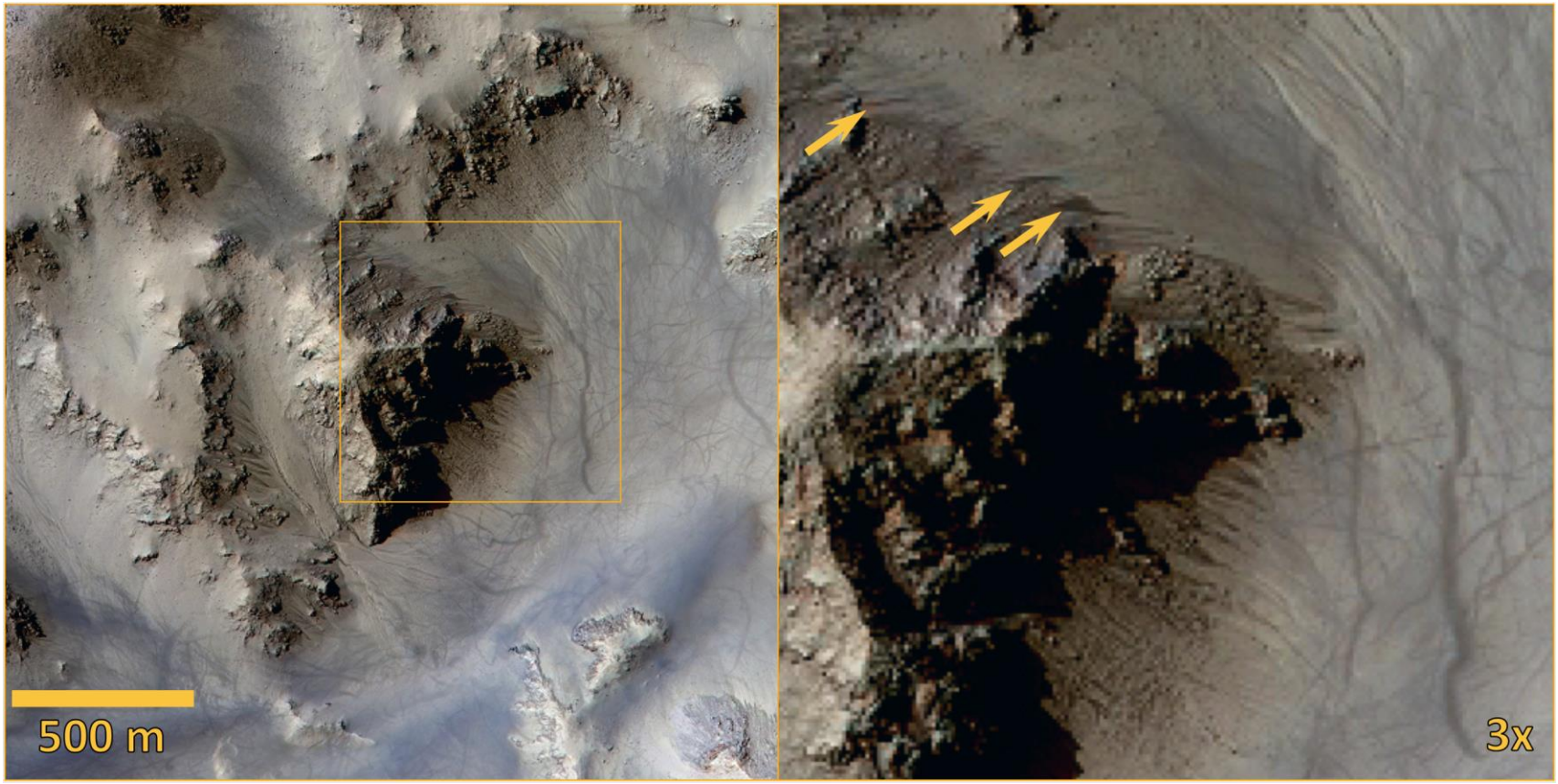

Figure 16 A fully-simulated CaSSIS infrared colour image (IRB1) of a portion of the central uplift of Horowitz crater (140.82°E, -32.05°N) known to host confirmed Recurring Slope Lineae (RSL). Three dark slope streaks (orange arrows) are HiRISE-confirmed RSLs observed in 2007 during southern summer (L_s = 334°) (*c.f.*, Figure 1 in McEwen et al 2011). Several other RSLs are resolved by the fully-simulated CaSSIS image, but only where they occur as dense groupings of RSLs. This simulated image also shows some gully channels (**upper right**) and relatively dark dust devil streaks (**right**) in the area. **Image credits: WesternU-CPSX/ASC-CSA/NASA, NASA/JPL/JHU-APL/MSSS/UofA and ESA/Roscosmos/ExoMars/CaSSIS.**

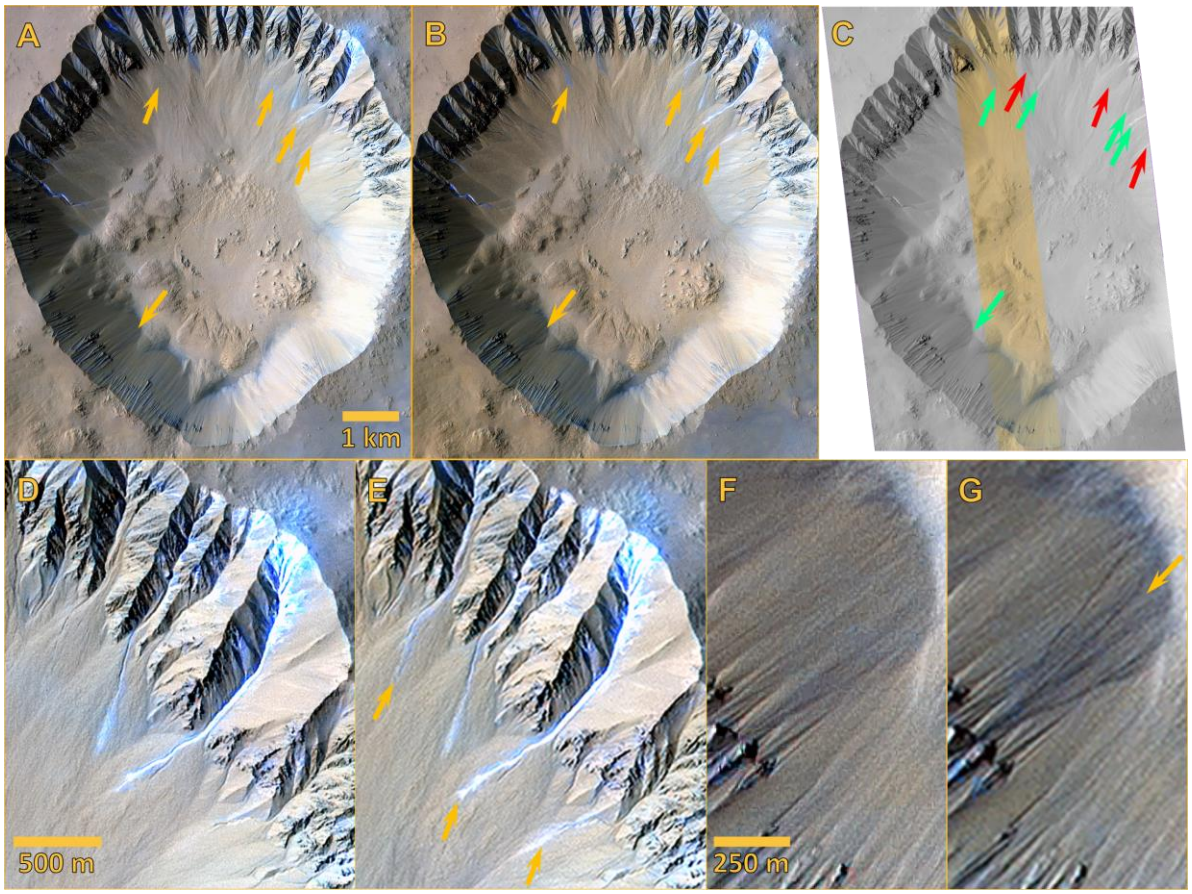

Figure 17 A comparison of two fully-simulated CaSSIS infrared colour (IRB1) images (**A** and **B**), and a cropped HiRISE MIRB image ESP_022718_1440 (**C**) of Gasa crater (129.39°E, -35.74°N). These images document changes that occurred between 2009 (**A**) and 2011 (**B–C**) and the anticipated ability of CaSSIS to detect these changes with its colour capability combined with its spatial coverage and resolution. Orange arrows show all locations where changes were observed in the simulated CaSSIS images. The green arrows in (**C**) indicate new or pre-existing light-toned gully deposits detected in both the HiRISE and simulated CaSSIS images. Red arrows indicate areas where a new or pre-existing light-toned gully deposit detected in the simulated CaSSIS images was difficult to detect in HiRISE, or was not covered with the narrow HiRISE colour strip. Changes from 2009–2011 in Gasa include both new gully deposits on the pole-facing slopes and a new mass wasting feature on the non-gullied southwestern crater wall. Please see the animated GIF of Gasa, based on the fully-simulated image pair in (**A)** and (**B**), provided with our supporting online supplementary materials. **Image credits: WesternU-CPSX/ASC-CSA/NASA, NASA/JPL/JHU-APL/MSSS/UofA and ESA/Roscosmos/ExoMars/CaSSIS.**

figure18 and caption

Click here to download figure
Tornabene_et_al_2016_CaSSIS_sim_SSR_FIGURE18_revised.docx

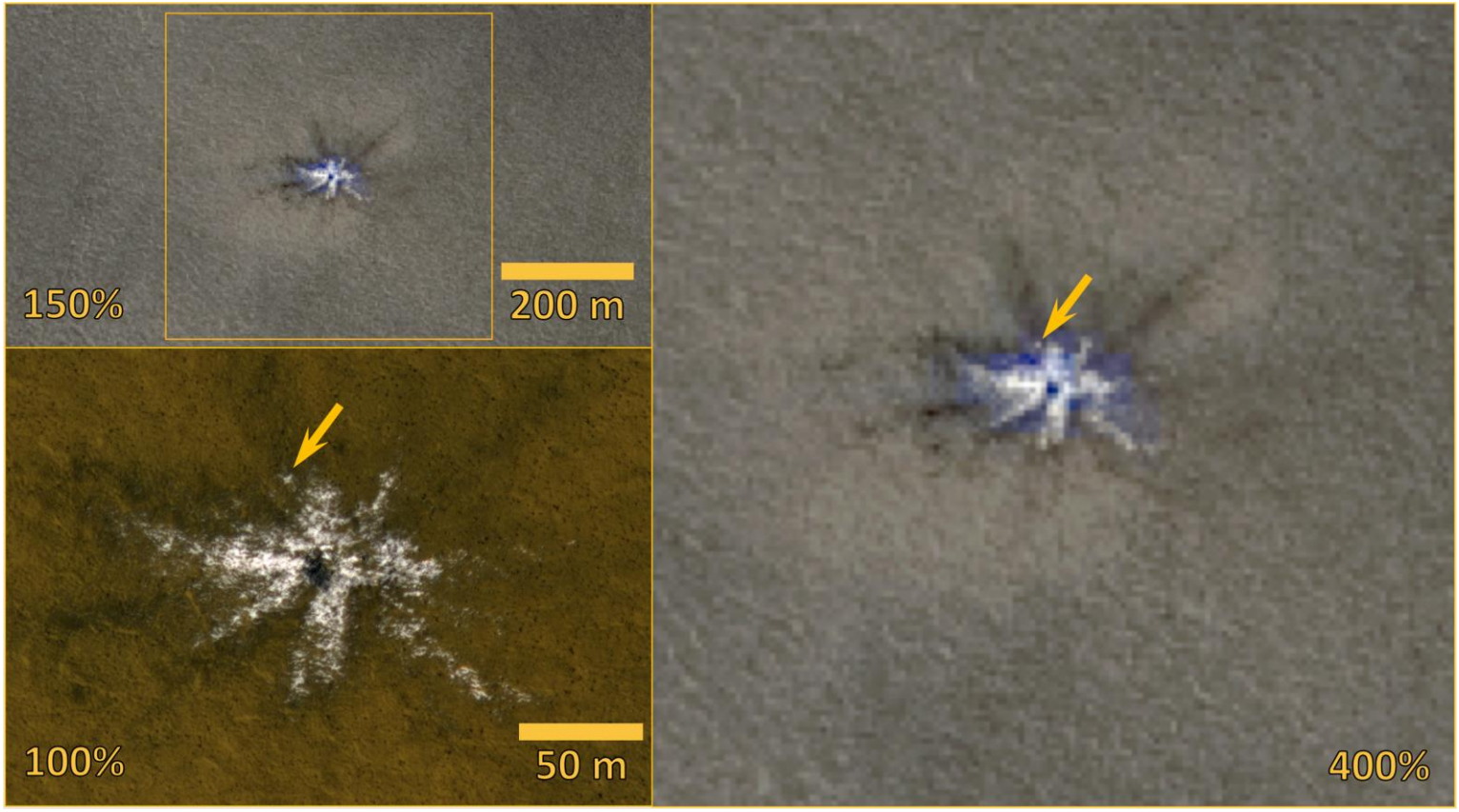

Figure 18 A comparison of a fully-simulated CaSSIS infrared colour image (IRB1) compared to a HiRISE IRB colour image of a recent ice-excavating crater that formed between March 2008 and March 2010 at 44.91°E, 63.92°N. The coordinated HiRISE-CTX-CRISM image used to create the fully-simulated CaSSIS image (**above left** and **right**) was acquired on the 19th of May 2010, at the onset of northern summer (L_s = 92.9°). As can be seen here, the fully-simulated CaSSIS images (**above left** and **right**) compares remarkably well with the HiRISE IRB image ESP_017868_2440 (**lower left**). The dark-toned rayed ejecta, ice-distribution – including a small discrete patch of ejected ice (arrow) are all well-resolved. **Image credits: WesternU-CPSX/ASC-CSA/NASA, NASA/JPL/JHU-APL/MSSS/UofA and ESA/Roscosmos/ExoMars/CaSSIS.**

figure19 and caption

Click here to download figure
Tornabene_et_al_2016_CaSSIS_sim_SSR_FIGURE19_revised.docx

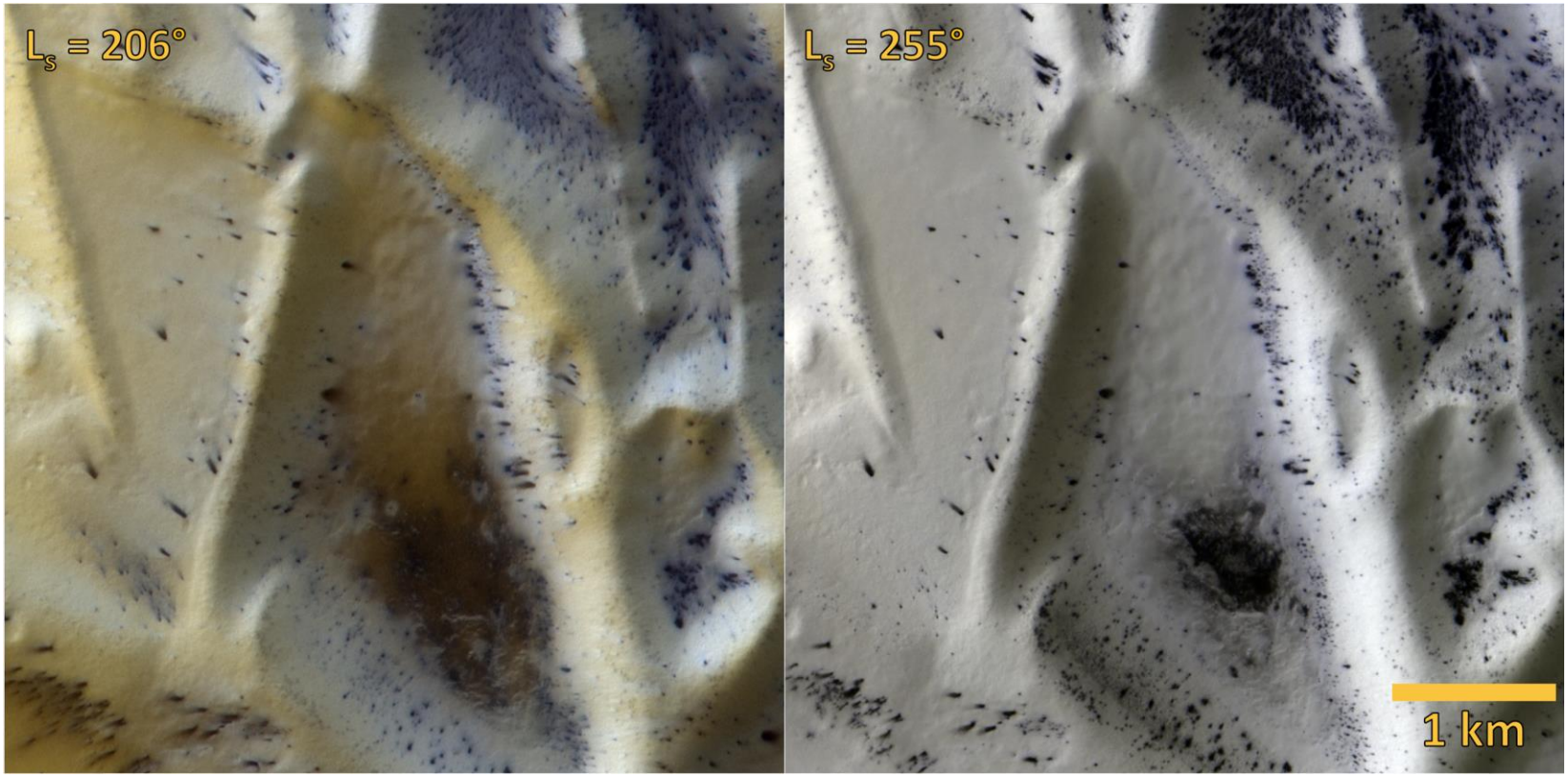

Figure 19 Fully-simulated CaSSIS infrared colour image (IRB1) change-detection pair covering the southern hemisphere site dubbed "Inca City," documenting CO_2 frost sublimation during the transition from southern spring to summer (295.81°E, 81.33°S). From one image to the next, the L_s and incidence angles vary from ~206° to 255° and ~78° to 62°, respectively. Please see the animated GIF provided of this image-set provided with our supporting online supplementary materials. **Image credits: WesternU-CPSX/ASC-CSA/NASA, NASA/JPL/JHU-APL/MSSS/UofA and ESA/Roscosmos/ExoMars/CaSSIS.**

figure20 and caption

Click here to download figure
Tornabene_et_al_2016_CaSSIS_sim_SSR_FIGURE20_revised.docx

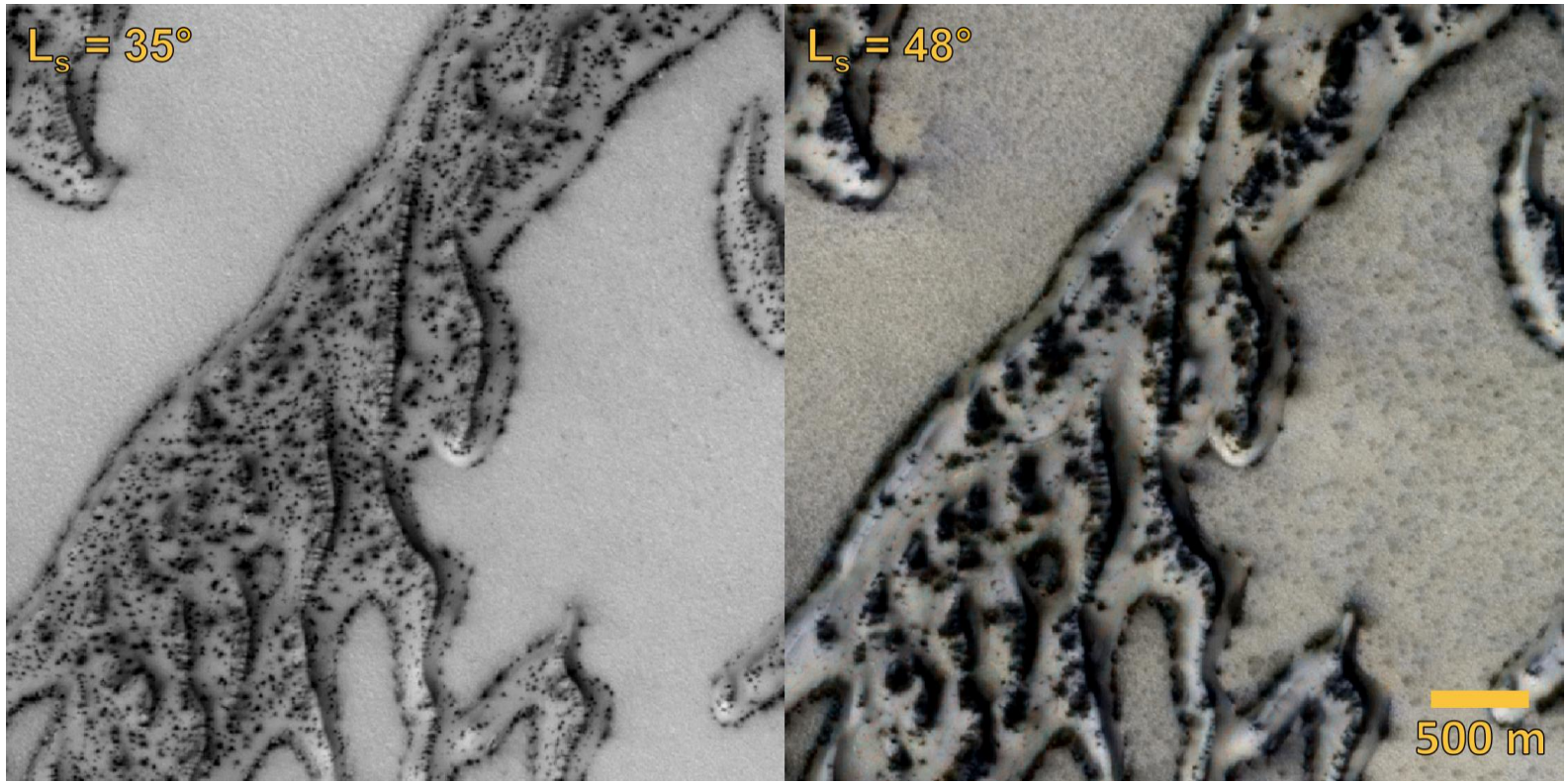

Figure 20 Fully-simulated CaSSIS infrared colour image (IRB1) change-detection pair covering the northern hemisphere site dubbed "Arrakis" dune field documenting CO_2 ice defrosting during the onset of Northern spring (122.58°E, 80.01°N). From one image to the next, the L_s and incidence angles vary from ~35° to 48° and ~61° to 59°, respectively. The simulated CaSSIS image on the right appears less sharp and blurred. This is due to high concentrations of water-ice aerosols, which impacted the clarity of the CRISM-CTX coordinated image set used to construct this simulation product (see Table 2). Despite this atmospheric issue, some of the "smearing" and merging of dark-toned spots observed from one image to the next is consistent with the modification of spots due to wind and aeolian activity (see HiRISE ESP_017100_2600 and ESP_017311_2600). Please see the animated GIF provided of this image-set provided with our supporting online supplementary materials. **Image credits: WesternU-CPSX/ASC-CSA/NASA, NASA/JPL/JHU-APL/MSSS/UofA and ESA/Roscosmos/ExoMars/CaSSIS.**

figure21 and caption

Click here to download figure
Tornabene_et_al_2016_CaSSIS_sim_SSR_FIGURE21_revise

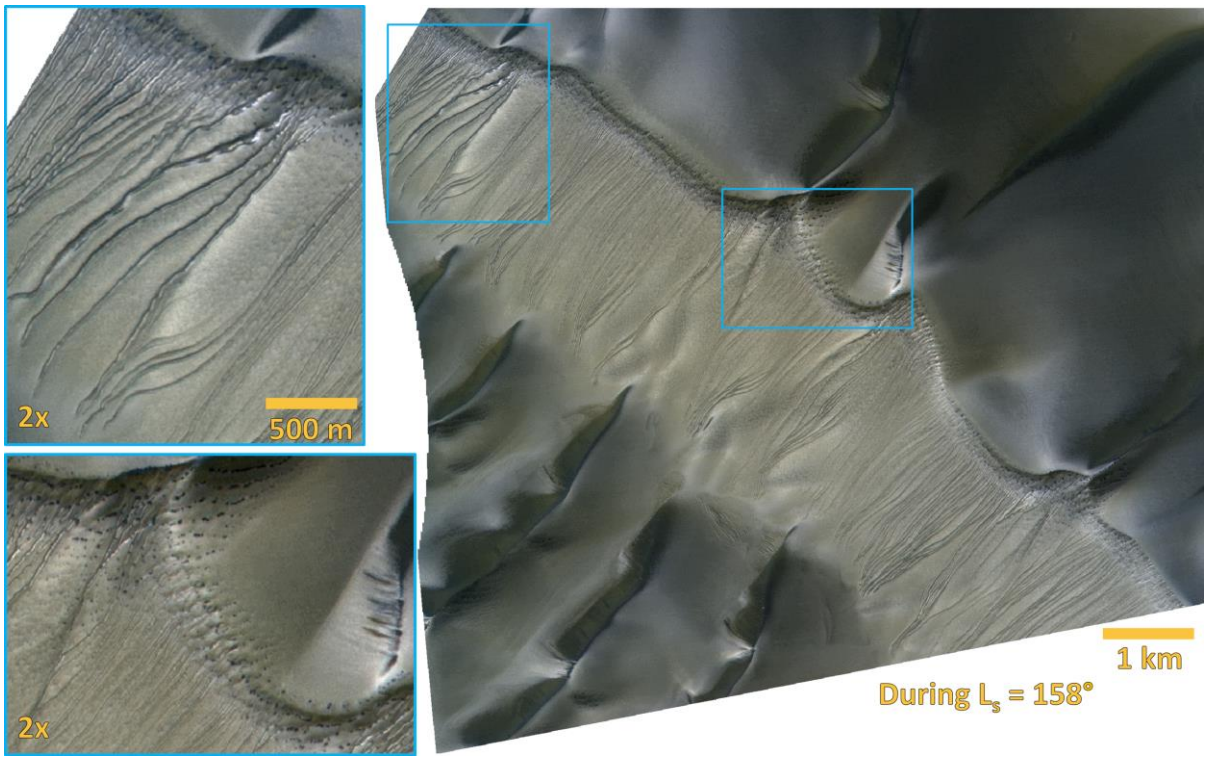

Figure 21 A fully-simulated CaSSIS infrared colour image (IRB1) covering the southern hemisphere site covering the NE portion of the Russell crater dune field (12.94°E, 54.25°S), documenting seasonal activity associated with defrosting and sublimation of CO_2 ice around the onset of southern spring (L_s = 157.7°) and an incidence of ~80°. **Image credits: WesternU-CPSX/ASC-CSA/NASA, NASA/JPL/JHU-APL/MSSS/UofA and ESA/Roscosmos/ExoMars/CaSSIS.**

figure22 and caption

Click here to download figure
Tornabene_et_al_2016_CaSSIS_sim_SSR_FIGURE22_revised.docx

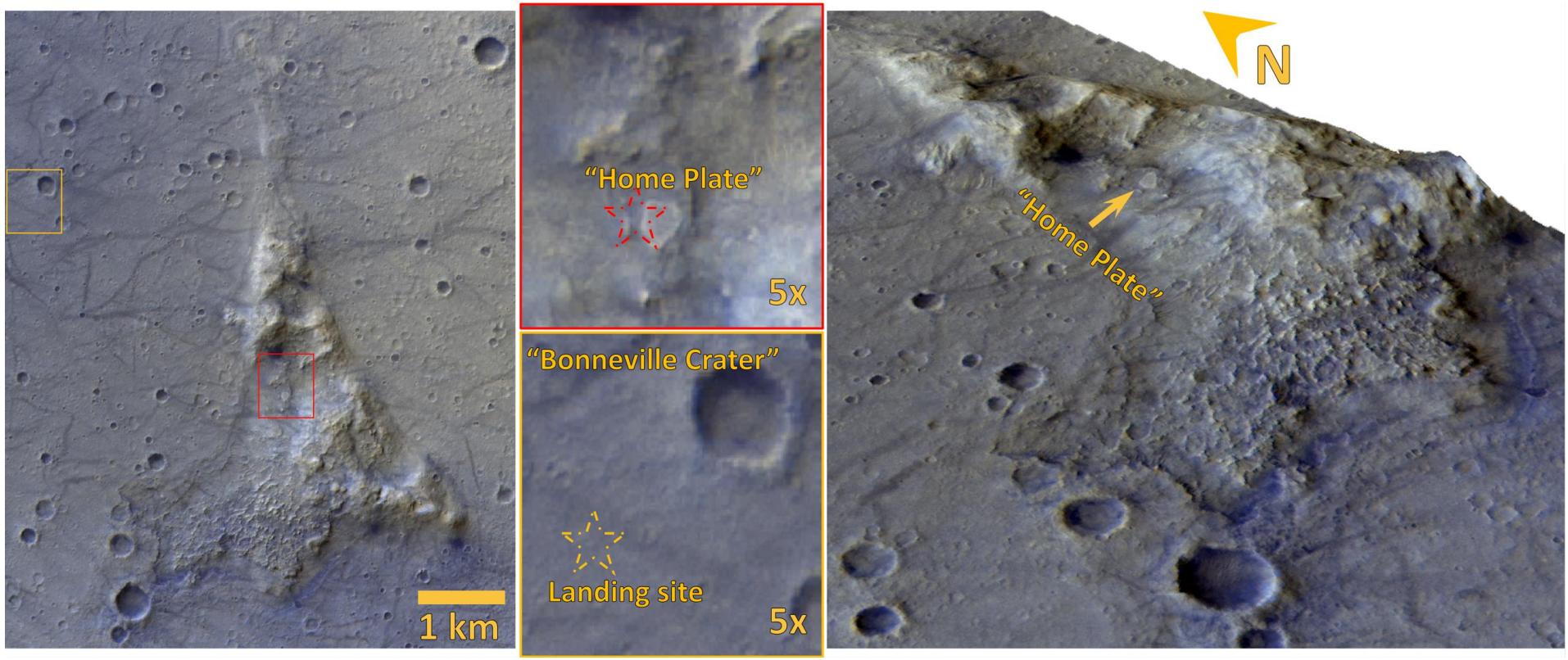

Figure 22 Portions of a fully-simulated CaSSIS infrared colour image (IRB1) and 3D perspective view of the Mars Exploration Rover (MER) Spirit landing site (**orange star**) and the Columbia Hills (175.54°E, 14.62°S) in Gusev crater. The **red star** indicates the last known location of Spirit (see HiRISE ESP_016677_1650). The rover is clearly too small (1.6 x 2.3 meters) to be resolved by CaSSIS. **Image credits: WesternU-CPSX/ASC-CSA/NASA, NASA/JPL/JHU-APL/MSSS/UofA and ESA/Roscosmos/ExoMars/CaSSIS.**

figure23 and caption

Click here to download figure
Tornabene_et_al_2016_CaSSIS_sim_SSR_FIGURE23_revised.docx

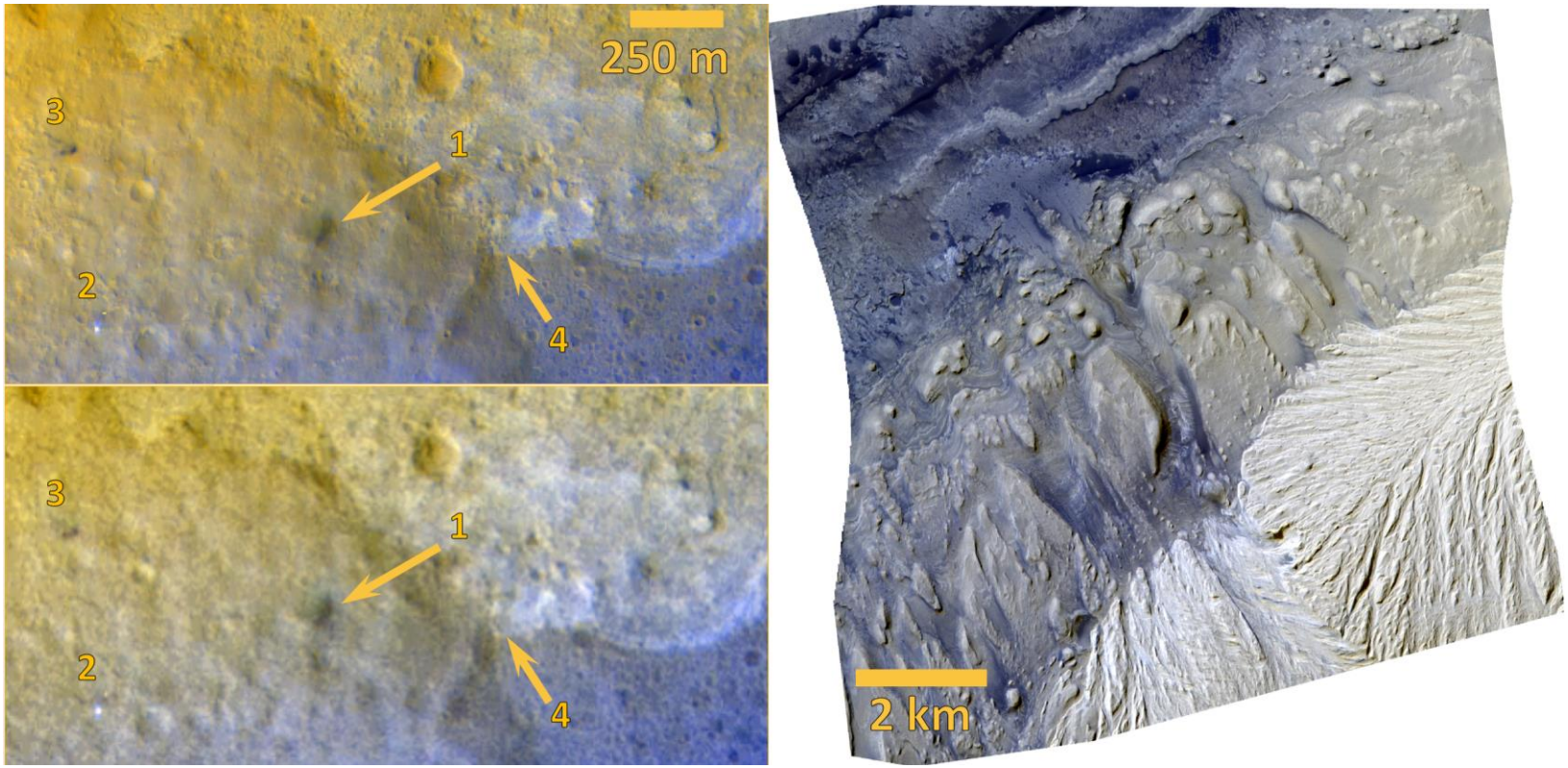

Figure 23 Fully-simulated CaSSIS infrared colour (IRB1) images of the Mars Science Lab (MSL) Curiosity landing site ("Bradbury Landing") and a portion of Aeolis Mons (*a.k.a*, "Mount Sharp"). Here we compare a HiRISE-based simulated CaSSIS image (**above left**) with one that is CTX-based (**below left**) centered at 137.45°E, 4.60°S. In both simulations, landing site features, such as (**1**) "Bradbury Landing" landing site, (**2**) the parachute and backshell, and (**3**) the sky crane impact site, are all resolvable; however, and despite its relatively large size (2.8 x 3.0 meters), nether the Curiosity rover, which was located at the Yellowknife Bay location (**4**) during the acquisition of the CRISM-CTX-HiRISE coordinated images, nor the rover tracks leading there, can be resolved in our simulated images (see HiRISE ESP_030313_1755). The image on the right is a fully-simulated CaSSIS infrared colour image of a portion of "Mount Sharp" (137.42°E, 4.79°S), which is currently being investigated by the MSL-Curiosity rover. **Image credits: WesternU-CPSX/ASC-CSA/NASA, NASA/JPL/JHU-APL/MSSS/UofA and ESA/Roscosmos/ExoMars/CaSSIS.**

figure24 and caption

Click here to download figure
Tornabene_et_al_2016_CaSSIS_sim_SSR_FIGURE24_revised.docx

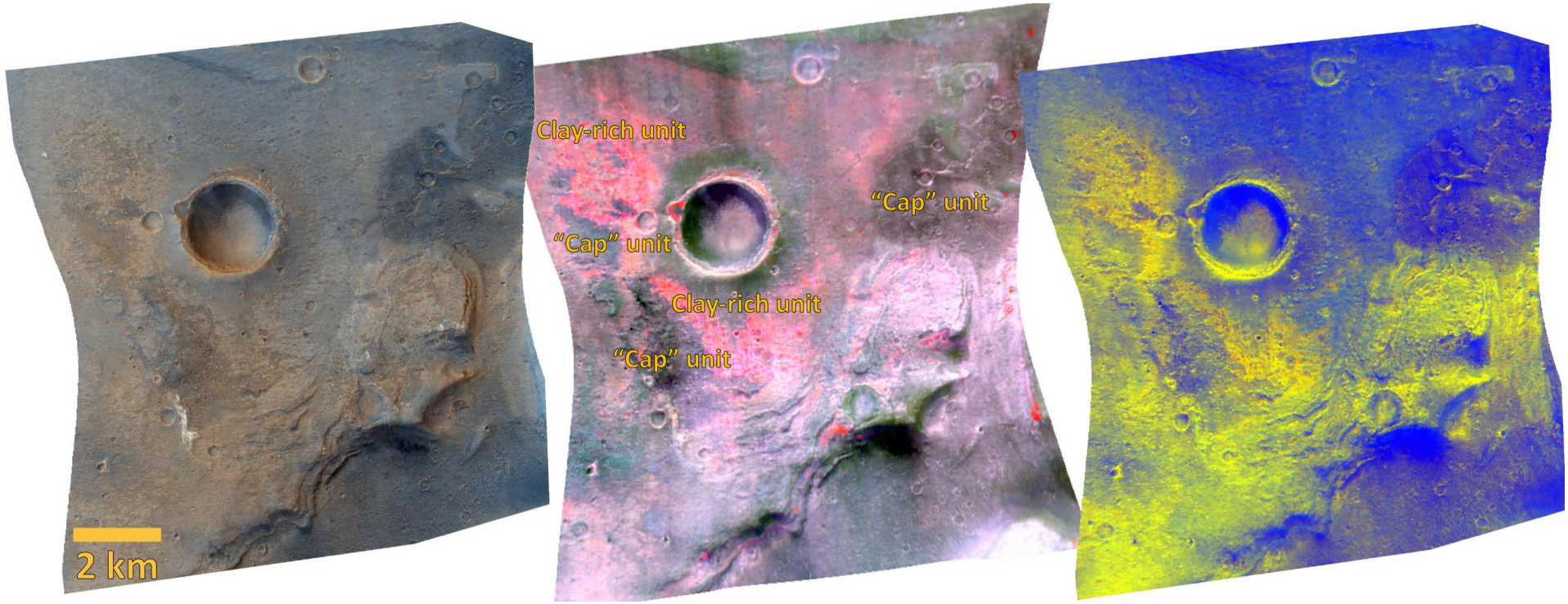

Figure 24 A comparison of fully-simulated CaSSIS colour images with a CRISM spectral parameter image composite covering the southeastern portion of the ExoMars 2020 landing ellipse in Oxia Planum (336.1°E, 17.7°N). A fully-simulated CaSSIS synthetic "true" colour image (RGB) (**left**) and the CBRC1 image (**right**) highlight the differences between ferrous- (blue and purple) and ferric-bearing (orange and yellow) materials compared to a CRISM spectral parameter composite image (**centre**), which was constructed in a similar fashion to the one in Figure 14. The most intensely altered areas (strong magenta colour) shown by the CRISM composite is most distinctive in the simulated CaSSIS CBRC1 image (**right**) as an orange-coloured unit. **Image credits: ASC-CSA/WesternU-CPSX, ESA/Roscosmos/ExoMars/CaSSIS and NASA/JPL/JHU-APL/MSSS/UofA.**

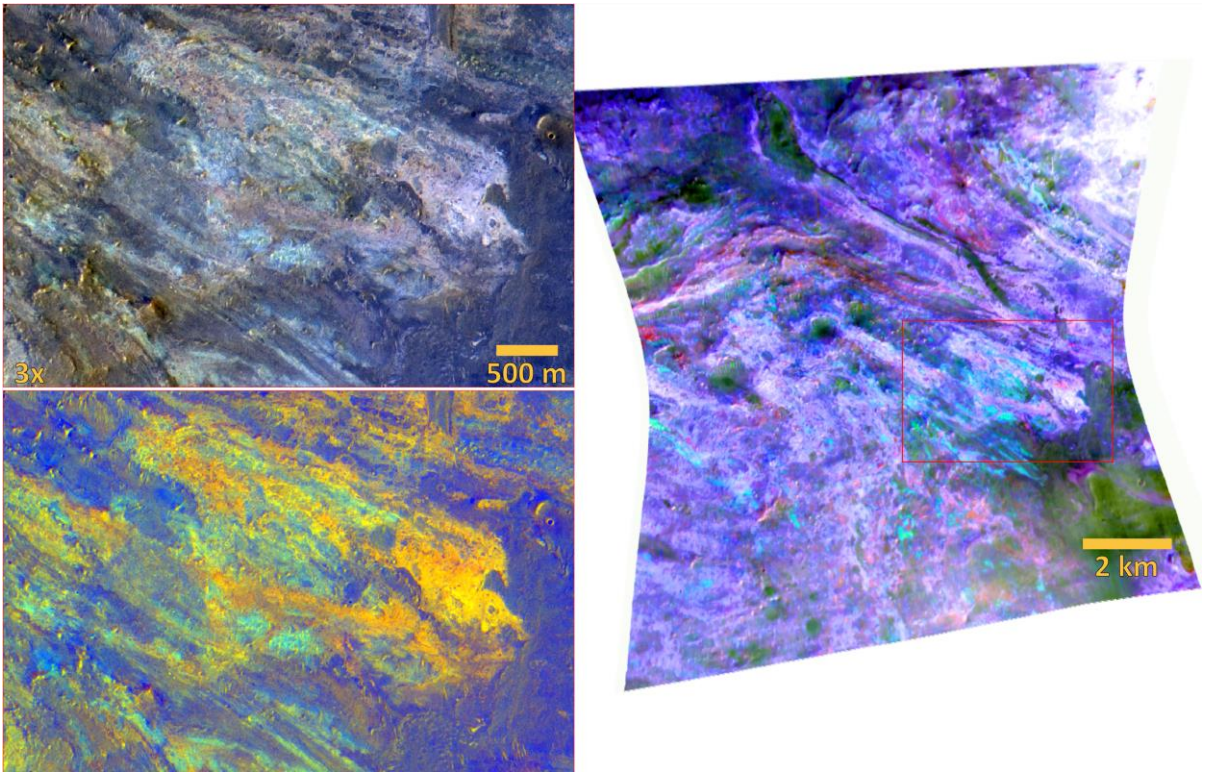

Figure 25 A comparison of a close-up fully-simulated CaSSIS colour images with a CRISM spectral parameter composite image covering a portion of the former Mars 2020 candidate landing site "Nili Fossae Trough" (74.58°E, 21.05°N). The close-up infrared colour (IRB1) (**upper left**) and CBRC1 (**lower left**) images demonstrate the level of colour and morphologic detail of various landing sites provided by the anticipated CaSSIS dataset. The simulated images, and a context CRISM spectral parameter composite (constructed in a similar fashion to the one in Figure 14) provide details on the clast and matrix compositional diversity of the scoured and well-exposed Hargraves ejecta blanket, which occupies the majority of the proposed landing ellipse (> 50%). The sharp contacts between ferrous (Fe^{2+}) (**blues**) and ferric (Fe^{3+}) iron-bearing deposits (**yellows** and **oranges**) observed in the fully-simulated CaSSIS images (**left**) provide locations and potential sampling sites where redox chemical gradients occurr, and where past life may have possibly flourished. **Image credits: ASC-CSA/WesternU-CPSX, ESA/Roscosmos/ExoMars/CaSSIS and NASA/JPL/JHU-APL/MSSS/UofA.**

Table 1 CaSSIS Bands

Band# / Name	Band Centre	Bandwidth	[1]Colour
[2]0 / Synthetic "Blue"	*"475.0" nm*	*N/A*	***Blue***
1 / BLU	499.9 nm	118.0 nm	**Blue-Green**
2 / PAN	675.0 nm	229.4 nm	**Orange-Red**
3 / RED	836.2 nm	94.3 nm	**NIR**
4 / NIR	936.7 nm	113.7 nm	**NIR**

[1]Based on band centre wavelength

[2]The synthetic "blue" band, which we denote as band 0, is calculated similarly to the HiRISE "synthetic blue" band using the blue-green and red wavelengths, *i.e.*, BLU and PAN, respectively (see Delamere et al 2010)

Table 2 Datasets used to construct fully-simulated CaSSIS cubes

Feature or Location	CRISM (18-20m/pix)	CTX (5-6m/pix)	HiRISE (25-50cm/pix)	[1]Observation Date	[2]Atmosphere (τ_{dust} / τ_{ice})	[1]Observation Angles (°) Incid.	[2]Emiss.	Phase	L_s
Russell Crater dunes (Fig. 21)	FRT000039DF	P02_001981_1255_	PSP_001981_1255	2006-12	0.5-1.0 / 0-0.2	80.66	8.79	73.8	157.7
Nili Fossae (Fe Olivine and Fe-Mg Carbonate) (Figs. 3, 7, 8, 10, S2-S4)	FRT00003E12	P03_002176_2024_	PSP_002176_2025	2007-01	0.0-0.5 / 0-0.2	53.94	6.07	60.01	165.8
"Inca City" ([3]Change detection pair) (Fig. 19)	FRT00004F9B FRT0000629D	P05_003092_0983_ P08_004147_0985_	PSP_003092_0985 PSP_004081_0985	2007-03 2007-06	0.5-1.0 / 0-0.2 1.0-1.5 / 0-0.2	76.48 62.25	1.65 0.66	77.89 62.77	206.65 254.81
Jezero Crater & Mars 2020 (Fig. S5 & S10)	FRT00005C5E	P03_002387_1987_	PSP_002387_1985	2007-05	0.5-1.0 / 0-0.2	63.94	17.57	49.32	240.84
Eberswalde Delta & Mars 2020 (Fig. S11)	FRT000060DD	P01_001336_1560_	PSP_001336_1560	2007-06	0.5-1.0 / 0-0.2	44.52	1.85	42.67	250.81
Alga Crater uplift (Fig. 12)	FRT00006415	P08_004158_1556_	PSP_007573_1555	2007-06	1.0-1.5 / 0-0.2	42.79	6.35	36.45	258.62
Nili Fossae Trough (LCP) & Mars 2020 (Figs. 9d & S13)	FRT000064D9	P07_003587_2005_	PSP_003587_2015	2007-06	0.5-1.0 / 0-0.2	62.64	3.26	65.18	261.69
Ritchey Crater uplift (Fig. 13)	FRT00007C34	P11_005372_1514_	PSP_005372_1515	2007-09	1.0-1.5 / 0-0.2	33.6	7.93	41.16	316.31
Oxia Planum (Capping unit) & ExoMars 2020 (Fig. 24)	FRT0000810D	P22_009735_1977_	PSP_009735_1985	2007-10	0.5-1.0 / 0-0.2	45.21	1.34	46.22	326.13
Elorza Crater uplift (Fig. 12)	FRT00008236	P12_005649_1696_	PSP_005649_1710	2007-10	1.0-1.5 / 0-0.2	33.37	1.75	31.62	328.46
Horowitz uplift RSL (Fig. 16)	FRT00008573	P12_005576_1473_	PSP_005787_1475	2007-10	0.5-1.0 / 0-0.2	39.31	8.2	32.7	334.35
Martin Crater uplift (Fig. 12)	FRT00008649	P12_005821_1585_	PSP_005821_1585	2007-10	0.5-1.0 / 0-0.2	35.08	2.12	33.09	335.78

Mawrth Vallis (Craters) ExoMars & Mars 2020 (Fig. S12)	FRT000094F6	P15_006821_2045_	PSP_006821_2045	2008-01	0.0-0.5 / 0-0.2	39.42	7.34	46.58	15.26
Oxia Planum ("Delta") & ExoMars 2020 (Fig. S9)	FRT00009A16	P15_007019_1978_	PSP_007019_1980	2008-01	0.5-1.0 / 0-0.2	38.71	0.49	39.17	22.54
Nili Fossae (Talc) (Figs. 9s & 14)	FRT00009D44	P16_007200_2002_	PSP_007200_2005	2008-02	0.0-0.5 / 0-0.2	39.18	1.44	40.62	29.08
Mawrth Vallis ExoMars & Mars 2020 (Fig. S12)	FRT0000A600	P17_007612_2043_	PSP_007612_2045	2008-03	0.0-0.5 / 0-0.2	38.84	20.85	59.63	43.62
Nili Fossae (Kaolinite & Serpentine) (Fig. 9m & see Fig. 28 in Thomas et al this issue)	FRT0000ABCB	P19_008347_2019_	No HiRISE coverage	2008-05	0.0-0.5 / > 0.2	43.44	0.15	43.32	68.83
Nili Fossae Trough & Mars 2020 (Fig. 25)	FRT0000B012	P20_008782_1999_	PSP_008782_2015	2008-06	0.0-0.5 / 0-0.2	45.17	5.79	39.8	83.65
Toro Crater Uplift	FRT0000B1B5	P12_005842_1964_	PSP_005842_1970	2008-06	0.0-0.5 / > 0.2	45.91	4.96	50.39	85.91
Aeolis Mons ("Mount Sharp") & MSL-Curiosity (Fig. 23)	FRT0000B6F1	P21_009149_1752_	PSP_009149_1750	2008-07	0.5-1.0 / 0-0.2	58.86	14.34	48.46	96.28
Chlorides (Fig. 11)	FRT00010A4E	B05_011691_1409_	PSP_003160_1410	2009-01	0.5-1.0 / 0-0.2	62.5	4.93	57.96	196.58
Negril crater uplift	FRT000110B7	B06_011960_2004_	ESP_025766_2005	2009-02	0.5-1.0 / 0-0.2	64.11	6.38	58.03	209.14
Unnamed crater uplift (Fig. 12)	FRT00012B01	B09_013134_1611_	ESP_013134_1610	2009-05	0.5-1.0 / 0-0.2	43.08	7.1	36.19	266.54
Verlaine Crater uplift (Fig. 12)	FRT00012CD9	B09_013213_1707_	ESP_013213_1705	2009-05	0.5-1.0 / 0-0.2	44.82	1.53	43.34	270.42
Gasa Crater gullies (^{3}Change detection pair) (Fig. 17)	FRT00013F9F FRT0001E5A2	B11_014081_1440_ G12_022718_1439_	ESP_014081_1440 ESP_022718_1440	2009-07 2011-06	0.0-0.5 / 0-0.2 0.5-1.0 / 0-0.2	36.65 34.76	0.82 2.75	37.35 32.29	311.52 303.31

Columbia Hills, MER-Spirit & Mars 2020 (Figs. 22 & S8)	FRT000168F3	B18_016677_1653_	ESP_016677_1650	2010-2	0.0-0.5 / 0-0.2	57.04	7.36	51.85	52.23
"Arrakis" dune field ([3]Change detection pair) (Fig. 20)	FRT00016B45 FRT000175A2	B18_016744_2601_ B19_017100_2601_	ESP_016744_2600 ESP_017100_2600	2010-2 2010-3	0.0-0.5 / > 0.2 Not Available	61.28 58.67	0.87 2.07	61.93 60.34	54.54 66.69
Recent ice-excavating impact (Fig. 18)	FRT00018E24	B21_017868_2451_	ESP_017868_2440	2010-05	Not Available	47.73	6.98	54.13	92.92
Unnamed crater uplift (Fig. 12)	FRT0002367C	D17_033757_1513_	ESP_028509_1510	2012-03	Not Available	71.1	2.42	69.63	78.18
Bradbury Landing Curiosity-MSL (Fig. 23)	FRS00028346	D08_030313_1751_	ESP_030313_1755	2013-01	Not Available	50.34	4.45	46.14	244.14

[1]Based off CRISM observation; [2]See Wolff et al (2009) and Fernando et al (2017); [3]Value based on the central nadir-looking scan of a CRISM targeted observation); [4]See animated GIFs included as part of our online supplemental materials; *Red text denotes non-coordinated, atmospheric dust and/or ice aerosol contamination, and high emission (> 9°) observations

Table 3 CaSSIS Band Ratios or Spectral Parameters for Distinguishing Common Surface Materials and Atmospheric Phenomena

Product	[1]Sensitivity	Description	Min./phase examples	[2]Alternates
2PAN/1BLU (Figs. 7 & S6)	Ferric iron(Fe^{3+})	Absorption short of ~550 nm due to intervalence charge transfer of Fe^{3+}	Hematite, goethite, akaganeite, nontronite	3/1, 4/1
2PAN/4NIR (Figs. 7 & S6)	Ferrous iron (Fe^{2+})	Broad absorption centered around ~1000-1100 nm due to crystal field transitions from the presence of Fe^{2+}	Low-Ca pyroxenes, olivines, high-Ca proxenes	3/4, 2/3
3RED/2PAN (Fig. 7)	Ferric iron (Fe^{3+})	Small broad absorption (*e.g.*, ~860 nm absorption for hematite) and slope around ~600-700 nm due to crystal field transitions from the presence of Fe^{3+}	Nontronite, Hematite	None
Mean[1BLU-4NIR]/(4NIR/1BLU) (Figs. 6 & S6)	Ices, Frosts, some atmospheric phenomena	Ices and some atmospheric phenomena (*e.g.*, haze, fog, clouds, dust devils, avalanche clouds, etc.), compared to other surface materials, would have the highest reflectance values in all 4 CaSSIS bands (*e.g.*, very high mean reflectance) and are most distinctive on Mars with respect to blue wavelengths, a NIR- or red-to-blue ratio and albedo (see text for more details)	H_2O, CO_2, Fog, Haze, Clouds	Mean[1-3]/(3/1), Mean[1,2]/(2/1), or Band 1 (blue-green) image
Colour Band Ratio Composites				
CBRC1 (Figs. 7, 9, 11, 14, 24, 25, S9-S13)	Distinguishes Ferric, and Fe-poor deposits	3/2, 2/1, 2/4 in R-G-B (see above for description of individual ratios)	N/A	(see above for possible alternate combinations)
CBRC2 (Fig. S6)	Distinguishes Ice/atmospheric phenomena from other surface materials	3/2, 2/1, Mean[1-4]/(4/1) in R-G-B (see above for description of individual ratios)	N/A	(see above for possible alternates combinations)

[1]Higher values provided by these band ratios or spectral parameters signifies the likelihood of the presence of the materials listed under this heading as a surface component
[2]Band numbers are as follows: 1 – BLU (499.9 nm), 2 – PAN (675.0 nm), 3 – RED (836.2 nm) and NIR (936.7 nm)